NASA CR-66002
[NAA] SID 65-411-1A

A STUDY TO DEFINE A STATE-OF-THE-ART ROCKET VEHICLE SUITABLE FOR SYNOPTIC METEOROLOGICAL SOUNDINGS

VOLUME I

By D. L. Howley

April 8, 1965 Revised June 16, 1965

Prepared under Contract No. NAS 1-4427 by
NORTH AMERICAN AVIATION, INC.
SPACE AND INFORMATION SYSTEMS DIVISION
Downey, Calif.

for Langley Research Center

NATIONAL AERONAUTICS AND SPACE ADMINISTRATION

For sale by the Clearinghouse for Federal Scientific and Technical Information
Springfield, Virginia 22151 – Price $4.00

FOREWORD

This volume, the first of two comprising the final report on a study to define a state-of-the-art rocket vehicle suitable for synoptic meteorological soundings, discusses the evaluation of candidate vehicle system approaches with respect to the design objectives established for the study and the selection of the most feasible system approach. A preliminary design and an analysis of the selected concept are also presented.

Volume II discusses growth potential aspects of the vehicle performance. Volume II is classified CONFIDENTIAL, because it presents data on advanced state-of-the-art propellants.

This report has been prepared by the Space and Information Systems Division of North American Aviation, Inc., for the National Aeronautics and Space Administration under Contract No. NAS1-4427. This contract was administered by the Langley Research Center under the technical direction of Hal T. Baber, Jr., of the Vehicle Performance Branch, Applied Materials and Physics Division, Langley Research Center.

CONTENTS

	Page
INTRODUCTION	1
SYSTEM REQUIREMENTS	5
Sensors	5
Ground Station Model	7
Payload Model	9
Major Design Objectives	11
SYSTEM EVALUATION STUDIES	15
System Performance Comparisons	15
System Reliability Comparisons	64
Comparative Production Cost Evaluation	73
System Selection	78
SYSTEM DESIGN	81
Vehicle Description	81
Rocket Motor Characteristics	89
Aerodynamic Characteristics	90
Stability and Control Characteristics	101
Magnus Instability	111
Trajectory Characteristics	113
Launcher Subsystem Design	122
CONCLUSIONS AND RECOMMENDATIONS	129
REFERENCES	131

ILLUSTRATIONS

Figure		Page
1	Representative Payload - Apogee Spectrum	2
2	Ground Station Complex	8
3	Design Wind Profiles	13
4	99 Percent Surface Wind Envelopes—Wallops Island	13
5	Parametric Motor Variations	18
6	Initial Attitude Response	20
7	Apogee Versus Vehicle Stability—99 Percent Headwind	21
8	Representative Wind Sensitivity	22
9	Energy Relationship	24
10	Representative Thrust-to-Weight and Burn-Time Characteristics	25
11	Initial Trajectory Characteristics—High Thrust-to-Weight Ratio	26
12	Single-Stage Altitude-Velocity Profiles	28
13	Initial Single-Stage Aerodynamic Characteristics	30
14	Nominal Reynolds Number History	31
15	Initial Single-Stage Performance Trades	32
16	T/W = 7 Parametric Variations	34
17	Single-Stage/Apogee Separation Trajectory Characteristics—No Wind	35
18	Single-Stage/Apogee Separation Trajectory Characteristics—99 Percent Headwind	36
19	Single-Stage/Apogee Separation Trajectory Characteristics—99 Percent Headwind	37
20	Lift-off Conditions—Single Stage	38
21	Lower-Altitude Conditions—Single Stage	38
22	Wind Effect on Apogee—Single-Stage Apogee Separation	39
23	Range at Apogee—Single-Stage Apogee Separation	39
24	Single Propulsive Stage-Stabilized Payload Separated at Burn-out	41
25	Single Propulsive Stage-Stabilized Payload Separated at Burn-out Trajectory Characteristics	42
26	Single Propulsive Stage-Stabilized Payload Separated at Burn-out Trajectory Characteristics	43
27	Wind Effect on Apogee—Single Propulsive Stage-Stabilized Payload Separated at Burn-out	44
28	Range at Apogee—Single Propulsive Stage-Stabilized Payload Separated at Burn-out	44

Figure		Page
29	Dual-Thrust Performance Trades	46
30	Dual-Thrust Altitude-Velocity Profile	48
31	Dual-Thrust Trajectory Characteristics	49
32	Dual-Thrust Trajectory Characteristics	50
33	Wind Effect on Apogee—Dual-Thrust Systems	51
34	Range at Apogee—Dual-Thrust System	51
35	Two-Stage Configuration	52
36	Variation in Apogee Conditions With Coast Time	53
37	Two-Stage Altitude-Velocity Profiles	54
38	Wind Effect on Apogee—Two-Stage System	56
39	Range at Apogee—Two-Stage System	56
40	Trajectory Characteristics—Two-Stage System	57
41	Trajectory Characteristics—Two-Stage System	57
42	Wind Effect on Apogee—Final Two-Stage System	58
43	Range at Apogee—Final Two-Stage System	58
44	Generalized Sequence of Events	65
45	Representative Motor Reliability Test Data	71
46	Sample Size Requirements	74
47	Cost, Apogee, Payload Comparison	76
48	Inboard Profile	83
49	Parachute Deployment Concepts	85
50	Motor Characteristics	92
51	Average Motor Thrust Variation With Temperature	93
52	Fineness Ratio Selection	93
53	Estimated Drag Characteristics	94
54	Boattail Equivalent Body	95
55	Estimated Aerodynamic Derivatives	97
56	Estimated Aerodynamic Derivatives	98
57	Estimated Aerodynamic Derivatives	99
58	Vehicle Surface Temperatures	99
59	Transient Heating Functions at One Diameter Back From Nose	100
60	Nutational Frequency of the Nonspinning Vehicle	103
61	Root Locus	103
62	Steady-State Amplitude Ratio During Resonance	104
63	Amplitude Ratio for Resonance at Three Different Times	104
64	Amplitude Ratio and Phase Angle	105
65	Pitch Response Through Resonance	107
66	Total Incidence Angle Through Resonance for One Degree Steady-State Trim	108
67	Spin-Forcing Methods	109
68	Helix Angle of Ring-Spin With Motor Vanes	110
69	Spin Contribution to Nutational Precessional Frequencies at High Altitudes	112

Figure		Page
70	Critical Magnus Moment Coefficient	112
71	Nominal Performance Trajectory—No Wind, English Units	114
72	Nominal Performance Trajectory—99 Percent Headwind, English Units	115
73	Nominal Performance Trajectory—No Wind, Metric Units	116
74	Nominal Performance Trajectory—99 Percent Headwind, Metric Units	117
75	Effect of Launch Velocity—50 Percent Profile Wind	118
76	Effect of Launch Velocity—99 Percent Profile Wind	118
77	Altitude at 124 Seconds	120
78	Nominal Spin Rate History	120
79	Apogee and Range Dispersion—50 Percent Wind Profile	121
80	Apogee and Range Dispersion—99 Percent Wind Profile	121
81	Ground Impact Dispersion—50 Percent Wind Profile	123
82	Ground Impact Dispersion—99 Percent Wind Profile	123
83	Launcher Configuration	125

TABLES

Table		Page
1	Sensor State of the Art	7
2	Representative Current Propellant Characteristics	17
3	Initial Single-Stage Motor Characteristics	27
4	Revised Single-Stage Motor Characteristics	33
5	Estimated Weight Breakdown—Single Propulsive Stage-Stabilized Payload Separated at Burn-out	45
6	Estimated Weight Breakdown—Continuous-Burn, Dual-Thrust System	47
7	Estimated Weight Breakdown—Final Two-Stage System	55
8	Apogee With Direct Lateral Winds	59
9	Apogee Variance With Increased Drag	62
10	Performance Recapitulation	63
11	Potential Reliability Problem Areas	67
12	Reliability Comparison—Ascent to Altitude Functions	69
13	Reliability Comparison—Payload Functions	70
14	Representative Motor Failure Mode Data	72
15	Estimated Average Unit Cost Comparison	75
16	Candidate System Comparisons on a Cost Per Measurement Base	78
17	Candidate System Comparisons	80
18	Estimated Component Weights and Inertias	90
19	Propulsion System Characteristics	91

SYMBOLS

A	Area
$\|A\|$	Amplification factor
C*	Characteristic exhaust velocity
d	Diameter
E/W	Energy-to-weight ratio
g	Acceleration of gravity
I_{sp}	Specific impulse
I_T	Total impulse
p	Roll rate
q	Pitch rate
$\overline{q}$	Dynamic pressure
r	Yaw rate
T/W	Thrust-to-weight ratio
V	Velocity
W	Weight
θ	Vehicle pitch attitude Euler angle
ϕ	Vehicle roll attitude Euler angle
ψ	Vehicle yaw attitude Euler angle
α	Vehicle angle of attack
β	Vehicle angle of sideslip

γ	Flight path angle
ν	Mass fraction
ω_n	Natural frequency
ζ	Damping ratio
σ	Real part of complex root
$j\omega$	Imaginary part of complex root

General Subscripts

o or i	Initial condition
G	Gross
p	Propellant
t	Time
T	Total

Aerodynamic Derivatives

C_{N_α}	Normal force coefficient per unit angle of attack
C_{m_α}	Pitching moment coefficient per unit angle of attack
C_{l_p}	Damping in roll derivative
C_{m_q}, $C_{m_{\dot{\theta}}}$	Damping in pitch derivative
C_{n_r}, $C_{n_{\dot{\psi}}}$	Damping in yaw derivative

INTRODUCTION

The sounding rocket has made it possible to attain many high-altitude, direct geophysical observations that are vital in understanding and resolving both terrestrial and space-oriented problems. The rockets are used in geophysics and astronomy research, meteorological observations, and in supporting roles to various National Aeronautics and Space Administration and military programs, and they make possible fulfillment of the data gap between the lower-altitude region (20-30 kilometers) covered by balloon soundings and the upper regions (170-180 kilometers) being assessed by satellites.

In general, the sounding rocket spectrum may be broken into two major categories—large and small. The large vehicles are used primarily in space sciences support—upper atmosphere research, component testing, etc. —while the smaller rockets are used principally in synoptic meteorological research and operations. A representative spectrum of the altitude and payload capabilities displayed by current vehicles is shown in Figure 1.

The establishment in 1959 of the Meteorological Rocket Network to provide simultaneous observations in the upper atmosphere continued to underline the requirement for a system that is simple, reliable, inexpensive, and capable of being fired on a round-the-world basis. In September 1964, NASA's Langley Research Center awarded to the Space and Information Systems Division of North American Aviation, Inc., a six-month study contract to define a state-of-the-art rocket vehicle suitable for synoptic meteorological soundings. This document, Volume I of two volumes, presents the final report on system evaluation studies associated with the selection of the most feasible vehicle approach and a preliminary design of the selected concept. Volume II discusses the growth potential aspects of the vehicle performance.

The objectives of the study included attainment of a system that displayed operational capability under relatively severe surface wind environments, had a high probability of attaining the design altitude under this wind environment within given launch angle restrictions, and satisfied state-of-the-art requirements with regard to vehicle, motor, and payload instrumentation technology. In addition, the selection of the most feasible system included consideration of the relative production costs and growth potential associated with the following candidate concepts:

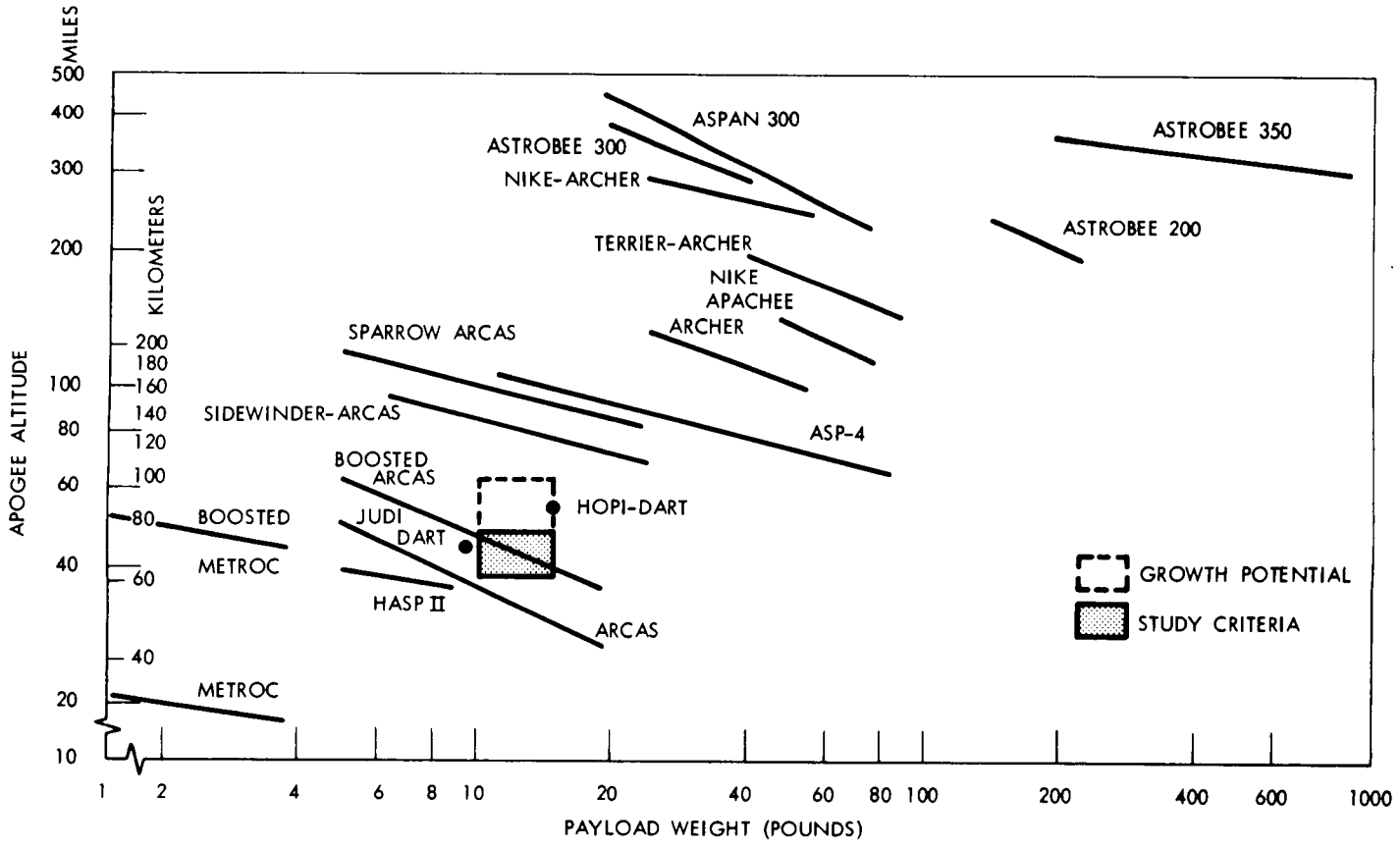

Figure 1. Representative Payload—Apogee Spectrum

1. A single-stage system with payload remaining attached until apogee (or near apogee) was reached

2. A single-thrusting-stage system with a stabilized, nonpropulsive payload separating prior to apogee

3. A single-stage system with a continuous-burn, dual-thrust-level motor

4. A two-propulsive-stage system.

The latter two approaches also included payload separation at, or near, apogee conditions.

Under the ground rules established for the study, and discussed in the System Requirements section, and on the basis of comparative evaluations that included the aforementioned aspects of performance, reliability, production costs, and other factors, the single-stage system with payload separated at apogee was judged the most feasible approach and was selected for preliminary design. The dual-thrust system was recognized as an extremely close contender; however, in view of the lesser amount of developmental and operational history associated with the system, the more conventional motor approach was recommended.

SYSTEM REQUIREMENTS

The meteorological sounding rocket, to effectively support synoptic and research firings, must be capable of operational use on a world-wide basis and under relatively severe environmental conditions. It must provide this capability with a high degree of cost-effectiveness and minimal ground support equipment. It is, in essence, the workhorse of the meteorological data-gathering business and, as such, it must be able to support specifically scheduled firings under varying seasonal conditions and on a round-the-clock basis.

Before reviewing the specific design objectives associated with this study, it appears worthwhile to examine the overall job of the meteorological sounding rocket and some of the data-acquisition methods employed.

SENSORS

There are five basic atmospheric parameters which (in the altitude region of interest in this study) appear to be measurable with current state-of-the-art sensors and which define most of the atmospheric characteristics of prime importance to synoptic meteorological needs:

1. Wind
2. Temperature
3. Pressure
4. Density
5. Ozone content

There are other important measurements—e.g., radiation level, moisture content, turbulence—but, since measurement techniques are relevant to this study only insofar as they help to define desired payload characteristics, the initial list appears sufficiently broad in scope to use as a base point.

The various methods of measuring wind can be classified into four basic categories: (1) passive tracking of a target, (2) analysis of trajectory

characteristics of a rocket, (3) measuring wind influences on the speed of sound, and (4) active techniques with a transponder. The passive tracking technique involves deployment of rocketborne reflective targets such as chaff, spheres, or parachutes for subsequent tracking by ground radar. One method of measuring wind from the flight characteristics of a rocket uses a combination of ground-determined velocity, rocket attitude as sensed by gyros, and the measured angle of attack of the vehicle. The acoustic technique involves the ejection and firing of explosive grenades at known points along the trajectory and subsequent resolution of the wind effects observed on the generated acoustic waves. The active techniques utilize a transponder descending on a parachute or inflated sphere to provide a signal to a combination ground-based tracking and receiving system.

Temperature may be measured directly by using a sensor such as the 10-mil bead thermistor, coated to reduce radiation effects. It may also be measured with thin film or acoustic transducer techniques or may be derived from other measurements such as pressure and/or density along with altitude.

Pressure is generally attained from hypsometer or ionization and thermal conductivity gauge measurements. (The hypsometer requires the addition of heat during descent.)

Density may be measured directly with the dynamic pressure gauge technique or by measurement of the drag on a falling sphere. It may also be derived from temperature, pressure, and altitude data.

Electro-chemical detectors and chemical luminescence are the most common ozone sensors suitable for rocketsonde use.

Table 1 presents an estimate of the current status of the more common sounding rocket sensors.

It would obviously be desirable to get as many as possible of the various measurements on a single flight although some, such as density, may be derived when others are known.

The major factor apparent at this point is the desirability of retaining a reasonable amount of instrument package installation flexibility in the design of the payload compartment. If the size is overly restrained, end item instruments may not fit, even though significant size reductions in electronic components are made by employment of solid-state circuitry.

Table 1. Sensor State of the Art

Atmospheric Parameter	Sensor	Accuracy
Temperature	Bead thermistor	2-4%
Pressure	Hypsometer	1%
	Ionization gauge	2%
Density	Falling sphere	
	Solid	1%
	Inflated	2%
Ozone	Chemical luminescence	1.0 parts per billion

GROUND STATION MODEL

In addition to the desire for maintaining instrument package flexibility, the payload must provide overall compatibility with the ground tracking and receiving equipment. Attention was focused on the AN/GMD-2 Rawin Set for use as the ground station model, because it is a relatively small, dual-purpose system (in that tracking and data receiving capabilities are combined in one unit). Separate radar tracking systems are not needed; the equipment requirements for remote area operation are thus minimized.

The AN/GMD-2 Rawin Set, a radiosonde recorder (such as the AN/TMQ-5), and a-c power generation equipment comprise the model ground station chosen and illustrated in Figure 2. The AN/GMD-2 main assembly is approximately 10 feet high and occupies a 7-by-7-foot area.

The antenna, under control of the antenna positioning system, automatically tracks a transponder-type radiosonde set. During tracking, the ranging system generates a 400-to-406 megacycle continuous-wave carrier and modulates it with an 81.94-kilocycle subcarrier. This is a ranging signal that is then transmitted by the antenna system to the radiosonde set. A pulsed 1680-megacycle signal carrying the 81.94-kilocycle modulation is returned by the radiosonde set, received by the antenna system, and sent to the receiving system. This system demodulates the radio frequency signal to separate position data, range data, and meteorological data. The position data are sent to the antenna positioning system for

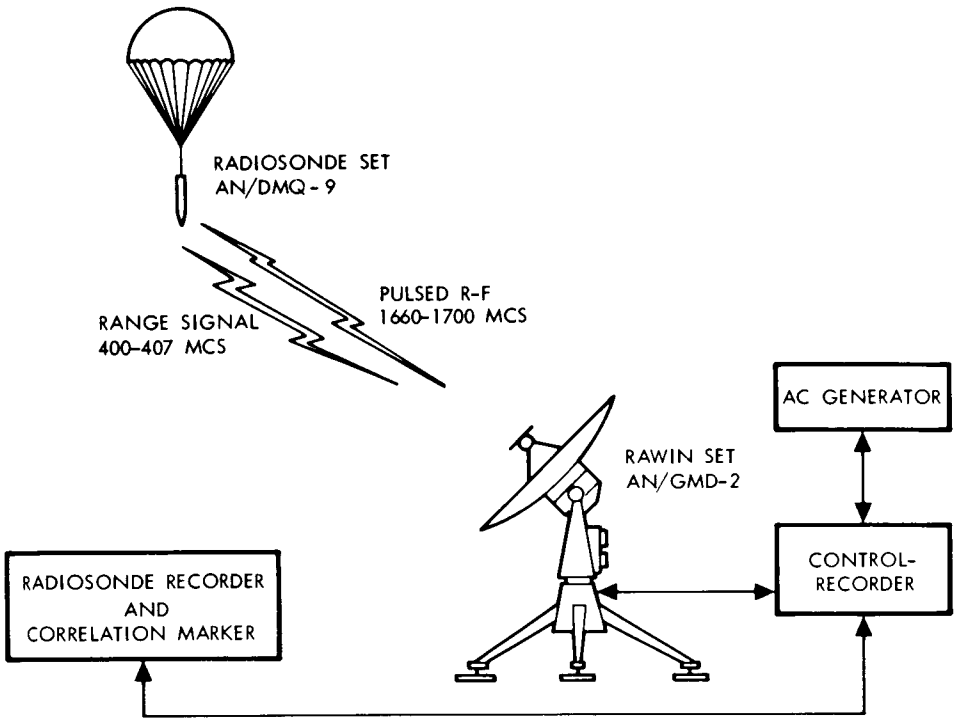

Figure 2. Ground Station Complex

precise antenna control and for data relay to a recorder. The range data (ranging subcarrier) is sent to the ranging system for measurement of slant range. An altitude computation and the recording of the range and position data from both ranging and antenna positioning systems are made by the recording, computing, and indicating system. The pulsed meteorological data are sent from the receiving system to the meteorological data transmission system for the necessary processing before recording on external equipment. The power and metering system is composed of component power supplies and the indicators used to monitor the equipment during operation and maintenance.

Pertinent characteristics of the AN/GMD-2 include:

Elevation tracking angle	3 to +90 degrees
Azimuth tracking angle	360 degrees
Maximum azimuth rate	6 degrees per second
Maximum elevation rate	6 degrees per second

The earlier AN/GMD-1B Rawin Set can be converted to an experimental GMD-2 configuration.

PAYLOAD MODEL

Four potential payloads appeared generally compatible with the AN/GMD-2 ground system:

1. AN/DMQ-6
2. AN/AMQ-21
3. AN/DMQ ( ) (XE-1)
4. AN/DMQ-9

The DMQ-6 is a miniaturized and ruggedized vacuum tube radiosonde designed to withstand the severe environment of rocket flight. It was developed by the U.S. Army Signal Research and Development Laboratories and is manufactured by the Atlantic Research Corporation for use in its ARCAS rocket system. The DMQ-6 consists of four components:

1. Modified AN/AMT-4A radiosonde transmitter
2. Modified AN/AMQ-9 radio receiver
3. Battery pack
4. Commutator switch

Although the DMQ-6 appeared compatible with payload requirements, it was deleted from further consideration because investigation indicated that it is being phased out.

The AN/AMQ-21 is a two-channel hybrid radiosonde packaged in a modified AN/AMT-4 radiosonde package. The two channels incorporate an FM-FM telemetering system to produce a continuous record of both temperature and humidity. From an economical standpoint, however, it was believed that the limited information obtained from the AMQ-21 would not justify its incorporation on the sonde.

The AN/DMQ( ) (XE-1) does not have this limitation, for it continuously transmits four channels of information. Of the four payloads, the DMQ( ) (XE-1) is the most flexible because of its modular construction. The meteorological sensors can be plug-in or plug-out, and, as new sensors are developed, they can be incorporated readily. The DMQ( ) (XE-1) is

not compatible with the GMD-2 ground tracking system without additional equipment—a four-channel subcarrier frequency filter and a four-channel magnetic tape recorder. The preference against modification of the ground equipment coupled with the belief that the DMQ( ) (XE-1) is still in the experimental stages tends, however, to rule it out for near-term use.

The most promising package is the AN/DMQ-9. Very limited information is available at this time, but all indications are that it is superior to the DMQ-6 in many respects. The DMQ-9 was developed by the Friez Instrument Division of the Bendix Corporation and is a hybrid radiosonde. It is expected to be made operational soon.

It is designed to be compatible with (approximately) a 4.5-inch-diameter rocket. Its elements are arranged so that the center of gravity lies on the axis. A threaded stud protruding from the base plate allows the nose cone to be screwed onto the launch rocket.

A lead ballast is located at the top of the stacked module. The ballast has an off-center slot and may be rotated to obtain spin-balance of the payload.

The individual modules have cylindrical shells of glass fiber, and electrical connections are made by soldering to swaged terminals. Interconnections between modules, except for the battery, are then made by a wire harness. The connector is secured with safety wire.

Noncorrosive materials are used throughout, and all modules are encapsulated in foam potting compound for vibration and shock resistance. The battery is inserted in a glass fiber shell having a removable section or door. This battery, made by the Eagle Picher Company on special order, is insensitive to altitude depressurization. It is easily activated and inserted in the sonde (payload); the whole process requires about five minutes. Once activated, the battery's standby life is three to five hours.

The AN/DMQ-9 also appears to offer growth capabilities in the amount and type of end instrumentation that can be adapted, and was chosen as the model payload for purposes of this study.

It is of interest to note that the payload compartment sizing dictated by this selection also provides compatible space requirements for the DMQ-6 and XE-1.

In investigating the potential application of the various payloads, a reported problem of fading or loss of telemetry signal during the latter

portion of ascent and initial descent phases of the AN/DMQ-9 was encountered. Preliminary investigation indicated that the orientation of the 1680 MC antenna may be the cause of the intermittent problem.

The antenna is circumferentially distributed along the sonde, and a null will, theoretically, show up on either end of the sonde along the flight vector. Nonsmooth and odd reflecting surfaces will have an influence on the null pattern and shape. More important, an antenna null in the direction of the flight vector is detrimental to system performance in this case. It appears that maximum signal would be realized if the orientation of the AN/DMQ-9 antenna were changed. A more detailed trade-off study that considers possible antenna pattern changes and/or physical orientation changes (with consideration of sensor interference problems) is recommended.

A dart-type payload section was also considered because of the apparent performance advantages to be gained with the characteristically smaller diameter (1.5-2 inches) instrument compartment. Because of its restricted size, however, the desired flexibility of end instrument interchange is not attainable. Temperature (and, of course, wind) measurements are the only foreseeable capability. It was not, therefore, considered as a candidate for this study.

With the payload instrument selected, the design objectives of the vehicle itself can be reviewed.

MAJOR DESIGN OBJECTIVES

Performance

Payload apogee will be 65+10, -3 kilometers. Attainment of this apogee band will be possible when launching in the surface environments and under the operational constraints listed below. Reliability of altitude achievement will be at least 95 percent.

Surface Conditions

Operational capability will be maintained under prefire temperature exposure between -30 F and 110 F for periods of up to one-half hour.

Apogee performance will be maintained during launchings in the following wind environments and under the listed constraints:

1. Nonwind-weighted firings in surface winds up to 30 feet per second and an altitude wind profile described by the 50 percent January binormal elliptical wind profile of Reference 1.

2. Wind-weighted firings in surface winds up to 58 feet per second and an altitude wind profile described by the 99 percent January binormal elliptical wind profile of Reference 1.

The referenced wind profiles are shown in Figure 3. Data on wind profiles above 90,000 feet were obtained from NASA report MTP-AERO-61-48, dated 8 June 1961. Subsequent data may be found in MTP-AERO-63-8, dated 28 January 1963, and NASA TMX 53023, dated 13 March 1964. Supplementary, near-surface wind envelopes are depicted in Figure 4.

Launch Angle Restrictions

The effective launch elevation angle will not exceed 80 degrees. The actual launch elevation angle, due to wind-weighting procedures, will not exceed 83 degrees.

Impact Dispersion

The vehicle will be amenable to wind-weighting technique application so that the wind-weighted 3-sigma circular dispersion of the expended booster (or, in the malfunction case of a nonseparated booster and payload, the combination) does not exceed 20 nautical miles about the nominal impact point.

Vehicle Stability

The vehicle will be aerodynamically or gyroscopically stable until payload ejection. Vehicle spin rate at payload ejection should not exceed ten revolutions per second.

Aerodynamic Heating

The vehicle will be capable of withstanding the aerodynamic heating environment without jeopardizing structural or aerodynamic integrity or exceeding the temperature limitation of the telemetry components.

System Handling Capabilities

The vehicle system, or stages thereof, must be light enough to be hand portable by three men.

The vehicle system will be capable of being assembled with minimal mechanical handling equipment.

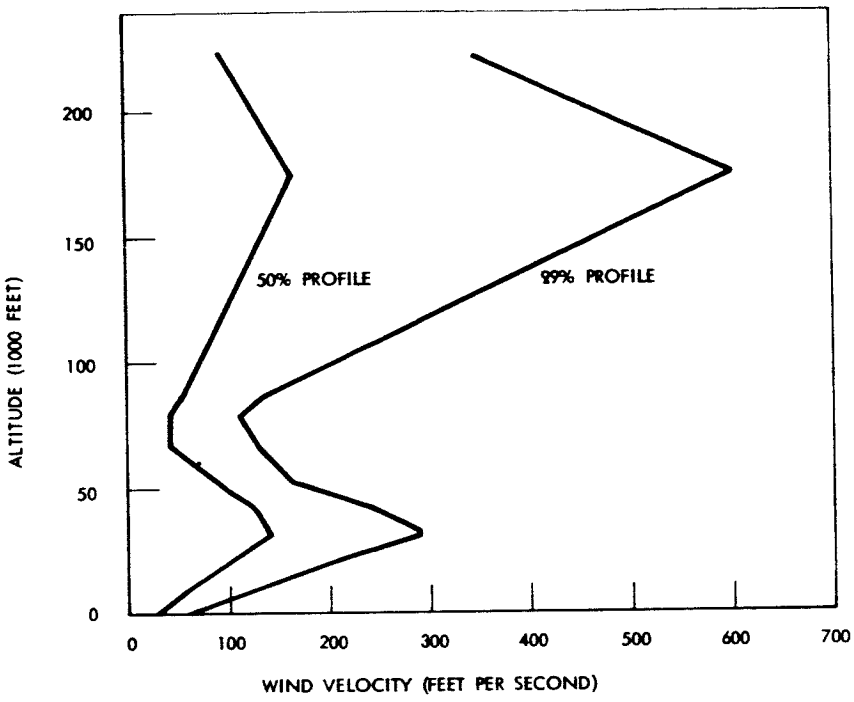

Figure 3. Design Wind Profiles

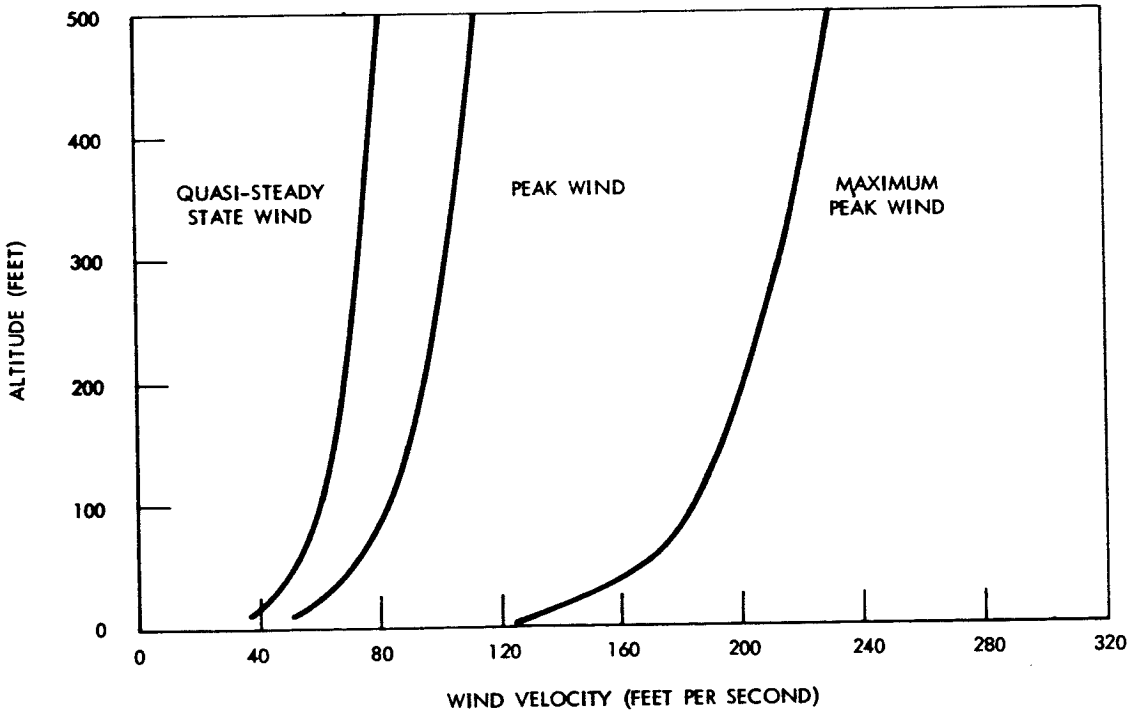

Figure 4. 99 Percent Surface Wind Envelopes—Wallops Island

Ground Equipment Compatibility

The vehicle system will be compatible with ground tracking and receiving equipment. (For purposes of this study, the AN/GMD-2 Rawin Set is used as the receiving and tracking system model.)

The foregoing requirements, then, form the basis for evaluation of the various vehicle system approaches considered in this study. For each case, payload was considered identical.

SYSTEM EVALUATION STUDIES

The major question to be answered is, "What systems approach most optimally fulfills the requirements of the synoptic meteorological sounding rocket when all constraints imposed upon the system are considered?" The preceding section outlined the requirements and constraints pertinent to this study. This section deals with the results obtained from trade-off studies in the areas of relative performance, reliability, cost, and other influencing factors associated with four basic systems approaches:

1. A single-stage system with the payload attached to near-apogee conditions

2. A single-stage system with a nonpropulsive payload separated subsequent to motor burn-out

3. A continuous-burn, dual-thrust-level system with payload separated near apogee

4. A two (propulsive)-stage system with the payload separated from the second stage near apogee

Certain of these basic system approaches give rise to subclassifications that must also be examined. For example, the single-stage system approach requires consideration (and subsequent selection) of a radial-burn motor of relatively high thrust-to-weight ratio or an end-burning motor in the more moderate thrust-to-weight ratio realm. With the two-stage system, coast time between first-stage burn-out and second-stage ignition may be of value; hence, various levels must be examined.

Growth potential for the attainment of higher altitude was another factor considered. This aspect is discussed in more detail in Volume II.

SYSTEM PERFORMANCE COMPARISONS

Reliable achievement of the design apogee altitude under the rather severe environmental influences previously discussed is of paramount concern. Therefore, the varied aspects of basic system performance afford a logical starting point in the comparative evaluation of the candidate system approaches. Before considering any specific system, however, a delineation of what comprises the state of the art relative to general motor performance is in order. In addition, a close look at the governing design influences that

affect performance, regardless of system approach, will provide a better perspective in which to consider each system.

Basic Propellant Data

A summary of performance characteristics (specific impulse) and burn rates attainable with representative propellants manufactured in the United States is shown in Table 2. Propellant density and chamber temperature at nominal chamber pressure (1000 psia) are also noted. As indicated, two propellants listed (ARCITE 368 and 373) display uniquely higher burn rate values that are obtained by imbedding silver-wire slivers longitudinally (in the end burning design) in the propellant grain structure. The higher values of the nonaluminized Arcite 368 propellant are attributed to its higher oxidizer content (81 percent NH_4ClO_4), compared to the aluminized Arcite 373 (59 percent NH_4ClO_4).

Also of interest in Table 2 is the comparison of theoretical specific impulse to actual delivered values. The relatively low propellant mass flow rates and low total weight of on-board propellant for the class of vehicle considered in this study appear to result in some degradation in delivered specific impulse. While the exact value of delivered specific impulse will be dependent upon the particular propellant make-up, the average value indicated by the data of Table 2 is 245 seconds and is considered representative of current state-of-the-art, industry-wide capabilities.

The referenced specific impulse of 245 seconds is based on the standard assumptions of 1000 psia chamber pressure exhausting to sea-level (14.7 psia) pressure and no nozzle divergence losses. The effect of variations in delivered I_{sp} with changes in chamber pressure, nozzle area ratio, and altitude are shown in Figure 5.

Before applying these basic propellant/motor data to specific system approaches, it appears worthwhile to consider certain criteria that will have major impact on the performance attained, regardless of approach.

Governing Factors

Particular configuration details and system approaches are of major importance in developing vehicle performance that meets the altitude achievement requirement, but certain factors are, in a broad sense, relatively independent of configuration specifics and apply to any system approach.

The synoptic sounding rocket has been, classically, a noncontrolled vehicle. (The inclusion of a control system should not be considered entirely out of the question, but the drive for minimum system complexity and minimum cost must preclude such an addition except as a last resort.)

Table 2. Representative Current Propellant Characteristics

Propellant	Density ($lbs/in.^3$)	Specific Impulse (sec)		Chamber Temperature (F)	Burn Rate (in./sec)
		Delivered	Theoretical		
Arcite 402	0.0640	232	258	5565	0.40
Arcite 368	0.0620	237	248	4685	2.60*
Arcite 373	0.0640	242	266	5600	1.90*
TRX-G415	0.0624	240	271	5475	0.277
TRX-H609	0.0636	236	264	5550	0.340
TP-G3014A	0.0625	235	263	5325	0.270
TP-H1001	0.0638	237	263	5710	0.320
ANP-2864HG	0.0637	243.7	261.5	5650	0.365
ANP-2862JM	0.0635	243.2	261.6	5640	0.28
ANP-2803HG	0.0635	251	262	5605	0.31
ANP-2716HL	0.0619	241	259	5460	0.285
ANP-2805HY	0.0625	240	265	5540	0.34
DDP-80	0.0644	250	264	6565	1.00
CYI	0.0635	247	267	6410	0.55
EJC	0.0654	254.5	271	6580	0.62
EFR	0.0658	252.5	270	6720	0.78
PFG_s	0.0682	—	276	6850	0.60
RDS-501	0.0630	247	266.3	5688	0.33
RDS-502	0.0650	247	265.8	6090	0.40
RDS-504	0.0630	245	264.4	5542	0.65
RDS-505	0.0666	248	264.8	6314	0.32
LPC-547	0.0628	244	261	5515	0.87
LPC-549	0.0636	246	264	5753	0.32
LPC-1003A	0.0616	246	262	5924	0.86
LPC-1005A	0.0628	250	266	6191	0.47
LPC-1008A	0.0670	255	272	6350	0.40

*Silver-wire imbedded in grain

Sea-level conditions and chamber pressure = 1000 psia

The attainment of apogee altitude is, then, largely at the mercy of the attitude of the vehicle since, once attained, there is no means available to change an undesirable attitude.

There are two governing factors that are esentially independent of system approach and that have major influence on the attitude attained by the vehicle: (1) the fact that launch is restrained to an angle less than vertical, and (2) the high surface (and near surface) wind environment in which the vehicle may be launched.

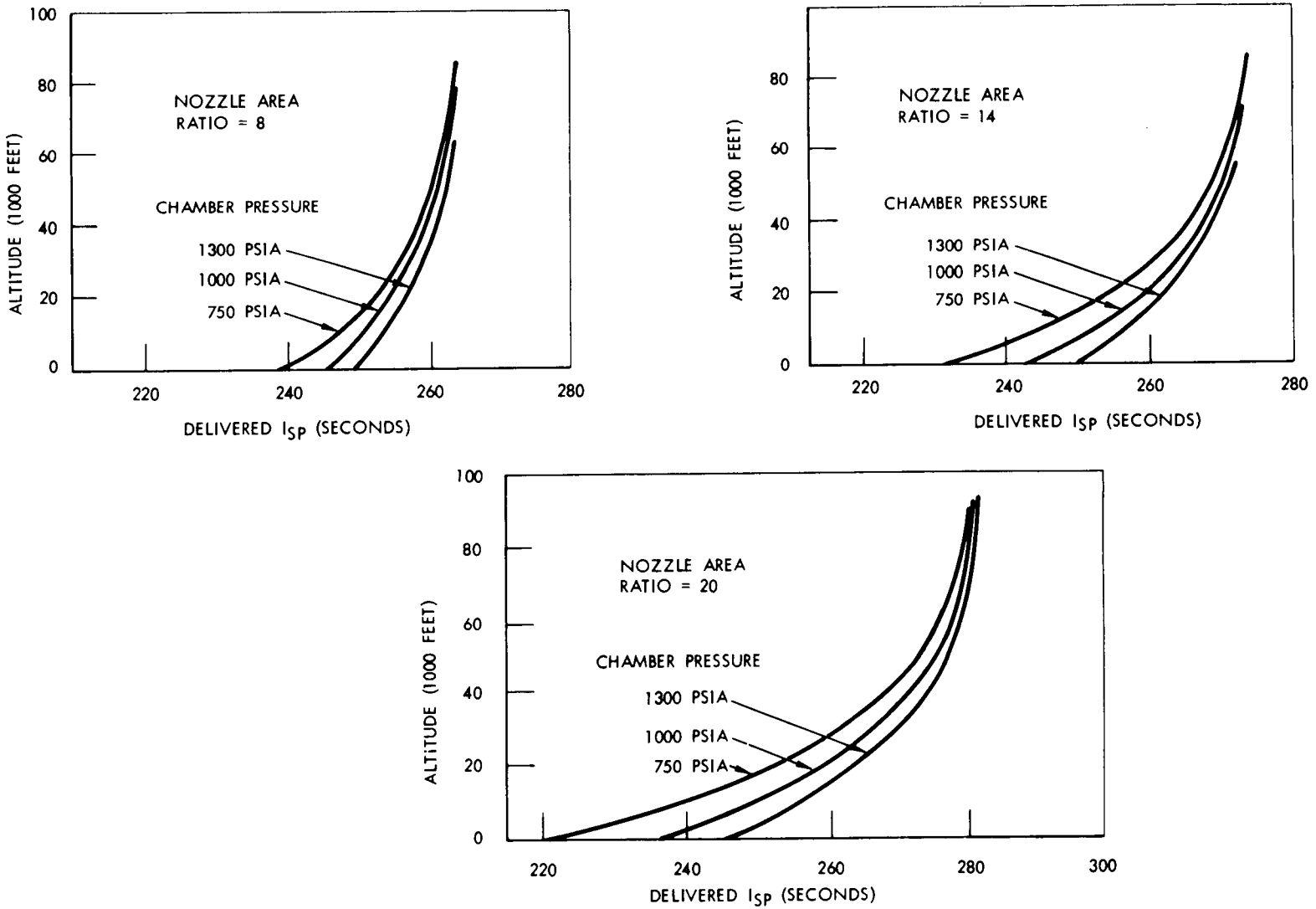

Figure 5. Parametric Motor Variations

The first item results in a weight component which produces a rate of change of vehicle flight path. The second item produces a nonaligned velocity vector which (assuming a finite static margin) will result in vehicle rotation.

Major rotational motion occurs during the initial few seconds of flight, as shown by the plots of Figure 6, which are representative of the trend exhibited by the entire spectrum of configurations investigated. Two factors that will influence the resultant altitude in a particular environment are apparent: (1) the static margin displayed by the vehicle, and (2) the velocity of the vehicle in the initial period of flight.

Figure 7 shows apogee altitude variations attained with a theoretical vehicle that, in Case 1, is forced to maintain neutral stability and, in Case 2, is forced to maintain an extremely high degree of static stability. With all other factors held constant, an apparent apogee altitude difference of approximately 30 percent is indicated. Obviously, neither extreme is realistic; however, if altitude attainment were reasonably linear with static margin, certain design approaches would be indicated. Unfortunately, the response is not in this category, as evidenced by the altitude achieved with two finite stability cases. Case 3 of Figure 7 is based upon an assumed stability that is generally representative of this class of vehicle, and Case 4 is based upon a considerably reduced margin, as indicated by the pitching moment coefficient insert. Thus, the effect of static margin relative to this problem is, essentially, a step function, and, unless a rigidly fixed neutrally stable case could be obtained in real life (which it cannot), the problem remains.

The second factor that will have major influence on the initial rotational movement of the vehicle is the velocity history. Figure 8 indicates the sensitivity of pitch attitude under the limit design wind conditions as a function of launch velocity. (In the context used here, launch velocity is the speed of the vehicle at the time it is free to respond to the wind environment.) The attitude attained at two seconds after launch is used as the reference point for comparison.

The sensitivity of apogee altitude to launch velocity and wind environment is also depicted in Figure 8. While the absolute magnitude of apogee altitude is dependent upon the characteristics of the specific configuration considered, the trend shown is valid for all cases. Responses of the various system approaches are discussed in more detail in subsequent portions of this section.

Launch velocity, then, is the major tool available for use in solving the problems associated with launches in the severe wind environment. The attainment of the necessary velocity, however, leads to other problem areas. During the time the vehicle is building up to the required velocity, it must

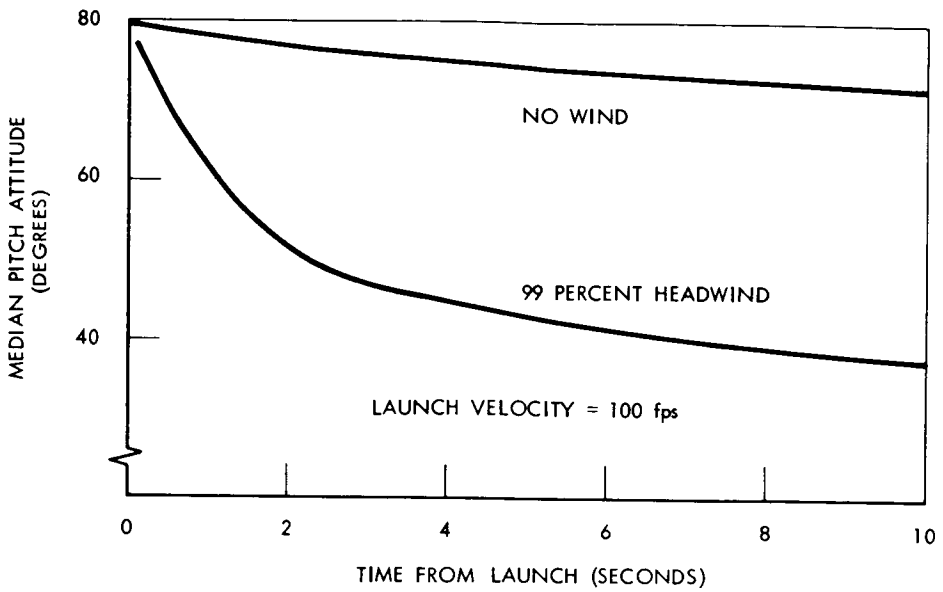

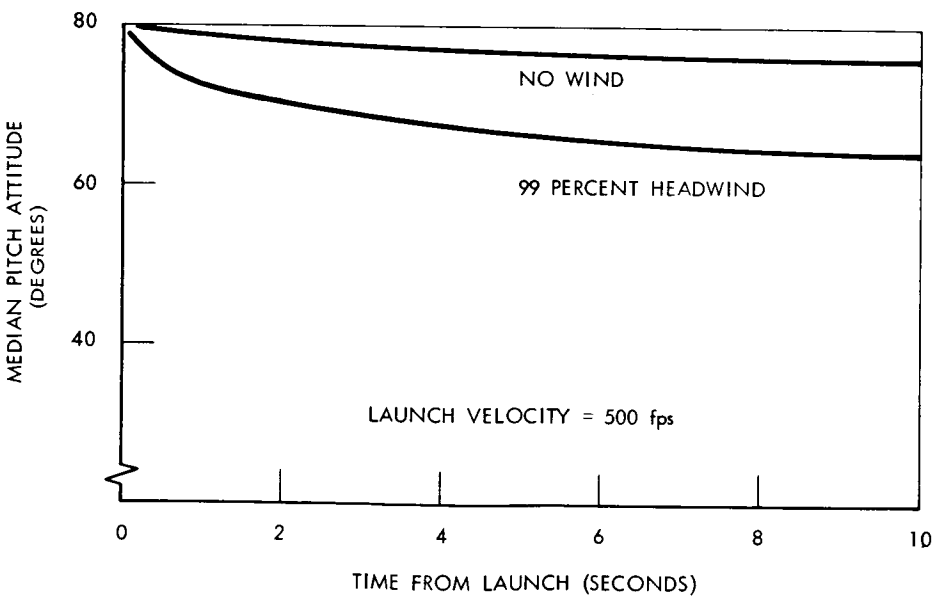

Figure 6. Initial Attitude Response

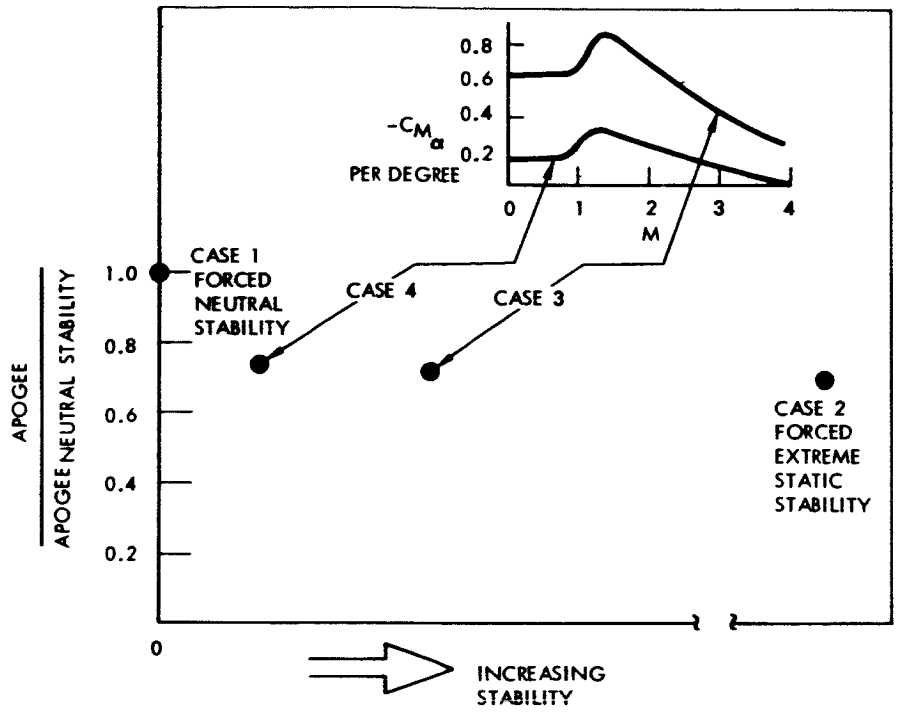

Figure 7. Apogee Versus Vehicle Stability — 99 Percent Headwind

be constrained by a launcher mechanism. Feasible length limitations of the launcher subsystem dictate the initial acceleration history of the vehicle, which, in turn, may place stringent requirements on the capabilities of the payload subsystem. If successful launch and apogee altitude attainment are to be achieved within the constraints and environments designated, however, a launch velocity in the 400-to-500-feet-per-second region must be maintained. These and other considerations will be examined in more detail in subsequent sections.

Single-Stage System

In evaluating applicable single-thrust-stage system approaches, two major subclassifications will be considered:

1. The general type of motor—radial or end-burning
2. The separation altitude of the payload—in the near burn-out region or in the near-apogee region

Before examining these subclassifications and the trade-offs associated with them, consider the general energy management problem associated with the single-stage system.

Assume that an apogee altitude of 213,000 feet (65 kilometers) and a corresponding velocity of approximately 1000 feet per second is desired. The energy-to-weight ratio (E/W) required to meet these conditions

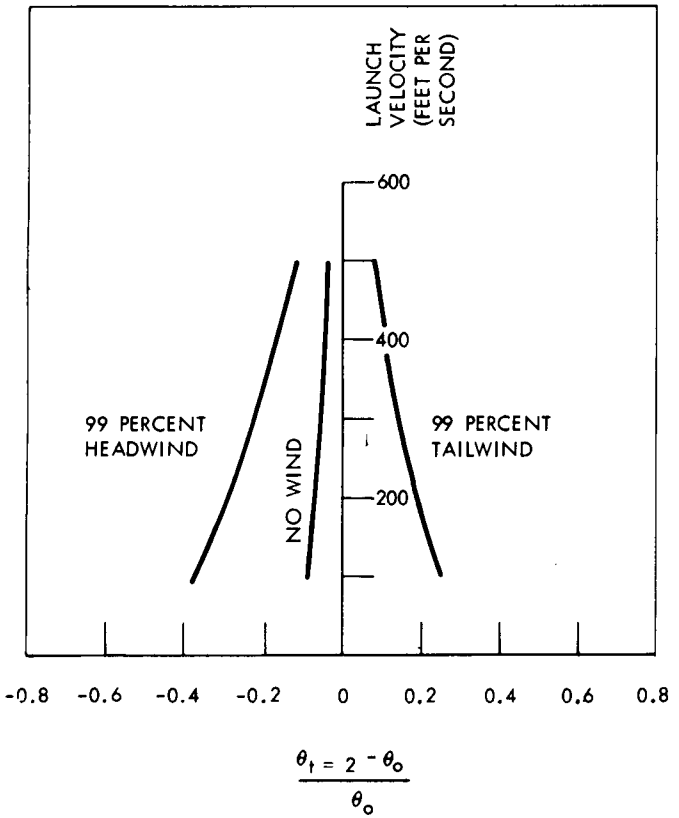

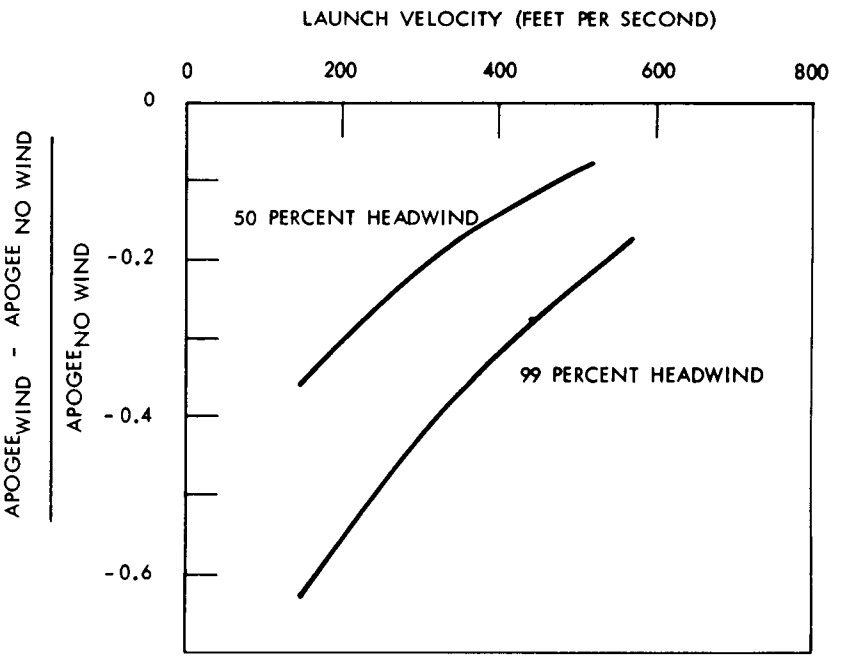

Figure 8. Representative Wind Sensitivity

is, of course, the weight normalized sum of the potential and kinetic energy conditions:

$$E/W \doteq h + \frac{V^2}{2g}$$

which, for the assumed values, equals 230,000 feet. Figure 9 shows the altitude-velocity relationship for lines of constant E/W in the U.S. standard atmosphere of 1962. Superimposed upon the figure are lines of constant dynamic pressure and traces that are indicative of the velocity losses associated with bodies of various weight-to-drag ratios. These latter traces are superimposed in such a manner that the resultant velocity at approximately 70,000 feet provides the desired E/W ratio of 230,000 feet. This altitude was chosen because above this altitude, drag losses are minimal and can be ignored for comparative purposes. The major element to be gleaned from this figure is the altitude-velocity relationship that must exist at the time of motor burn-out. For example, if the body has a W/C_DA equal to 1500 pounds per square foot and a burn-out altitude of 40,000 feet is achieved, the velocity at that point must be approximately 3740 feet per second if the apogee conditions are to be attained. For the same body, a velocity of 5000 feet per second must be achieved if burn-out occurs at 15,000 feet.

With this general picture in mind, the properties required for the inherently short-duration, radial-burn motor can be examined.

Radial Burn Motors

Shown in Figure 10 are the approximate initial thrust-to-weight (T/W) ratios and corresponding burn times of various sounding rocket configurations. As indicated, a relatively wide range of values is spanned with a majority grouping of radial-burn systems in the region of T/W's between 20 and 40 and burn times in the 1.5-to-2.5-second category.

These background data are useful in establishing a feel for existing capabilities. The particular requirements of this study may, however, lead to different situations. The required burn-out velocity-altitude relationship for an assumed single-stage configuration can be estimated from Figure 9. For reasonable values of W/C_DA, burn-out velocities on the order of 4500 to 6500 feet per second are indicated. Drag and gravity will result in velocity losses during the short-duration burn period of about 1000 to 2000 feet per second; thus, an ideal velocity in the region of 6500 to 7500 feet per second must be generated by the motor.

As a check, consider the initial trajectories attained with vehicles representing both ends of the radial-burn spectrum. The altitude-velocity

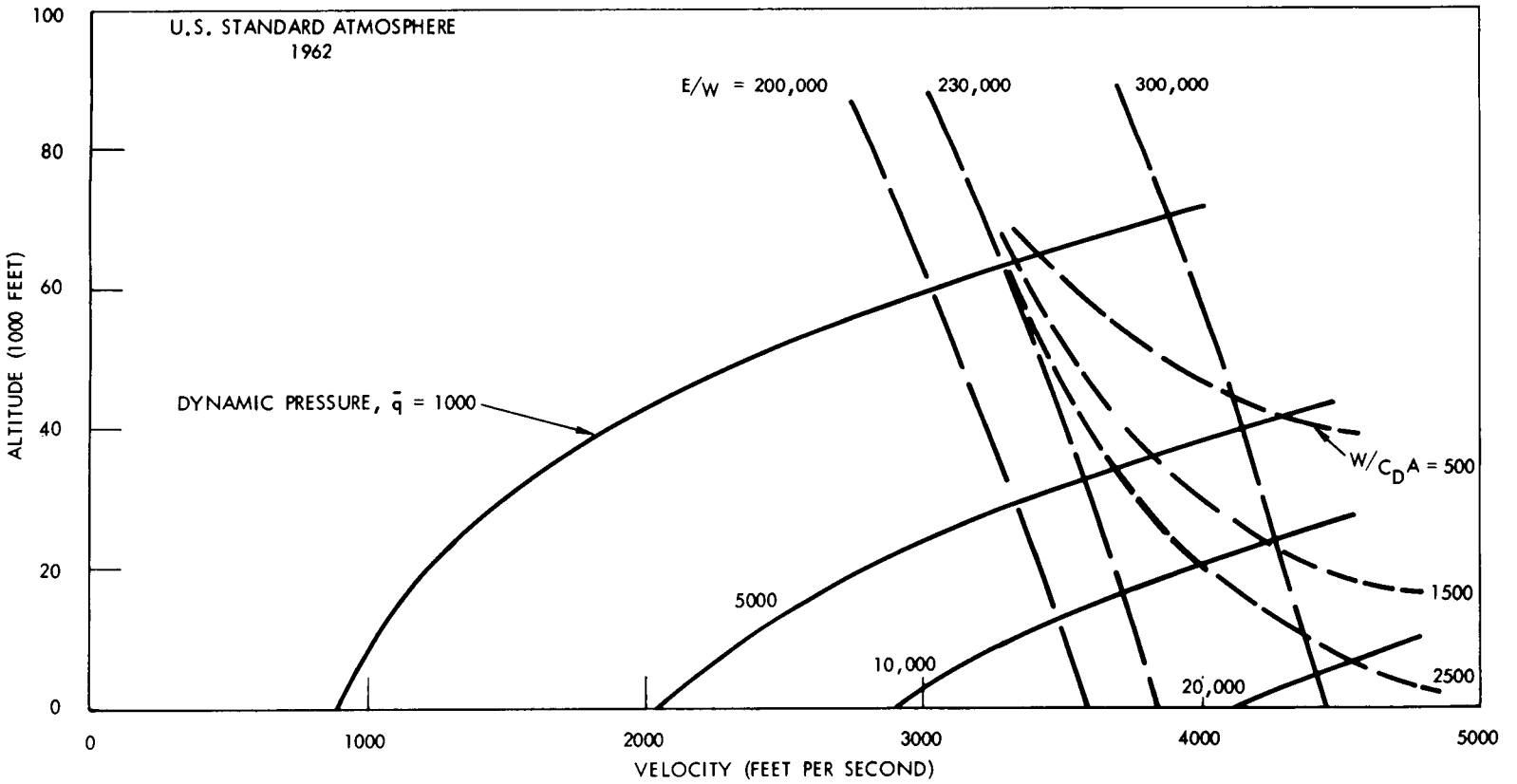

Figure 9. Energy Relationship

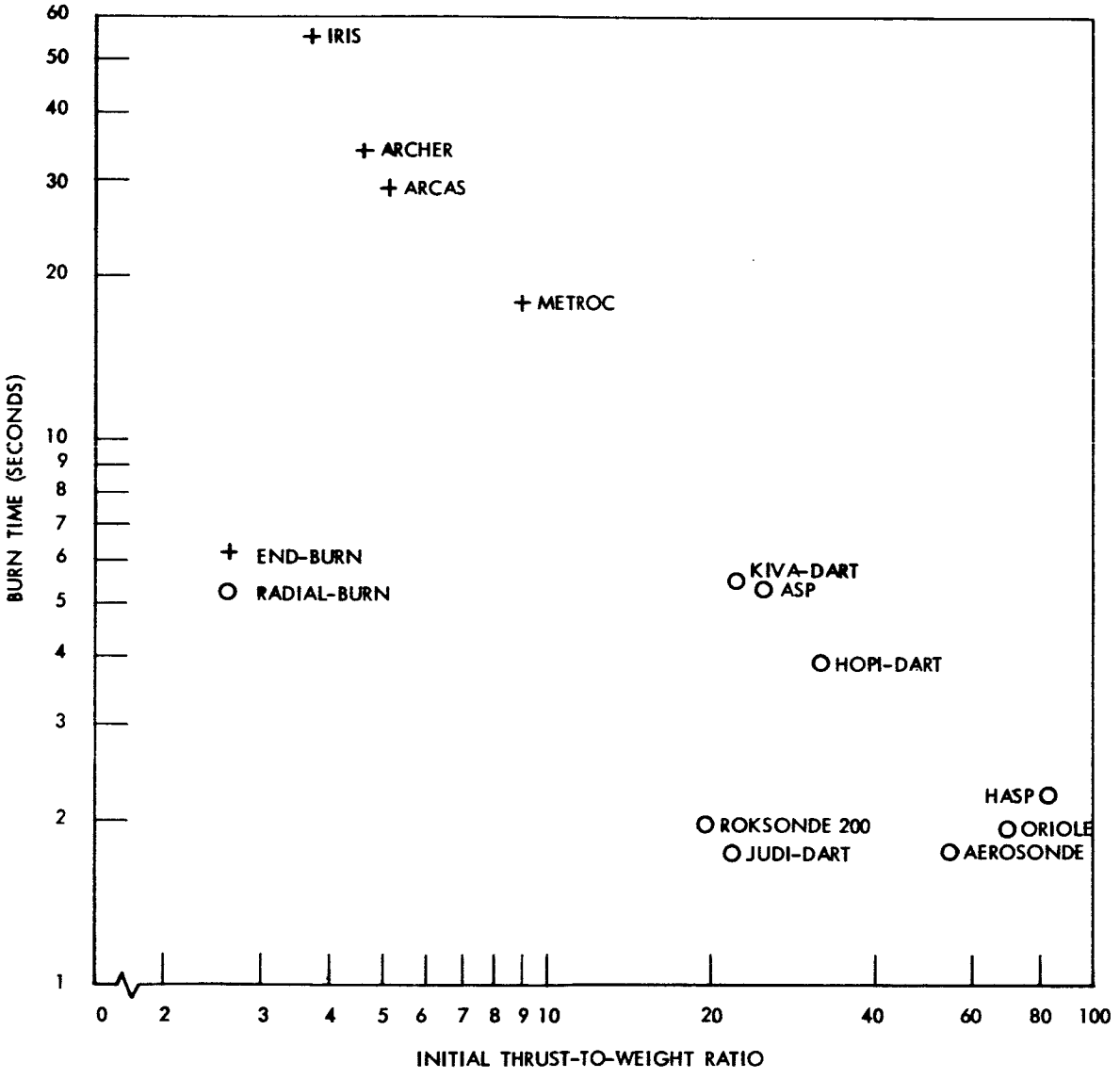

Figure 10. Representative Thrust-to-Weight and Burn-Time Characteristics

profile for a theoretical vehicle that has a thrust-to-weight ratio of 30 is shown in Figure 11. The required altitude-velocity relationship for coast from burn-out is reached approximately 6.5 seconds after launch at an altitude of 16,500 feet. In this case, drag and gravity velocity losses amount to 1400 feet per second, which, when summed with the required velocity of 4800 feet per second, yields an ideal velocity requirement of 6200 feet per second.

The altitude-velocity profile obtained with a higher T/W ratio of 90 is also shown in Figure 11. For this example, necessary burn-out conditions are reached at 7000 feet altitude and a velocity of 6000 feet per second. An ideal velocity of approximately 7000 feet per second is needed to overcome drag and gravity losses.

In either case, the resultant profile for this single-stage approach presents a rather severe aerodynamic heating and loads environment. In addition, the generation of sufficient propellant mass flow to obtain the necessary thrust-to-weight ratios leads to motor diameters that are considered unadvisable for this study.

The single-stage, radial-burn motor approach is, therefore, not considered practical for application to this study.

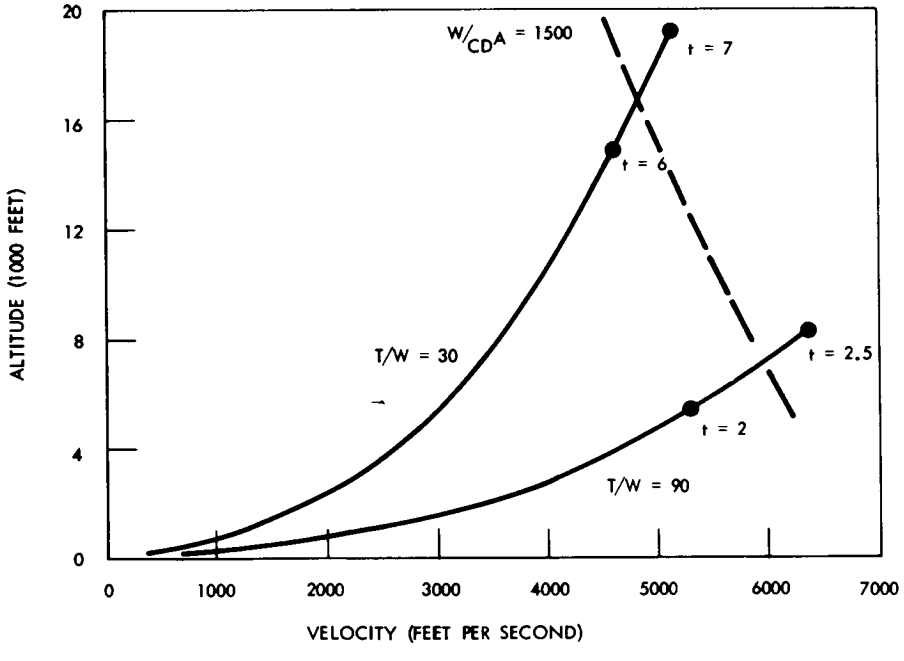

Figure 11. Initial Trajectory Characteristics — High Thrust-to-Weight Ratio

End-Burning Motors

The end-burning grain configuration provides maximum propellant loading density and, because of the longer duration and lower thrust level burn period offers more flexibility in achieving a reasonably favorable velocity-altitude history.

A survey of pertinent end-burning configurations yields the representative thrust-to-weight ratios and burn times shown in Figure 10. Although the data are somewhat limited, representative T/W ranges of 3.5 to 9 and burn times between 20 and 55 seconds are indicated. The burn-out altitude band of interest for the end-burning approach can be estimated to be in the 30,000 - to 50,00 foot region, which, referring again to Figure 9, indicates that a required burn-out velocity band of 3500 to 4500 feet per second is applicable.

Figure 12 shows, as a check of the validity of these assumptions, the altitude-velocity profiles of the initial portion of representative single-stage, end-burning configurations. In the general case, drag and gravity losses at burn-out will fall in the 2000-to-2500 feet-per-second category.

To provide a starting point for trade-off evaluation of the various parameters associated with the end-burning, single-stage motor, a theoretical vehicle with a thrust-to-weight ratio of 5 was assumed.

The motor characteristics evolved are shown in Table 3. While the final single-stage configuration incorporates a T/W greater than 5 and thus embodies different characteristics, the trends shown at this point are representative and presented as a matter of method of approach.

Table 3. Initial Single-Stage Motor Characteristics

Factor	Characteristic
Motor outer diameter	4.31 inches
Grain diameter	3.79 inches
Grain length	43.7 inches
Burn rate	1.8 inches per second
Burn time	24.3 seconds
Nozzle area ratio	14.0
Propellant weight	31.5 pounds
Chamber pressure	1000.0 psia
Sea-level thrust	315.0 pounds
Sea-level specific impulse	242.5 seconds
Sea-level total impulse	7640.0 pound-second

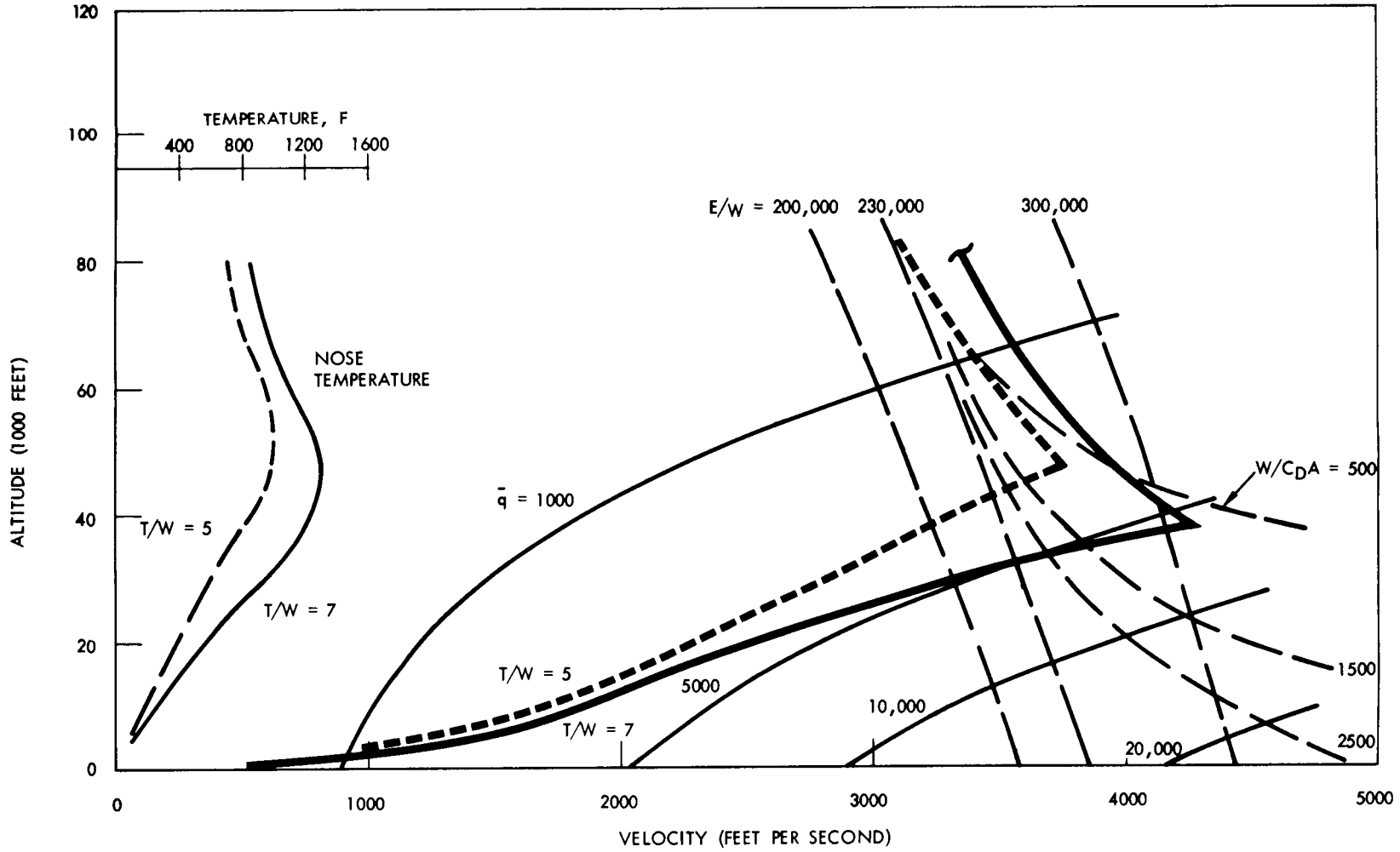

Figure 12. Single-Stage Altitude-Velocity Profiles

The nozzle geometry was defined as an 80 percent bell nozzle, and overall motor efficiency was estimated to be 96 percent. An 80 percent bell nozzle is defined as a nozzle in which the first 20 percent of the length from the throat to the exit is conical and the remainder is bell shaped.

These data can now be used as the base point for evaluation with respect to overall system performance in the design environments and within the design constraints imposed.

Near-Apogee Motor Separation

With baseline motor characteristics defined, the next step in determining overall system performance is the establishment of a baseline vehicle configuration. Estimated aerodynamic characteristics required for trajectory analysis are shown in Figure 13. These data are again presented primarily as a matter of record at this point.

One particular item is worthy of note at this time. Representative trajectory data obtained with this configuration produce a Reynolds number variation as indicated in Figure 14. In the region of interest from a drag standpoint, the restricted variation in Reynolds number results in an essentially constant (with altitude) friction drag coefficient. Thus, the total drag variation for this general case can be represented as a function of Mach number alone.

The definition of these baseline characteristics provides a starting point for the examination of the effects of variations in pertinent parameters on vehicle performance. Apogee altitude was chosen as the basic criteria against which vehicle performance would be measured. Figure 15 delineates the sensitivity of apogee altitude to the major variables. The figure also indicates the allowable apogee tolerance band. Again, the trend rather than the absolute values is of primary interest at this point.

As indicated in Figure 15, the basic T/W = 5 configuration can provide acceptable no-wind performance but, in the presence of design headwinds, fails to achieve the desired altitude band. It is also apparent that a change in only thrust-to-weight ratio will not accomplish the desired objective. However, peaking of the attainable altitude occurs at a T/W of approximately 7. In addition, the figures indicate the trends in altitude gain with other basic vehicle parameters such as mass fraction and vehicle weight. The noted effects of the two variables that can be considered relatively independent of configuration—launch velocity and launch angle—also provide some insight into gains that can be made in those areas.

Evaluation of the data indicates that an increase in thrust-to-weight ratio coupled with an increase in vehicle mass fraction and utilization of the maximum allowable launch angle may provide suitable performance in

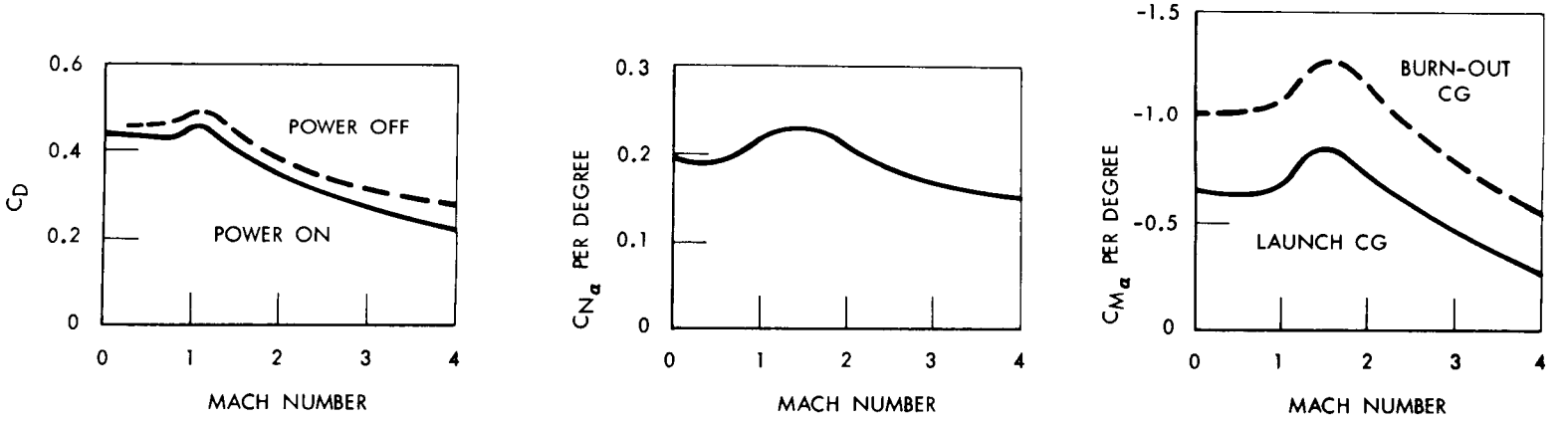

$S_{REF} = 0.102\ FT^2$
$d_{REF} = 0.36\ FT$

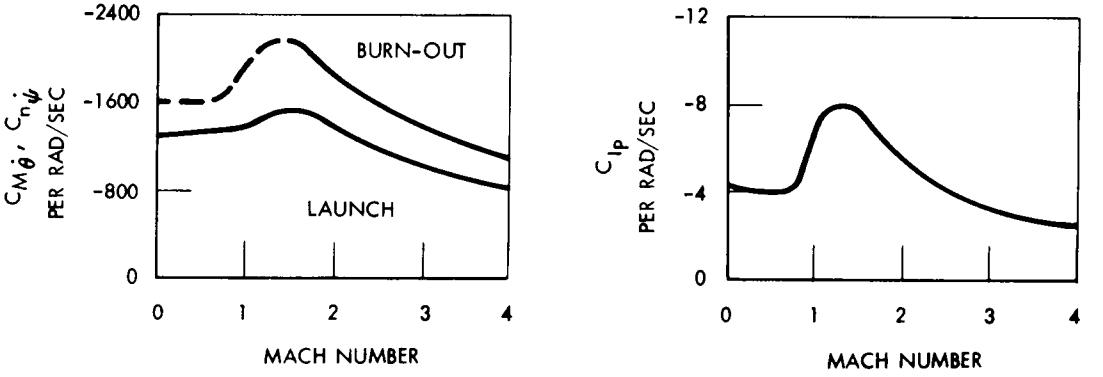

Figure 13. Initial Single-Stage Aerodynamic Characteristics

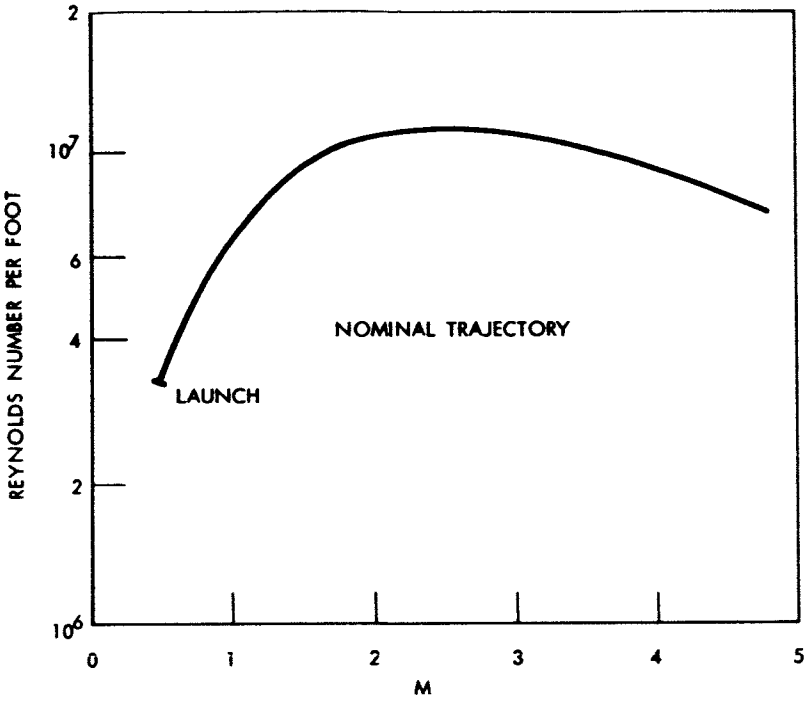

Figure 14. Nominal Reynolds Number History

the 99 percent headwind environment, provided that a launch velocity in excess of 400 feet per second is established. A second-generation vehicle embodying these characteristics can now be estimated to require the following characteristics:

$T/W \sim 7.0$
$\nu \sim 0.52$
$W_{gross} \sim 69$ pounds
γ launch ~ 83 degrees (under 99 percent headwind conditions)
$V_{launch} \sim 500$ feet per second

The increased thrust requirement is reflected in basic motor characteristics, as evidenced by a comparison of the revised values of Table 4, with those developed initially and shown previously in Table 3.

Motor diameter was increased slightly to provide overall compatibility with the forward sections of the vehicle. The increased burn rate is achieved by operation at an increased chamber pressure and utilization of increased wire concentration within the grain and decreased oxidizer particle size. The increased chamber pressure also provides an increase in delivered specific impulse without undue penalty in case construction.

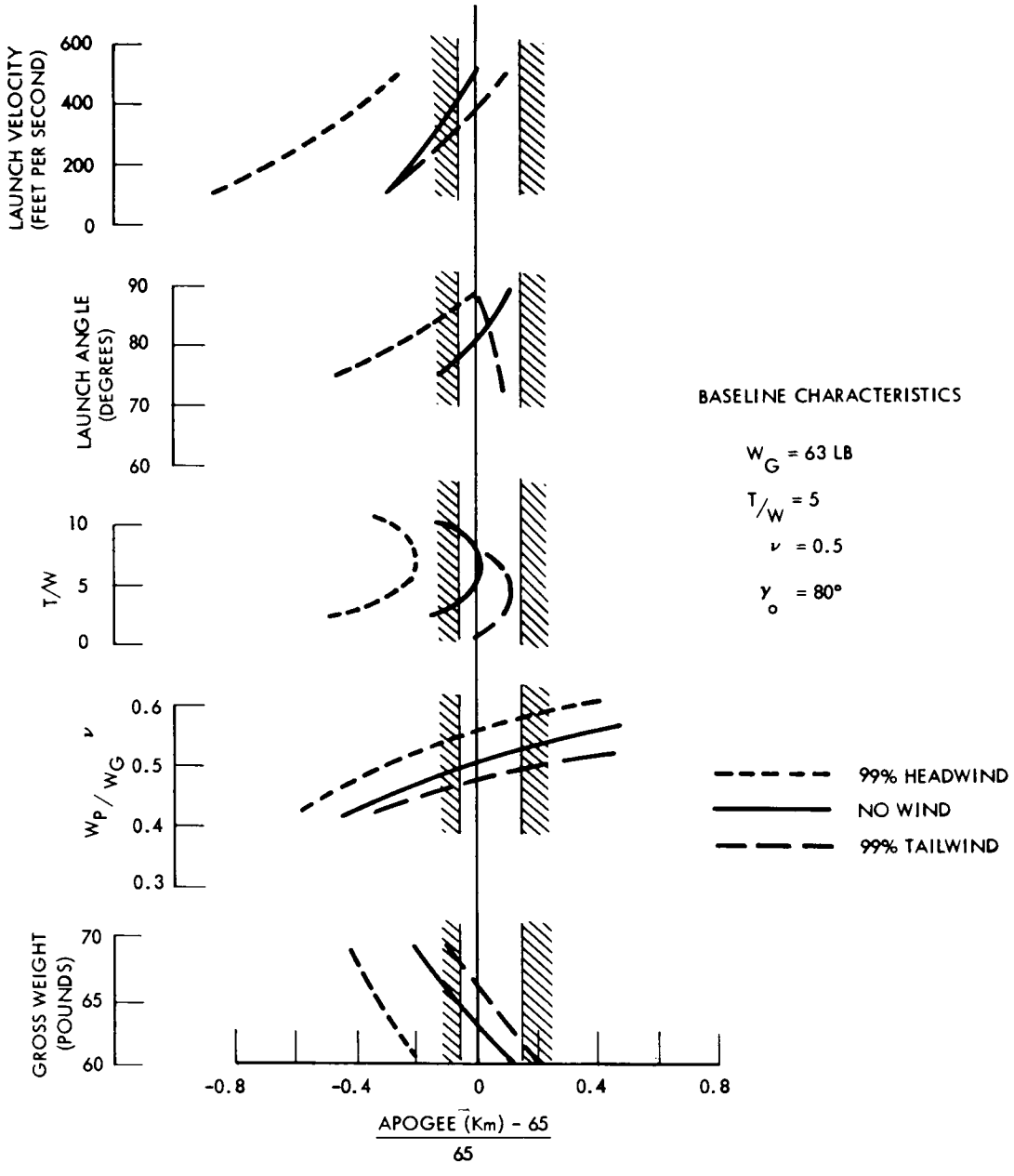

Figure 15. Initial Single-Stage Performance Trades

Table 4. Revised Single-Stage Motor Characteristics

Factor	Characteristic
Motor outer diameter	4.475 inches
Grain diameter	3.935 inches
Grain length	46.5 inches
Burn rate	2.45 inches per second
Burn time	19.01 seconds
Nozzle area ratio	14.0
Propellant weight	36.2 pounds
Chamber pressure	1250.0 psia
Sea-level thrust	473.2 pounds
Sea-level specific impulse	248.5 seconds
Sea-level total impulse	8996.0 pound-second

The motor variations are, in turn, reflected in slight modifications in the basic aerodynamic parameters. With these changes accomplished, another look at system performance sensitivity can be taken.

Figure 16 shows the normalized apogee variations attained with the revised configuration and the indicated parametric variations. Design apogee can now be attained in the presence of the maximum design headwind and within the launch angle constraints required. The requirement for a relatively high launch velocity remains, however, as should be expected when the discussion of vehicle response in the first few seconds of flight is recalled.

Iterative sizing procedures and trajectory analyses yield the final vehicle configuration, which is described in detail in the System Design section. Major characteristics include:

Gross weight: 71.4 pounds
Propellant weight: 36.2 pounds

Specific trajectory results of this candidate single-stage system can now be examined. Figures 17 through 21 present representative histories of pertinent trajectory characteristics from launch to apogee for a no-wind and a 99 percent headwind environment. (The severe-headwind case will be used for most comparative purposes, since it represents the limit-performance condition.) Figure 22 indicates the apogee attained for 50 percent and 99 percent headwind and tailwind profiles and varying launch angles. The ranges at apogee for similar wind conditions are shown in Figure 23. The apogee boundary criteria of 65 km +10, -3 km can be met under all wind

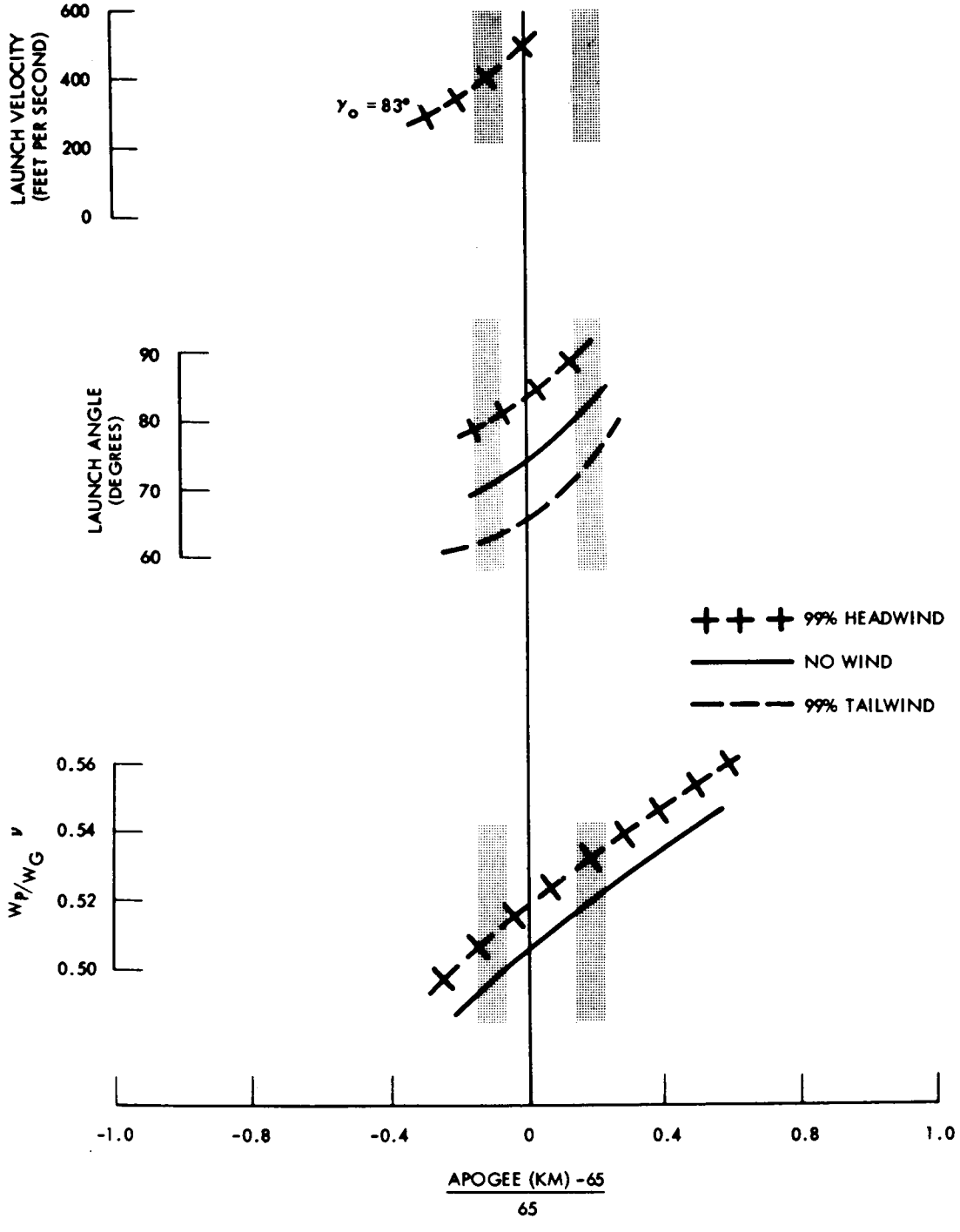

Figure 16. T/W=7 Parametric Variations

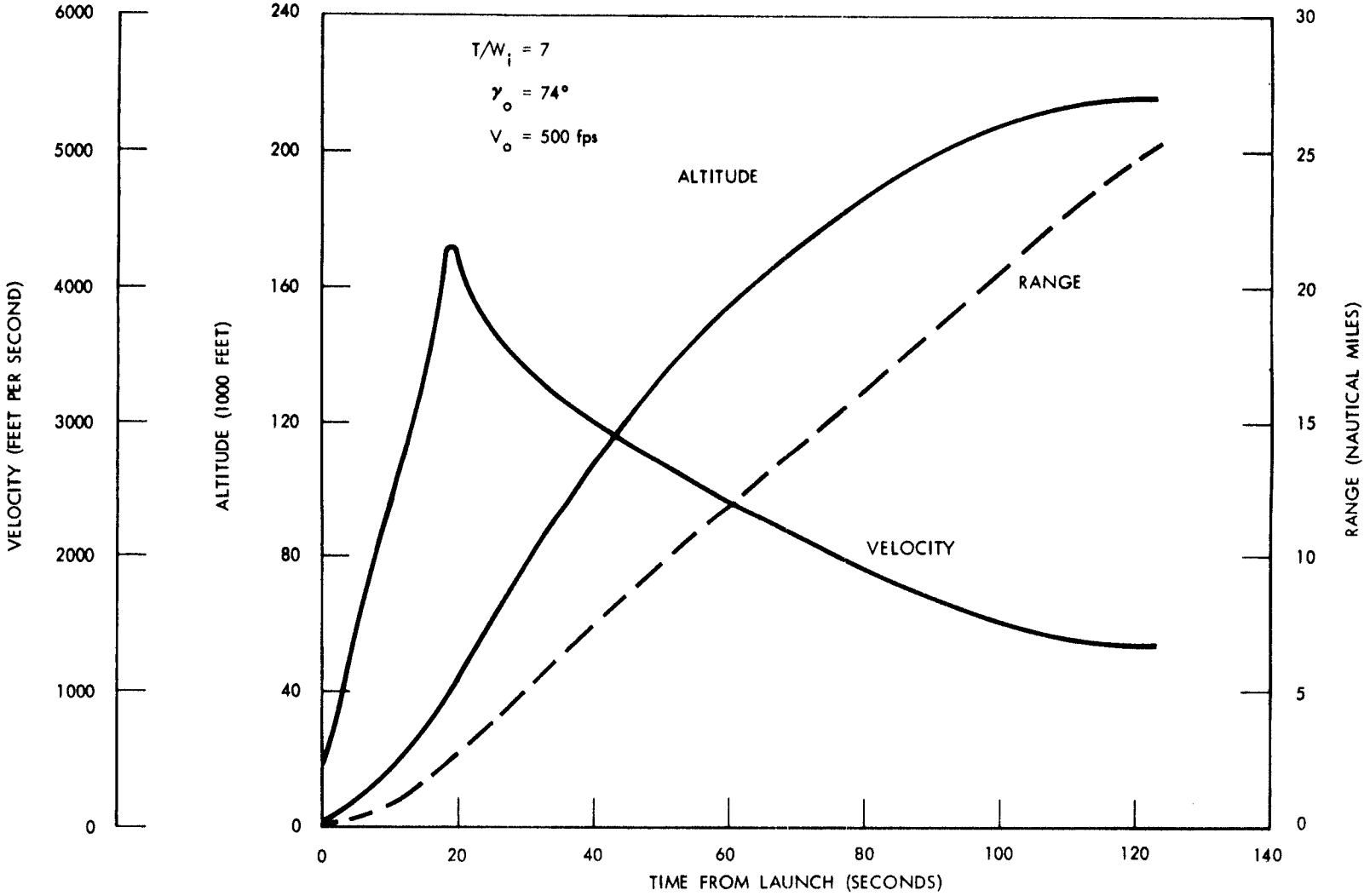

Figure 17. Single-Stage/Apogee Separation Trajectory Characteristics—No Wind

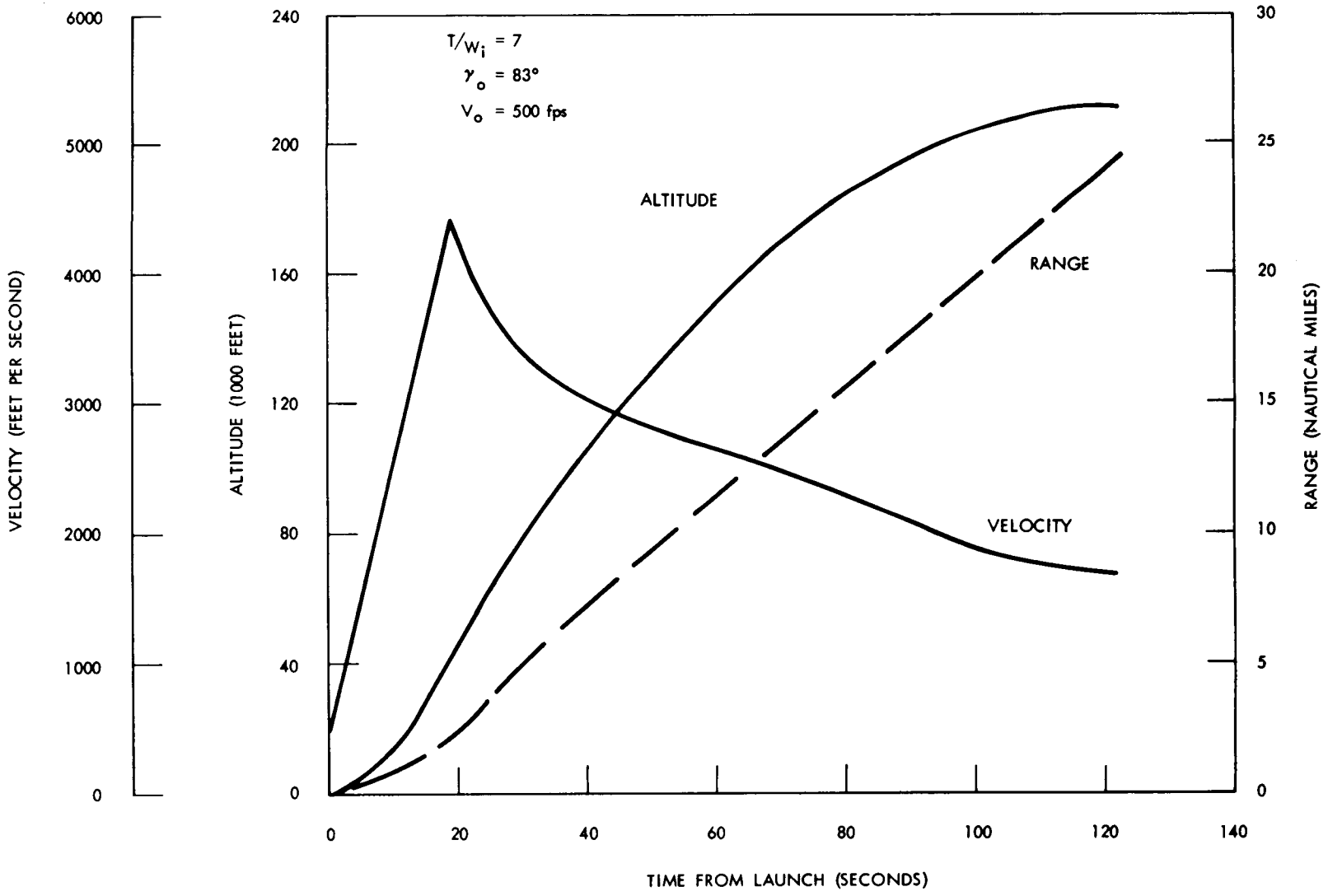

Figure 18. Single-Stage/Apogee Separation Trajectory Characteristics—99 Percent Headwind

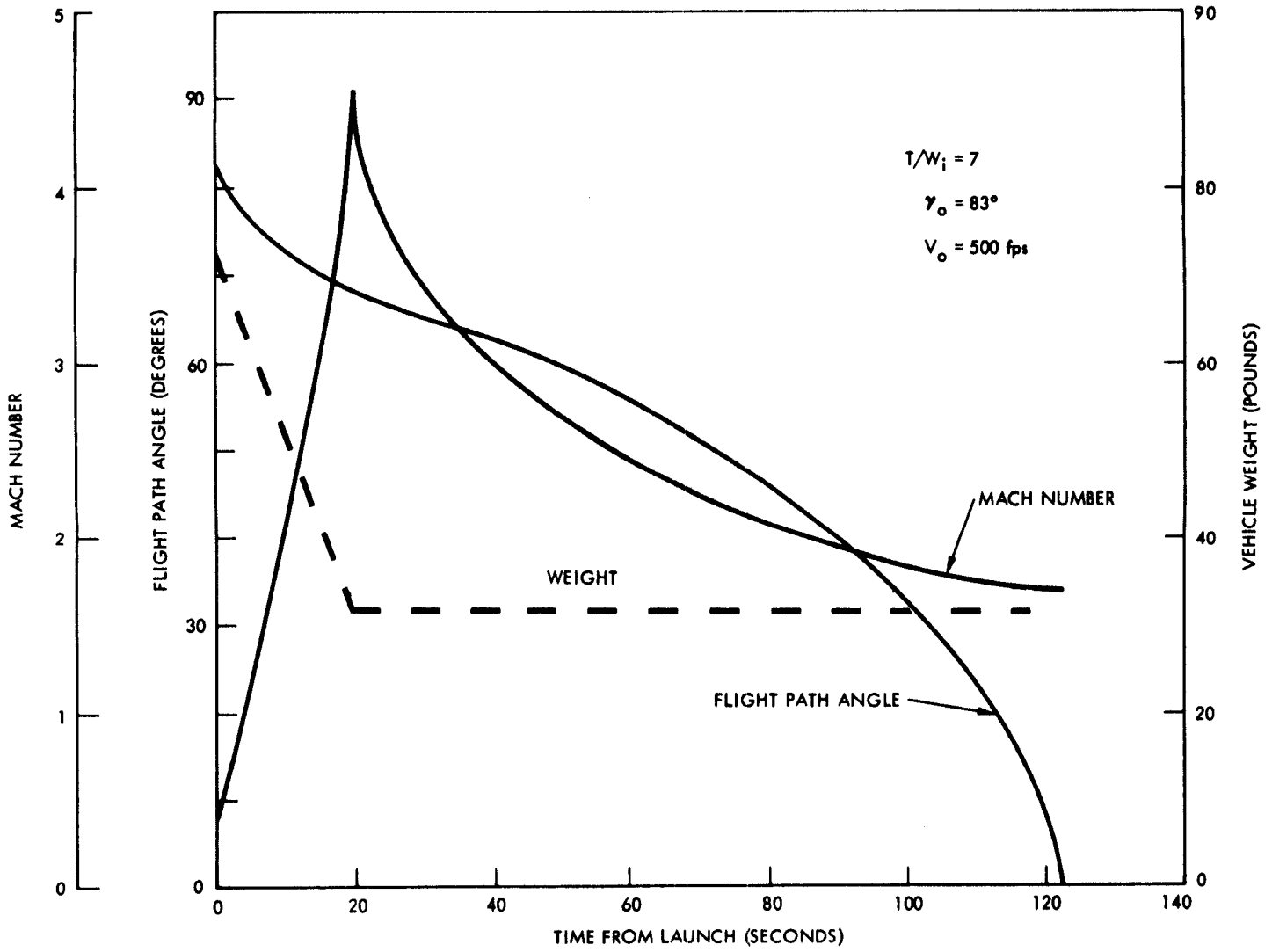

Figure 19. Single-Stage/Apogee Separation Trajectory Characteristics—99 Percent Headwind

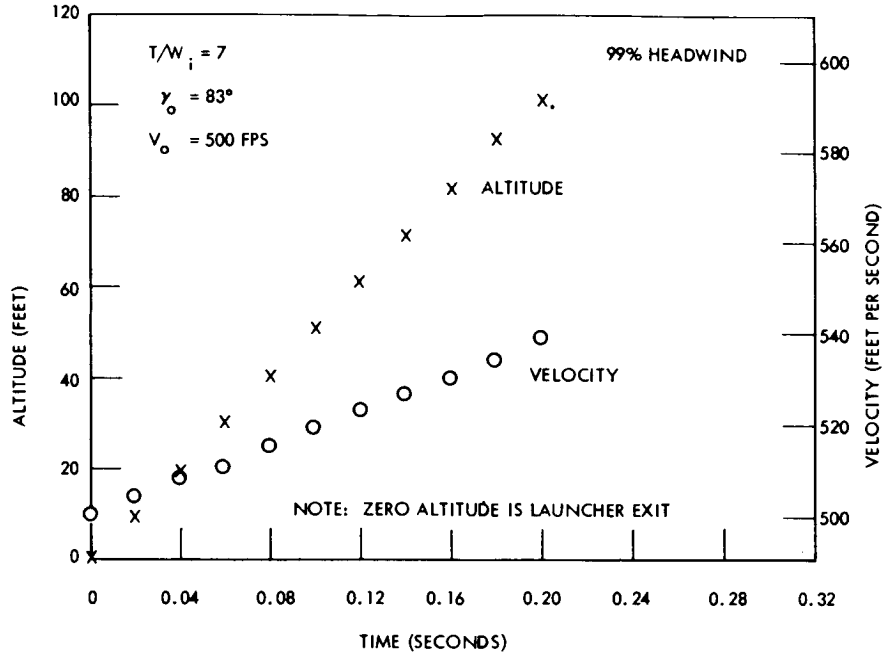

Figure 20. Lift-off Conditions — Single Stage

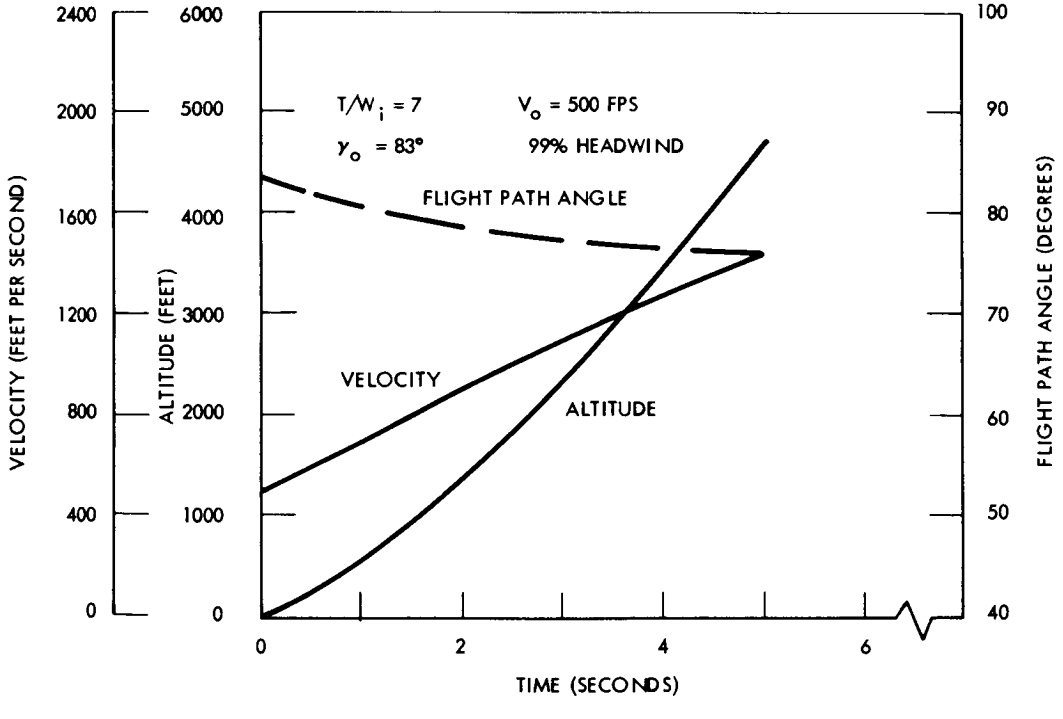

Figure 21. Lower-Altitude Conditions — Single Stage

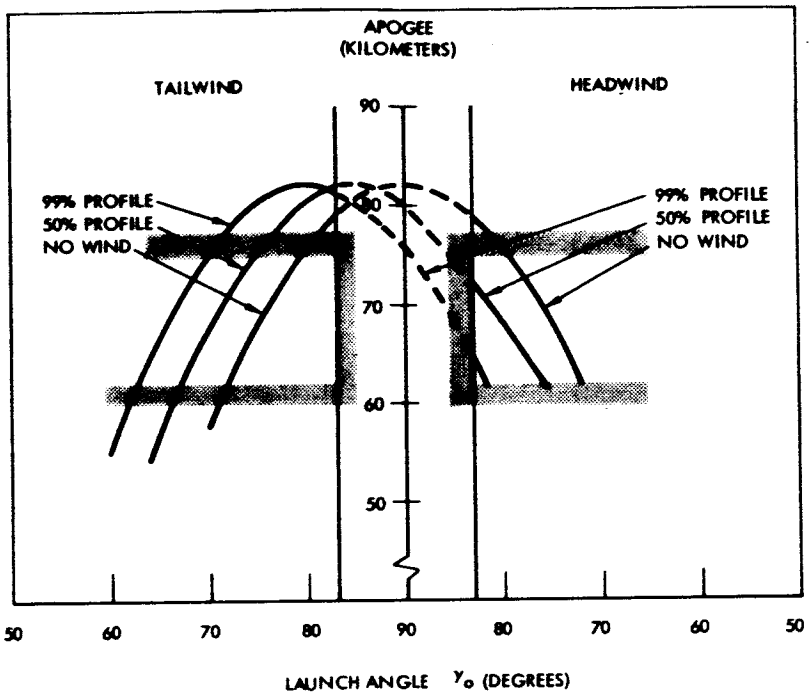

Figure 22. Wind Effect on Apogee—Single-Stage Apogee Separation

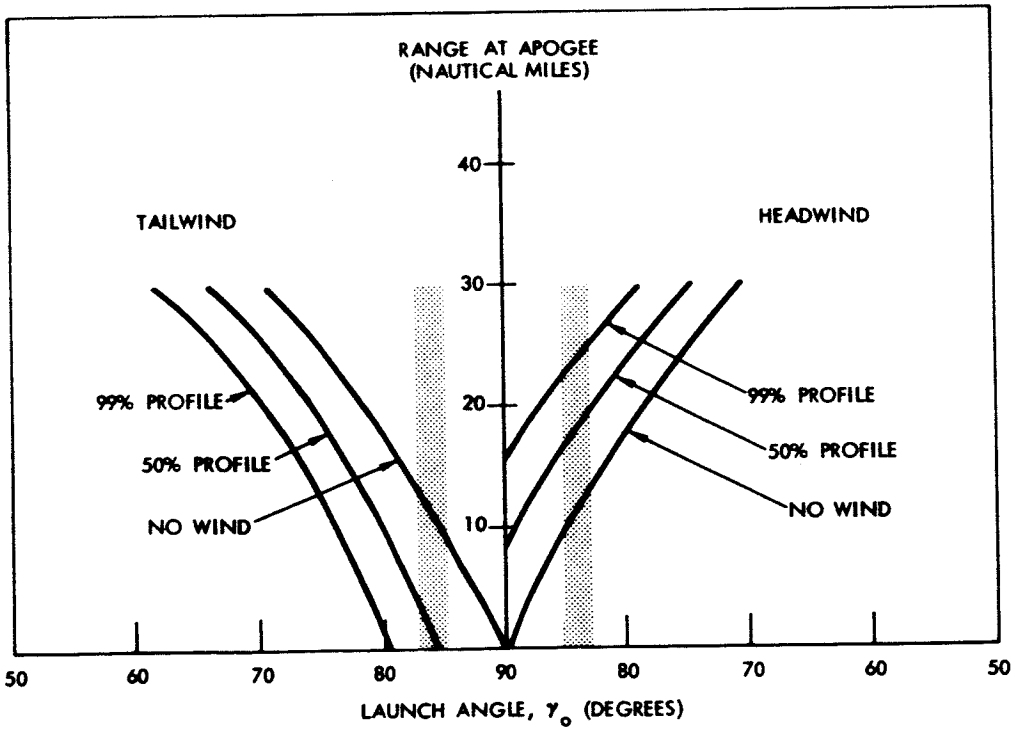

Figure 23. Range at Apogee—Single-Stage Apogee Separation

conditions, provided that initial launch angle adjustments are made. Except for the severe-headwind condition, these adjustments can be fairly gross, as indicated by the approximate 7-degree tolerance in launch angle for a given wind condition.

Since a relatively broad range of launch angles are applicable, a representative angle of 74 degrees is shown for the no-wind case of Figure 17. This launch angle results in close attainment of the target apogee altitude of 65 kilometers.

Limiting conditions in the tailwind environment are due to launch site safety considerations rather than to apogee performance. Compatible situations are evident, however, since the lower launch angles required for a minimum clearance distance from the launch site to apogee still provide for design altitude attainment.

Additional design details and characteristics, component weight breakdowns, and an inboard profile of this vehicle system may be found in the System Design section of this report.

Single Propulsive Stage-Stabilized Payload Separated at Burn-Out

A second approach to the general single propulsive stage system which can be considered is that of separating the motor from the payload just subsequent to burn-out. Examination of the energy requirements (as depicted in Figure 9) immediately indicates, however, that the governing factor in determining the burn-out conditions that must be met is the relationship of W/C_DA of the payload section to W/C_DA of the payload-booster combination.

The design payload chosen for this study dictates the general size, weight, and drag characteristics of the forward section. To provide as minimum a payload drag as possible while maintaining necessary stability characteristics, the configuration shown in Figure 24 was evolved. Estimated drag characteristics for the combination booster-payload and for the payload alone also are presented in Figure 24. Representative trajectory data are shown in Figures 25 through 28. While an approximate 60-percent reduction in drag is realized once the payload is separated, the reduction in mass due to dropping the motor case, aft-fin assembly, and interstage fairing is of the same order (Table 5) and the W/C_DA ratio is approximately 1.0. The net performance characteristics must then approximate those obtained with an equivalent, non-separated single-stage system.

To check this assumption, consider the data shown in Figure 24. For the particular conditions chosen, a slightly better performance is indicated for the near apogee separation case, although very minor adjustments can interchange the relative positions of the two curves. Unless very major reductions in the payload size are made, however, any slight performance benefit from early separation is more than offset by the added system complexity.

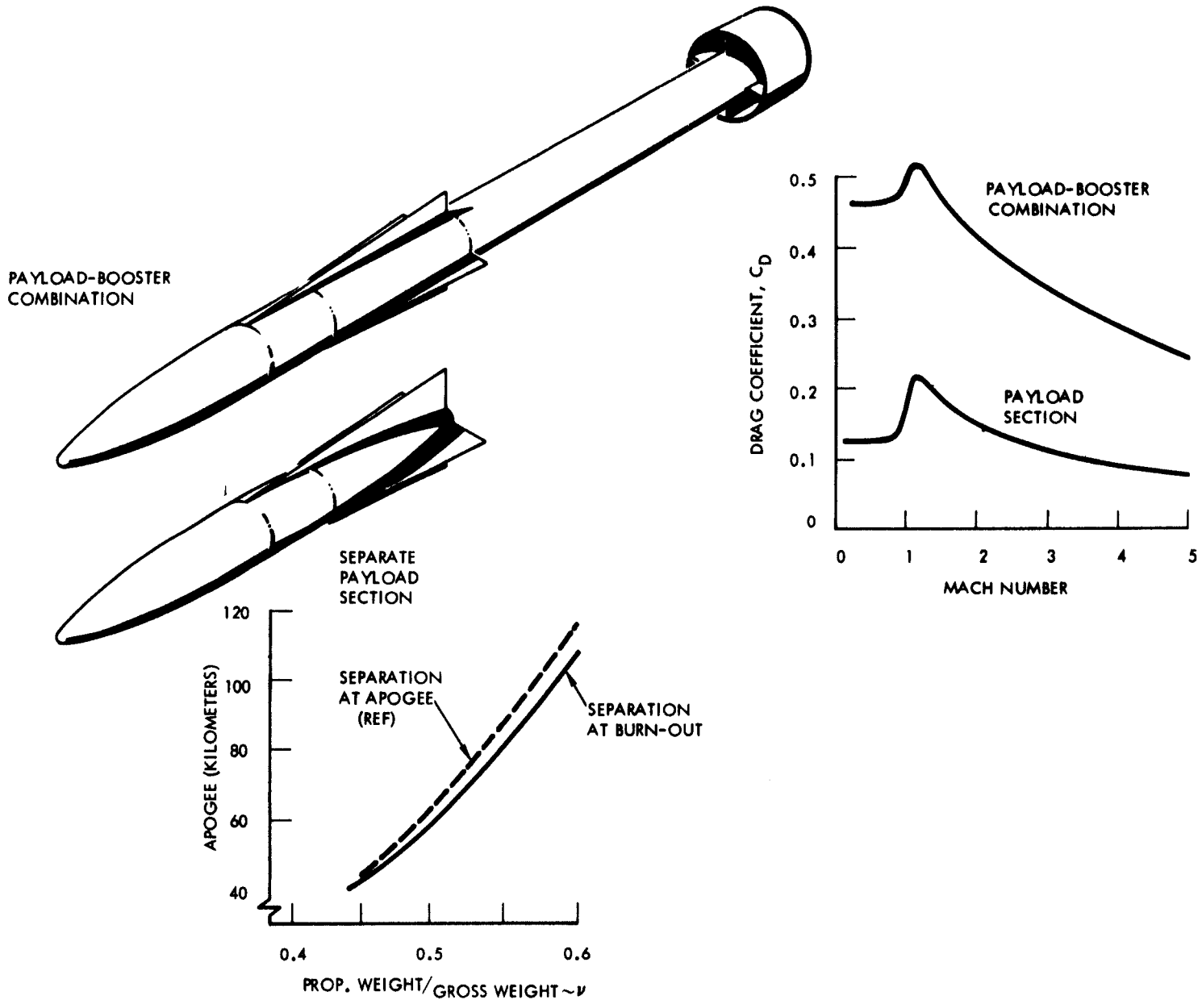

Figure 24. Single Propulsive Stage-Stabilized Payload Separated at Burn-out

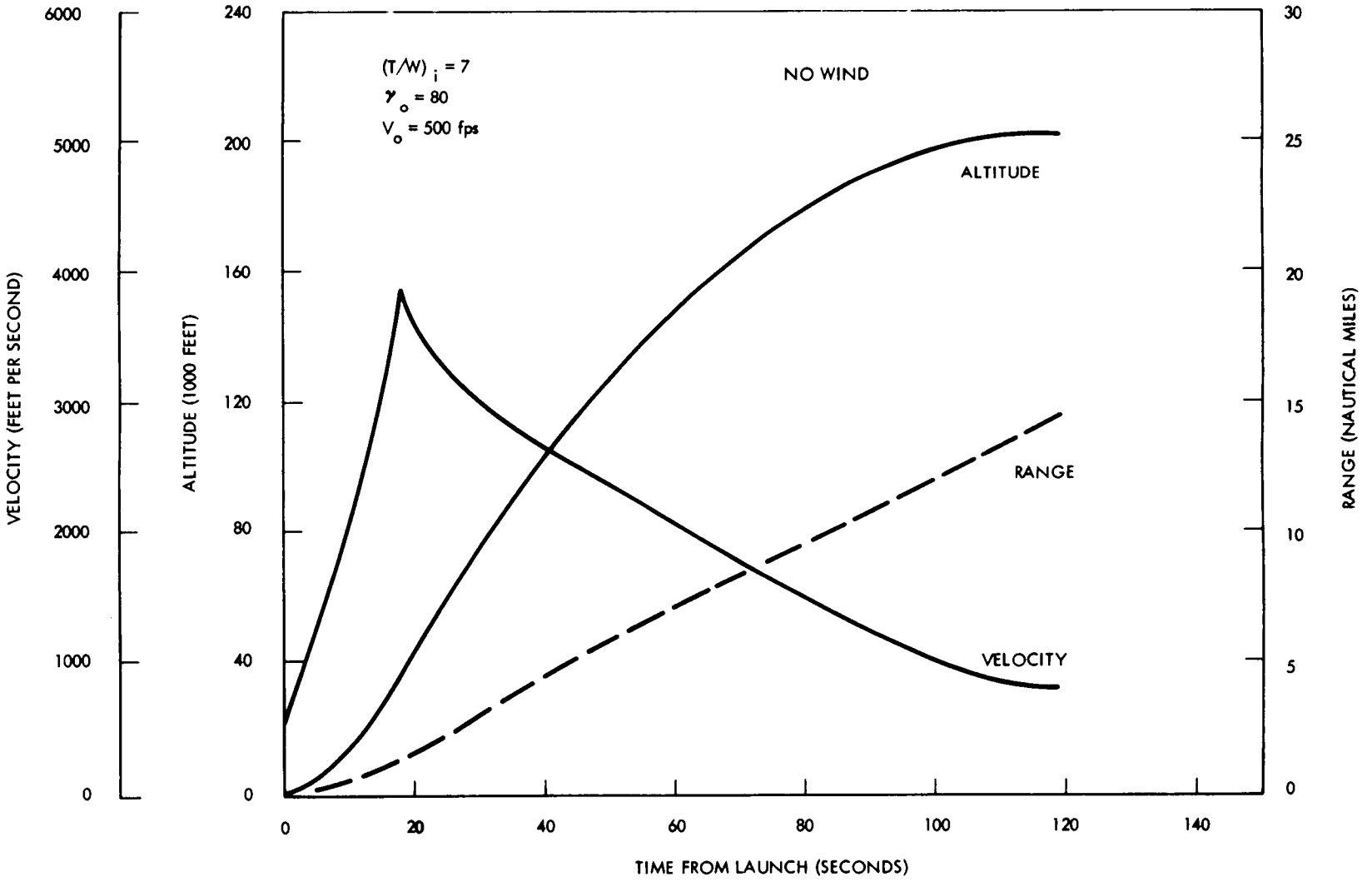

Figure 25. Single Propulsive Stage-Stabilized Payload Separated at Burn-out Trajectory Characteristics

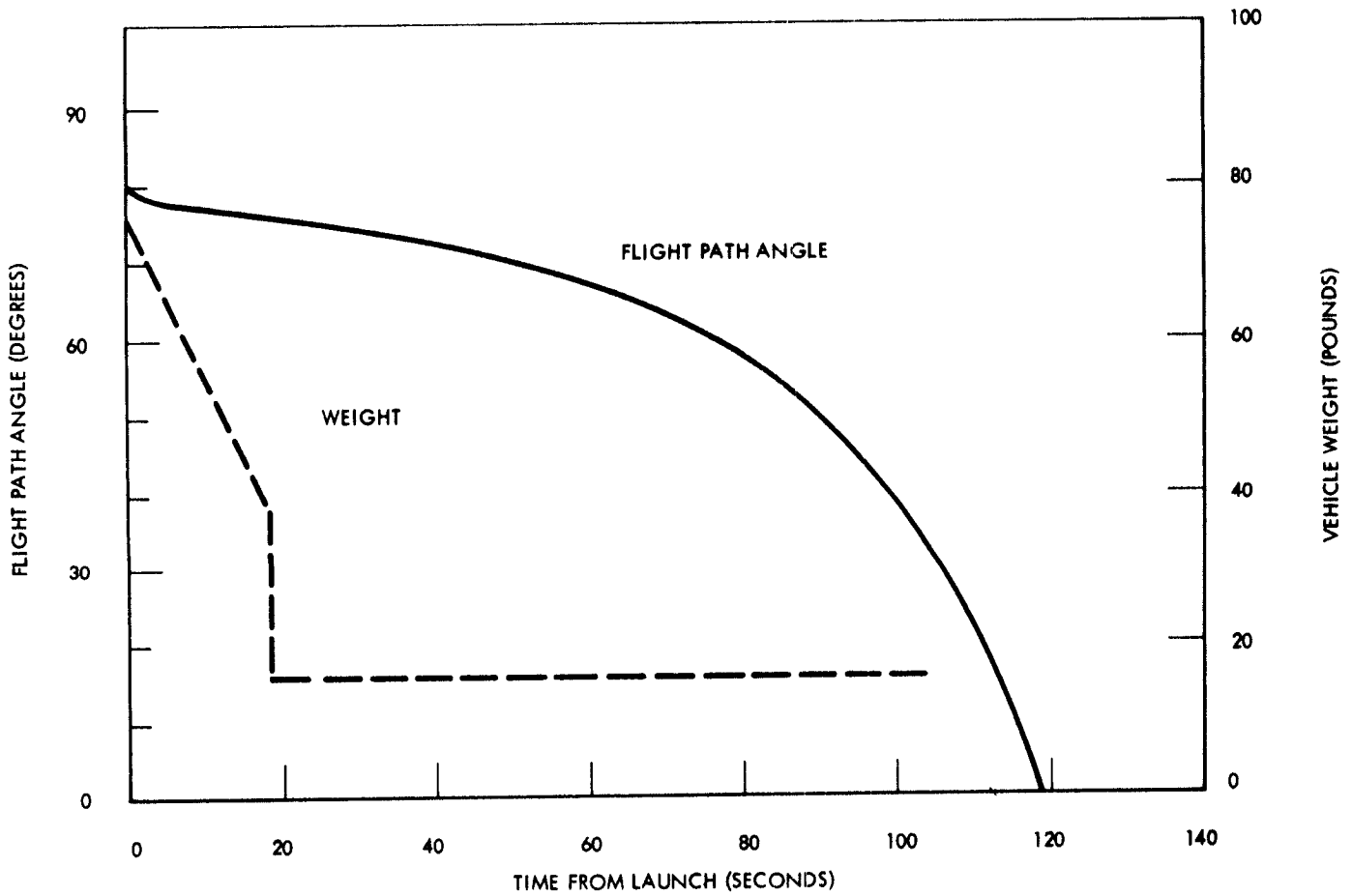

Figure 26. Single Propulsive Stage-Stabilized Payload Separated at Burn-out Trajectory Characteristics

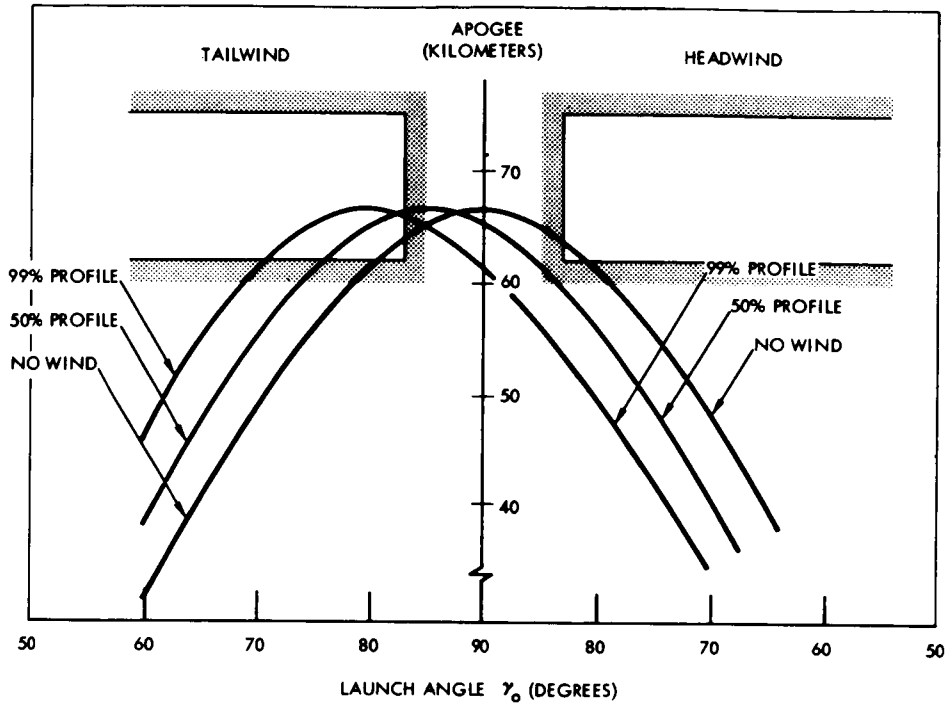

Figure 27. Wind Effect on Apogee—Single Propulsive Stage-Stabilized Payload Separated at Burn-out

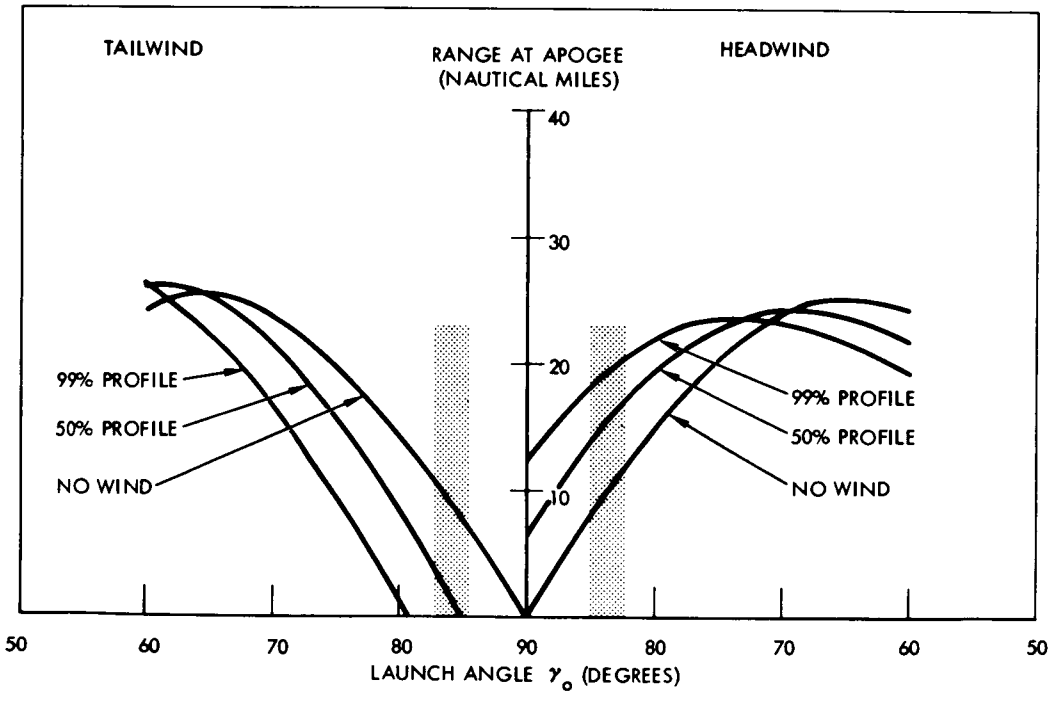

Figure 28. Range at Apogee—Single Propulsive Stage-Stabilized Payload Separated at Burn-out

Table 5. Estimated Weight Breakdown — Single Propulsive Stage-Stabilized Payload Separated at Burn-out

Component	Weight (pounds)
Nose assembly	1.44
Parachute compartment assembly	1.40
Payload fins	1.50
Instrumentation mounting ring and separation system	1.50
Interstage fairings	1.20
Booster attach ring and separation system	1.60
Motor case and insulation	14.50
Tail assembly	3.20
Motor nozzle assembly	1.30
Instrument and parachute assembly	9.90
Propellant	40.60
Total	78.14

Continuous-Burn, Dual-Thrust System

The continuous-burn, dual-thrust system has the potential of furnishing a relatively high thrust level during the initial, lower altitude portion of the trajectory and a sustained thrust for the remainder of powered flight without the complexity associated with separate staging. The single-chamber dual-thrust motor is the least complex of the several conceivable approaches and is, therefore, the method considered for this application.

Figure 29 presents basic performance capabilities of assumed dual-thrust systems under no-wind and 99-percent headwind conditions. As shown in Figure 29, the initially assumed systems fail to attain the apogee conditions desired but do provide useful trend information. Optimum altitude gain occurs, in the headwind case, with a high thrust level portion mass fraction between 0.2 and 0.3 A slight gain also is noted for the 20:3 case over the 10:3. However, continued examination of the characteristics of this type of motor indicated current practical thrust ratios should not exceed approximately 4:1. The single-chamber motor cannot, of course, operate at optimum chamber pressure during both the boost and sustain phases and performance for any one phase limits the maximum practical ratio. The 10:3 was, therefore, re-examined along with changes in vehicle weight, total mass fraction, and launch angle to determine if a satisfactory combination could be attained.

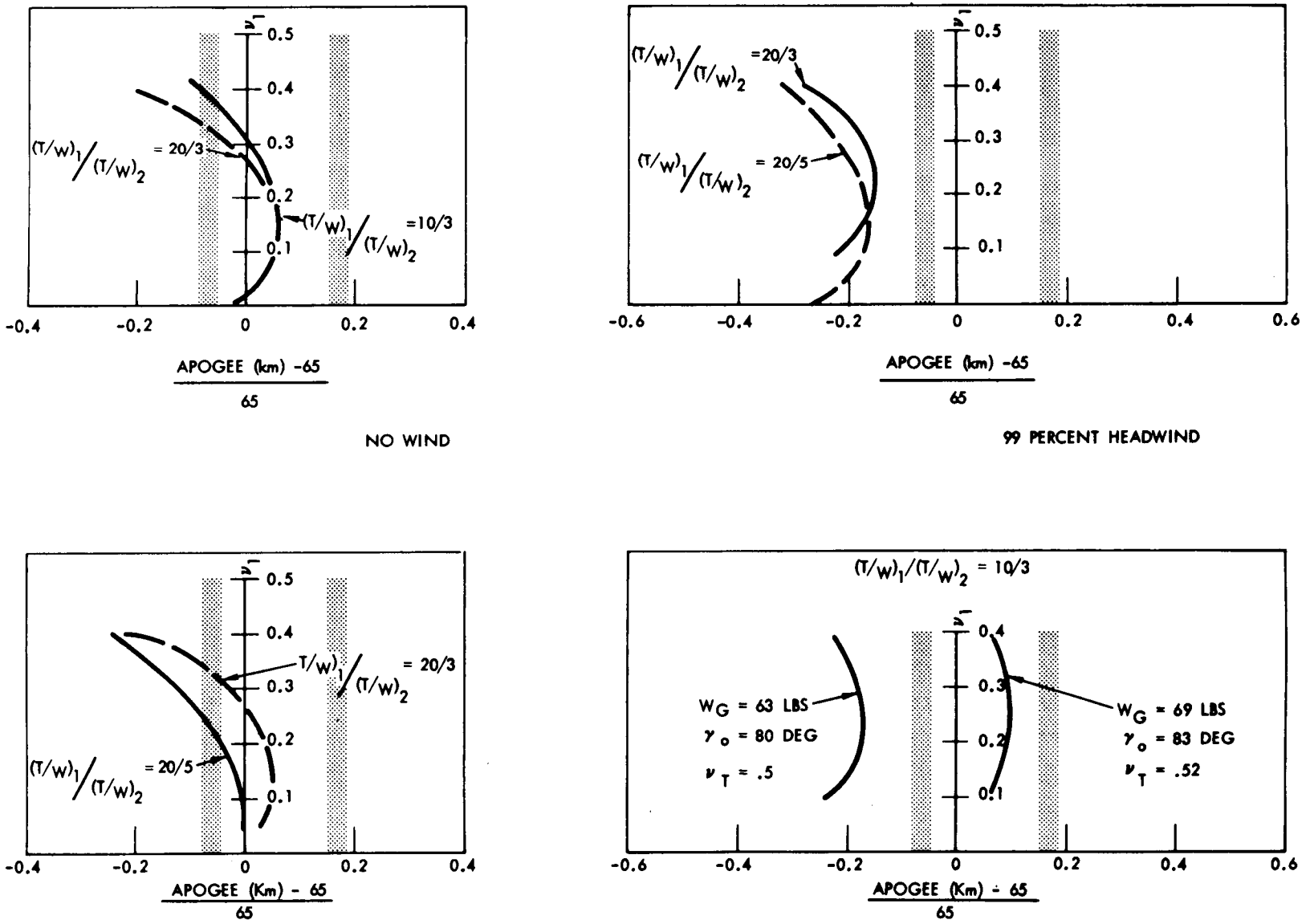

Figure 29. Dual-Thrust Performance Trades

Figure 29 also indicates the apogee attained with the revised configuration and utilization of the maximum allowable launch angle. Satisfactory performance under the severe headwind conditions is exhibited. Pertinent trajectory characteristics of the dual-thrust system are shown in Figures 30, 31, and 32.

Overall apogee capability in the various design wind environments is depicted in Figure 33. The performance trends are comparable to that shown for the single-stage case with a somewhat larger allowable variation in launch angle for the 99-percent headwind case noted. Range at apogee is shown in Figure 34.

General configurational characteristics of the continuous-burn, dual-thrust level motor allow utilization of the approach selected for the single-stage/apogee separation vehicle (see the System Design section). Estimated component weights are presented in Table 6.

Table 6. Estimated Weight Breakdown — Continuous-Burn, Dual-Thrust System

Component	Weight (pounds)
Nose assembly	1.44
Parchute compartment casing	1.20
Instrumentation mounting assembly	1.34
Separation and expulsion system	2.00
Motor case and insulation	15.90
Nozzle assembly	1.30
Fin assembly	2.45
Instrument and parachute assembly	9.90
Propellant	35.70
Total	71.23

Two-Stage System

The two-stage system synthesized for evaluation of performance characteristics is depicted in Figure 35 along with the general drag characteristics associated with the total launch combination and payload plus second-stage assembly.

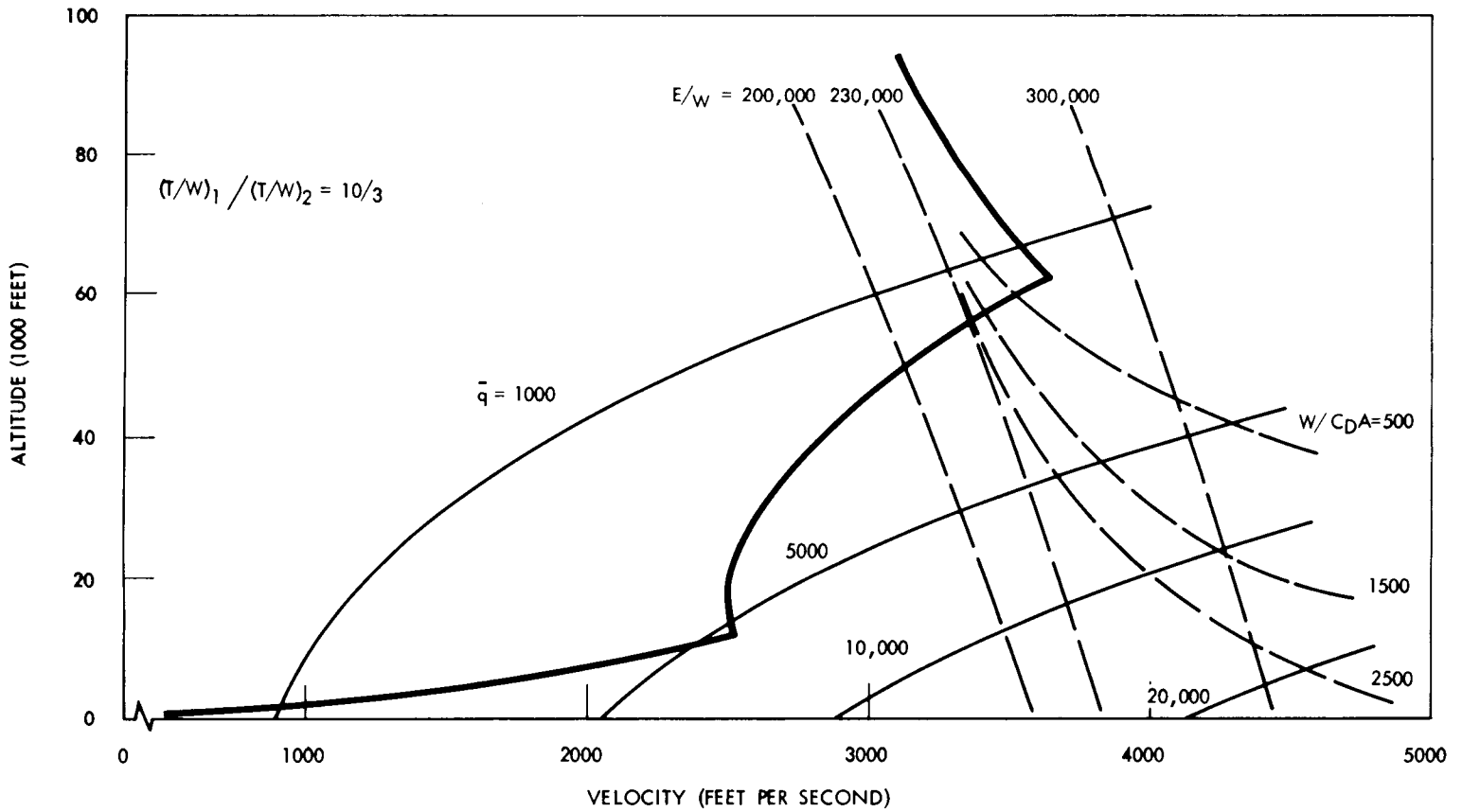

Figure 30. Dual-Thrust Altitude-Velocity Profile

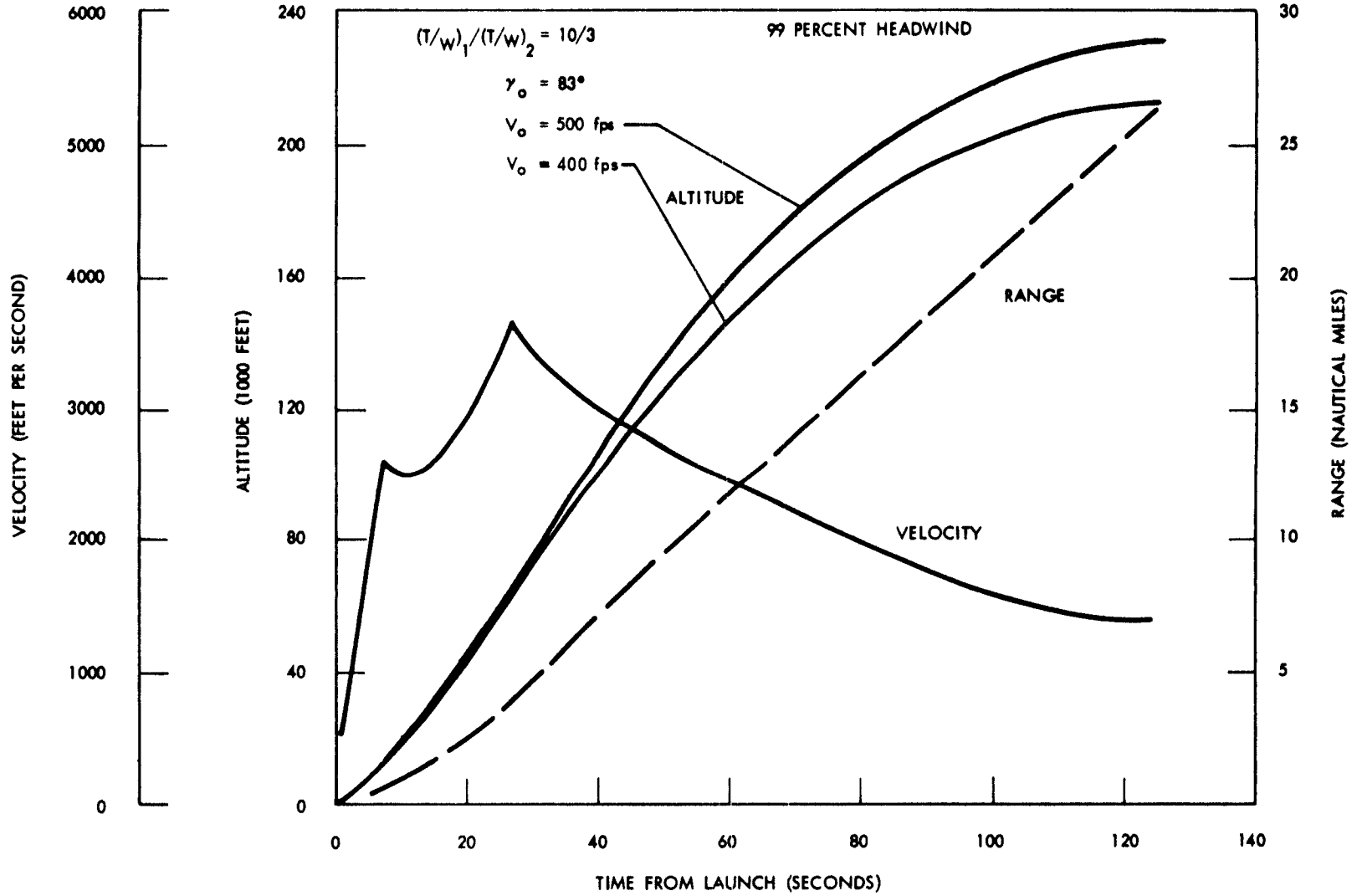

Figure 31. Dual-Thrust Trajectory Characteristics

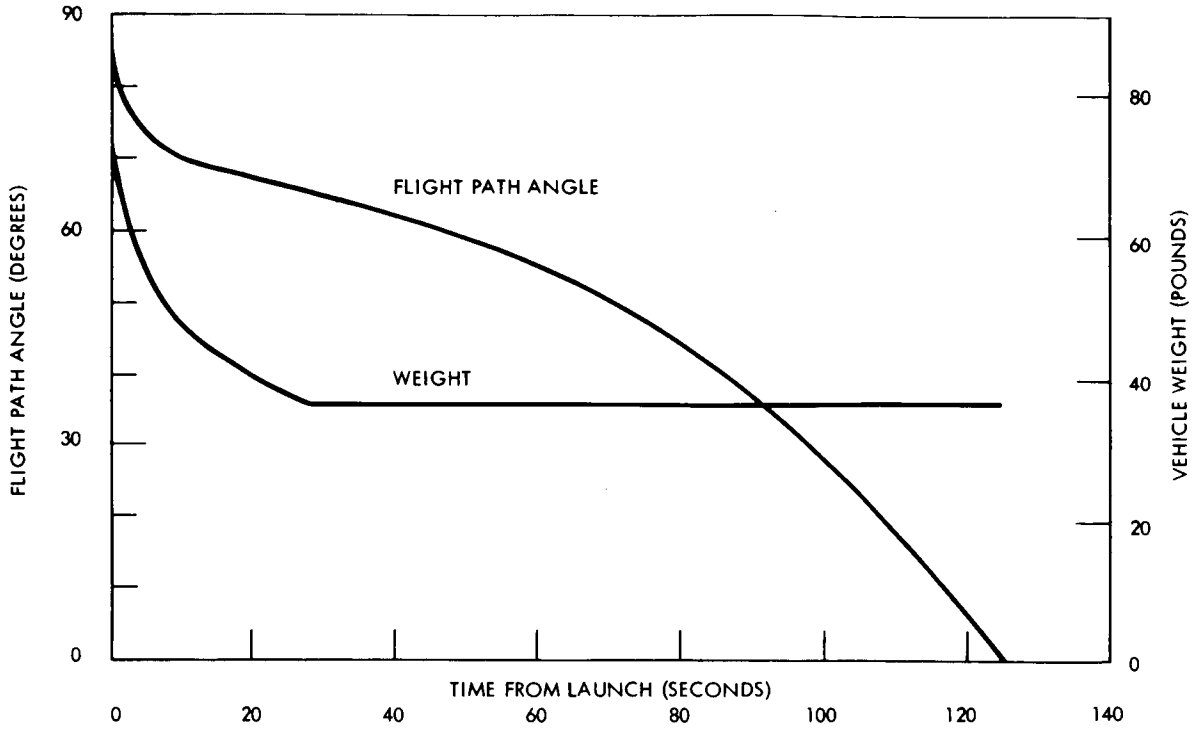

Figure 32. Dual-Thrust Trajectory Characteristics

Figure 35 also depicts the observed trends of initial parametric variations in the stage mass fraction, total mass fraction, and thrust-to-weight ratios. For low initial T/W values, apogee altitude is relatively flat, with variations in first stage to total propellant ratios. As higher initial T/W values are utilized, a marked decline in apogee is shown as the ratio of high-thrust propellant weight to total weight is increased.

The effect of coast time on apogee altitude is indicated in Figure 36. The velocity losses sustained during increasing coast periods must be made up by the second powered portion of the ascent trajectory. Thus, no gain is noted in the intermediate coast time region, and overall altitude capability decreases as the time increment exceeds five seconds. This effect is also portrayed in Figure 37 which presents the altitude-velocity profiles attained with a given vehicle configuration and coast times of 0, 5, and 10 seconds. While the particular case portrayed results in apogees somewhat higher than desired, the trends shown are valid for all combinations noted in this study.

While apogee altitude decreases with increasing coast time, it may be noted by referring again to Figure 36 that the velocity at apogee does increase in order to maintain the necessary energy balance.

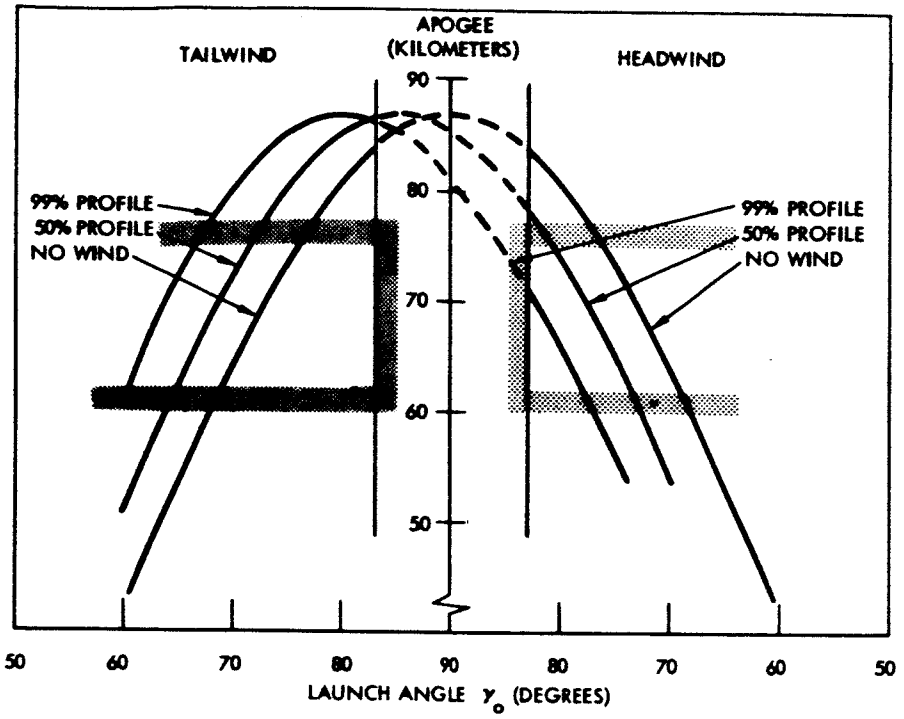

Figure 33. Wind Effect on Apogee — Dual-Thrust Systems

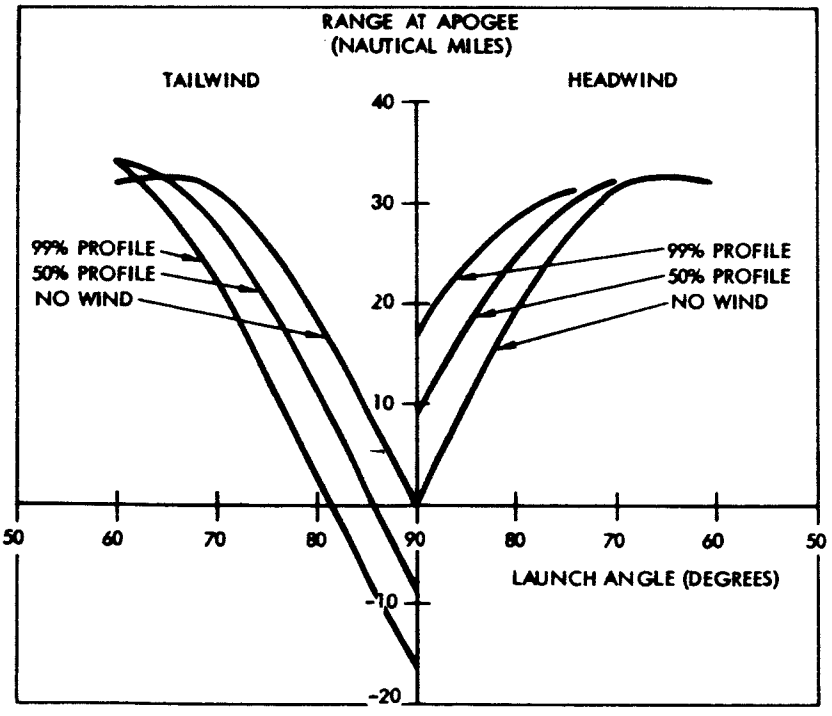

Figure 34. Range at Apogee — Dual-Thrust System

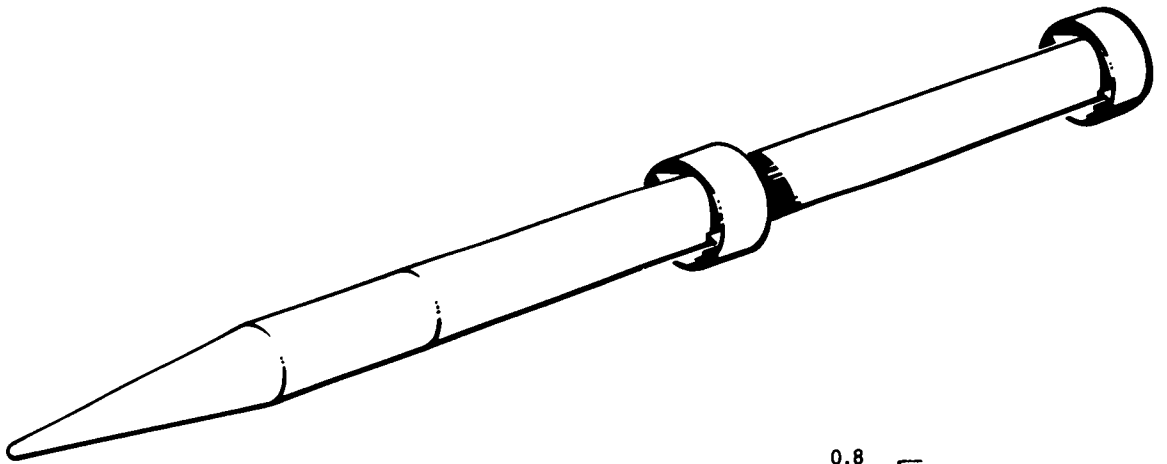

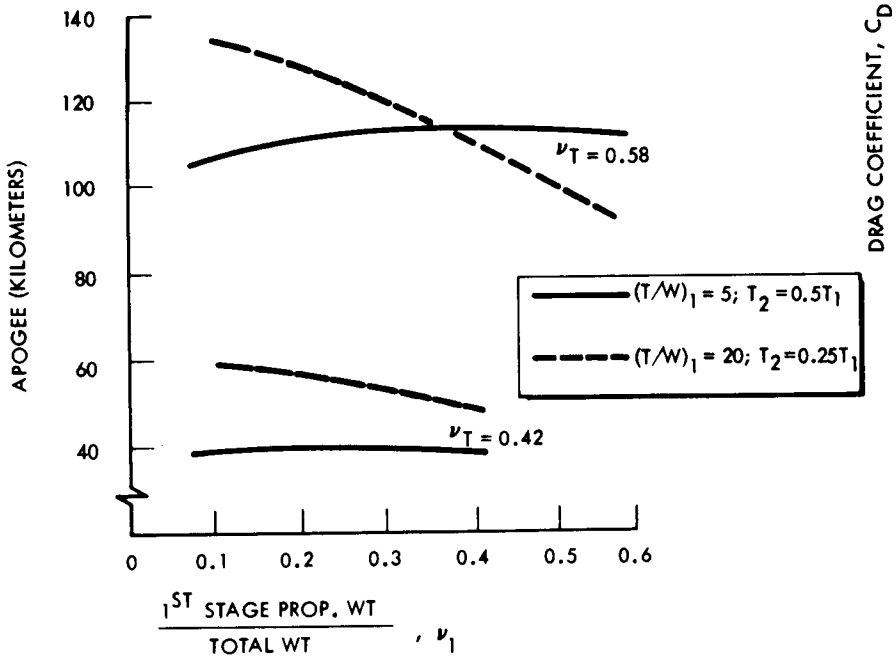

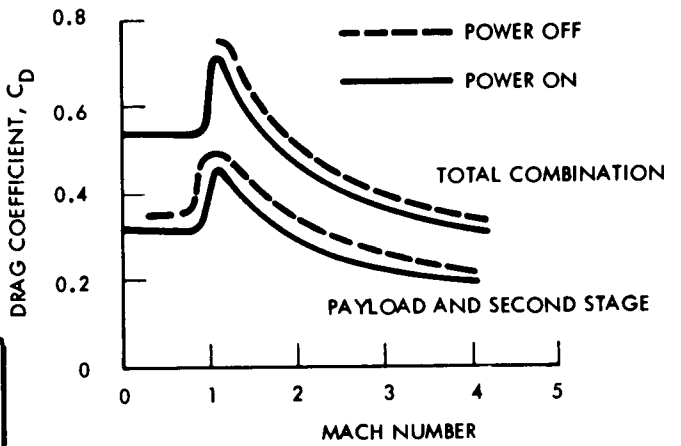

Figure 35. Two-Stage Configuration

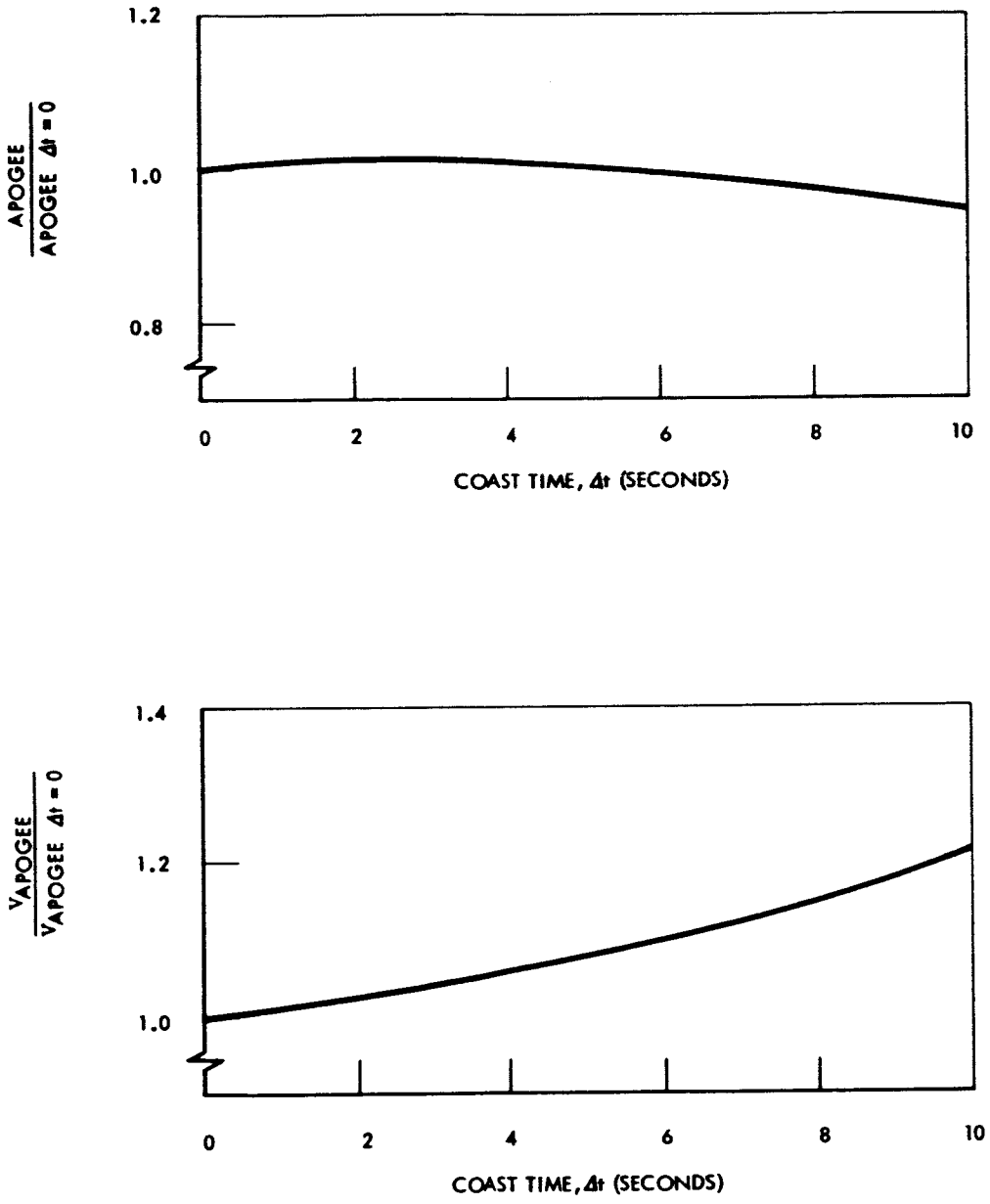

Figure 36. Variation in Apogee Conditions With Coast Time

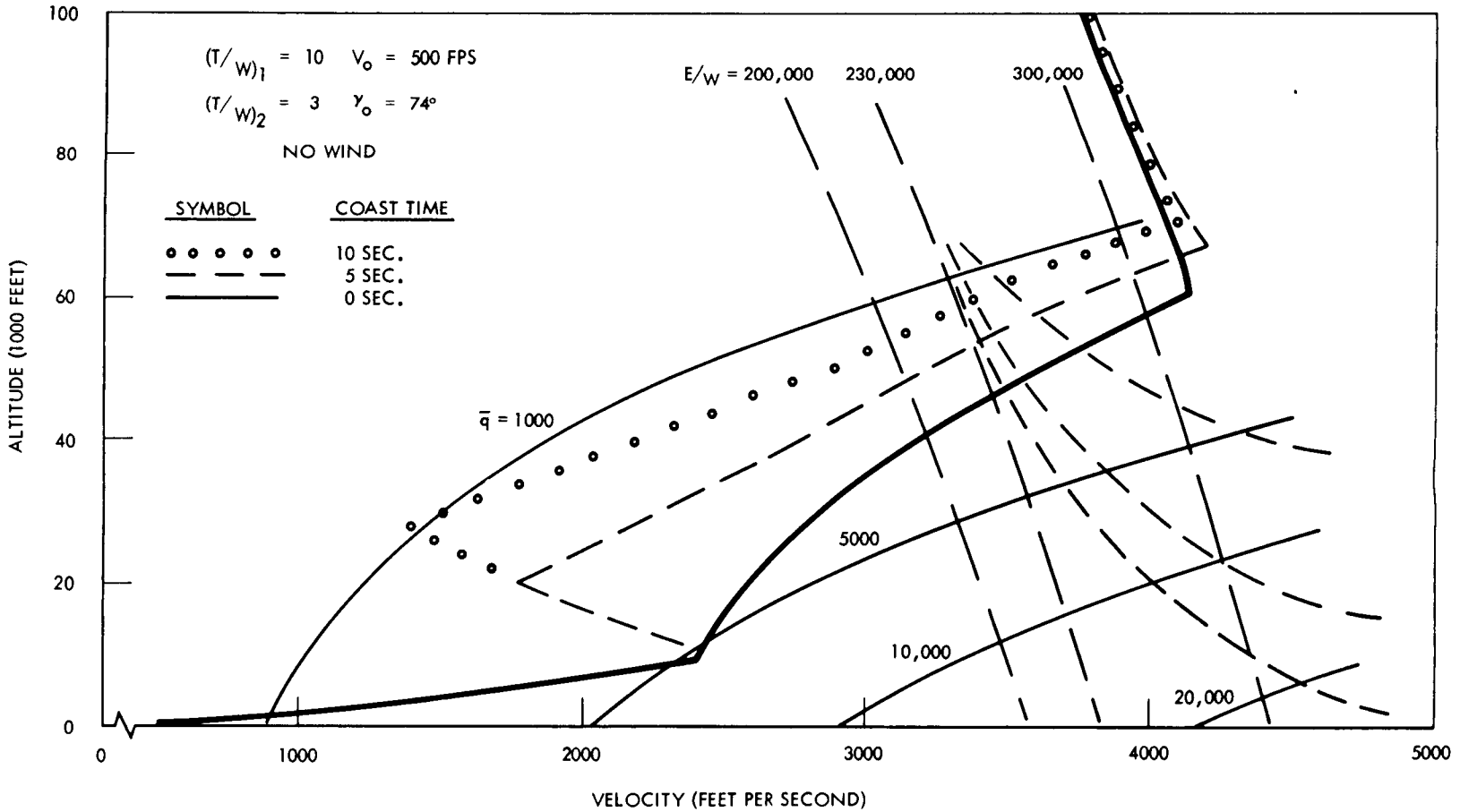

Figure 37. Two-Stage Altitude-Velocity Profiles

While the two-stage vehicle depicted in Figure 37 attains a higher apogee than desired for this study, the trends obtained may provide a useful reference. Figure 38 presents apogee as a function of launch angle and wind environment, while the corresponding ranges are shown in Figure 39. Gross weight of this configuration is 72.8 pounds, with propellant weights of 20.7 pounds and 16.2 pounds for the first and second stages, respectively.

Iterative design procedures were employed to attain a two-stage configuration that more closely approximated the desired performance. The resultant configuration provided trajectory characteristics which are presented in Figures 40 and 41. For the case shown, the coast time was nominally zero. The estimated weight breakdown is shown in Table 7. Apogee and range at apogee are presented in Figures 42 and 43 for varying wind conditions and launch elevation angles.

Table 7. Estimated Weight Breakdown—Final Two-Stage System

Component	Weight (pounds)
Nose assembly	1.44
Parachute compartment casing	1.20
Instrumentation mounting assembly	1.34
Separation and expulsion system	2.00
Second-stage case, insulation, and nozzle	4.50
Second-stage fin assembly	1.70
Interstage fairing and separation system	1.80
First-stage case, insulation, and nozzle	7.60
First-stage fin assembly	4.40
Instrument and parachute assembly	9.40
Second-stage propellant	12.24
First-stage propellant	20.40
Total	68.02

Lateral Wind Effects

In the evaluation of the various systems, direct lateral winds (i.e., at 90 degrees to the direction of launch) were used for comparison purposes. During continued study of the system selected for preliminary design, quartering winds at 45 and 135 degrees to the direction of launch also were used. This aspect is discussed in more detail in the System Design section; at this point, only the comparative performance aspects under an initial direct side-wind will be considered.

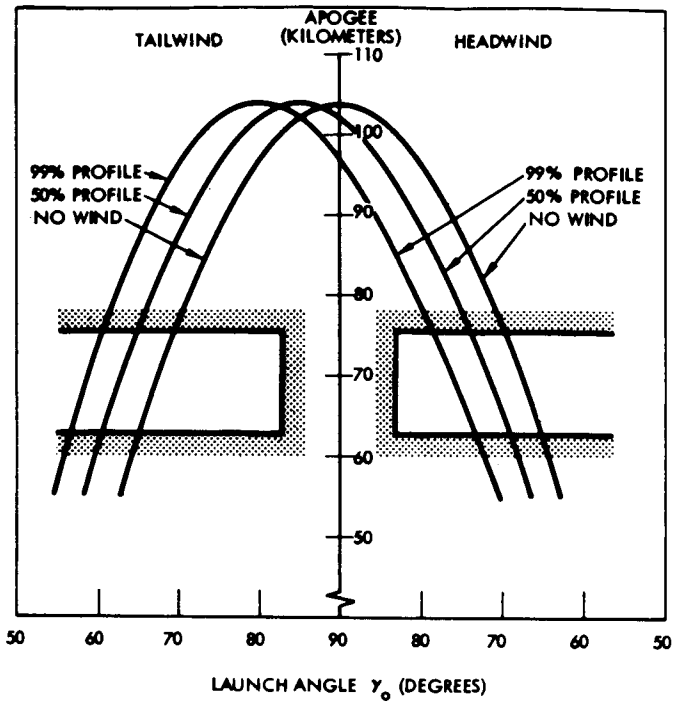

Figure 38. Wind Effect on Apogee—Two-Stage System

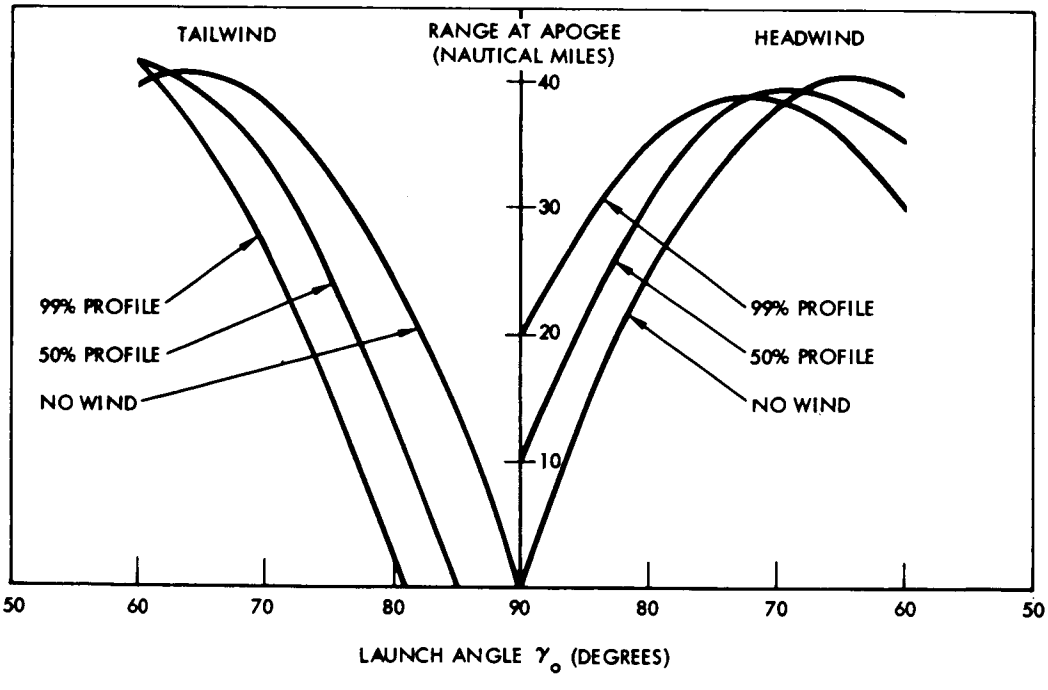

Figure 39. Range at Apogee—Two-Stage System

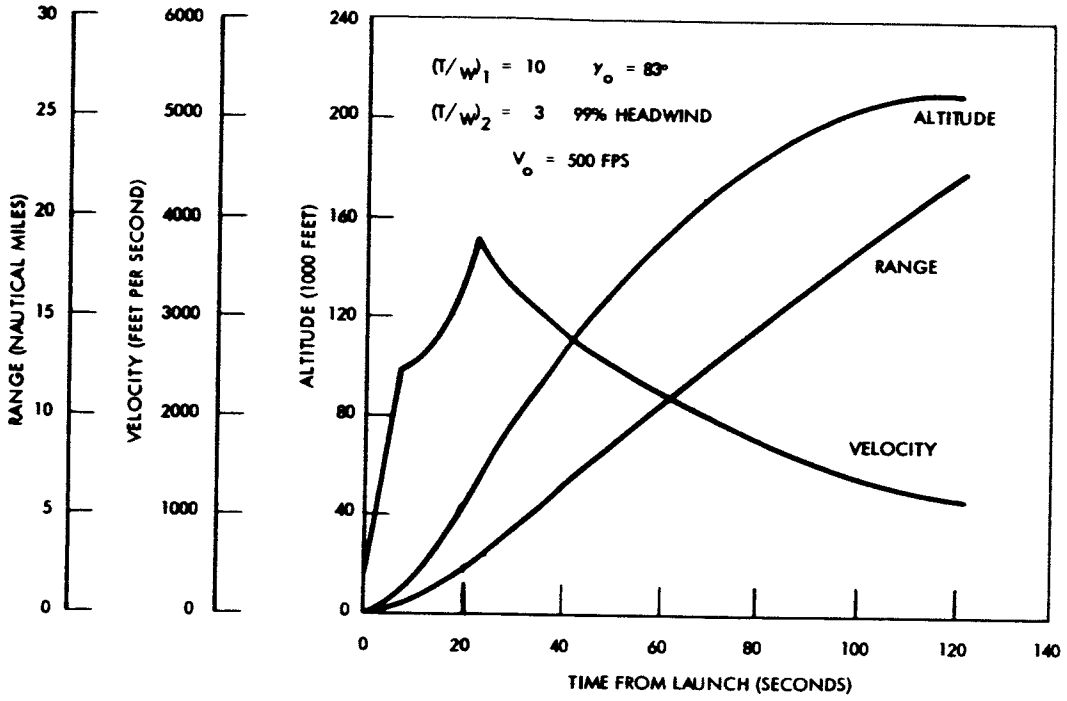

Figure 40. Trajectory Characteristics—Two-Stage System

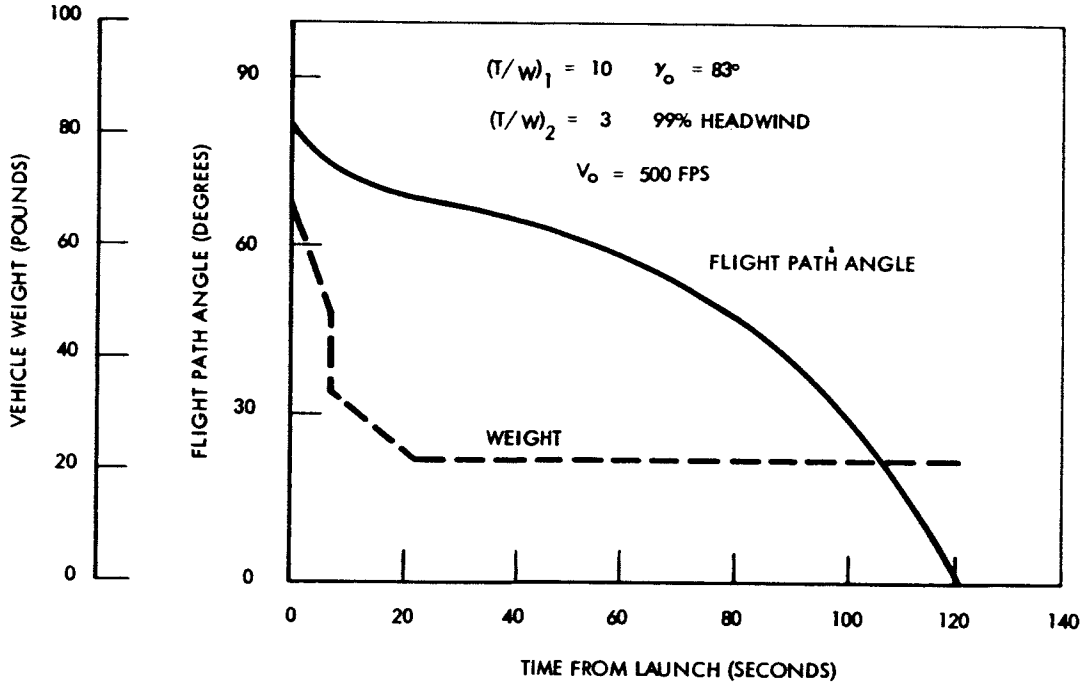

Figure 41. Trajectory Characteristics—Two-Stage System

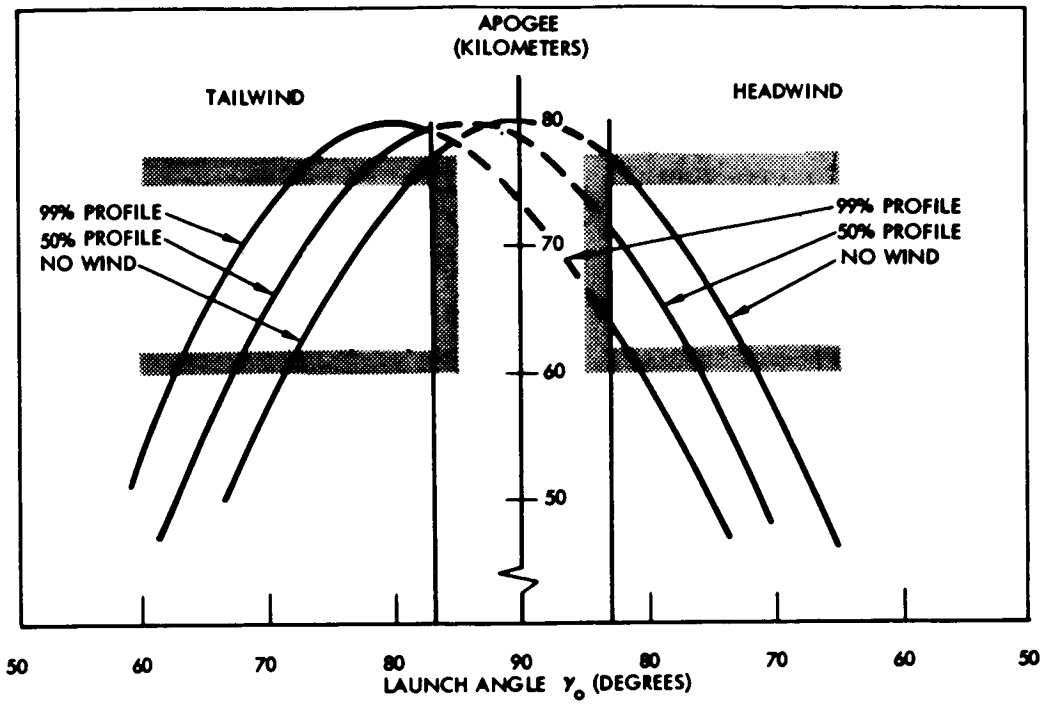

Figure 42. Wind Effect on Apogee—Final Two-Stage System

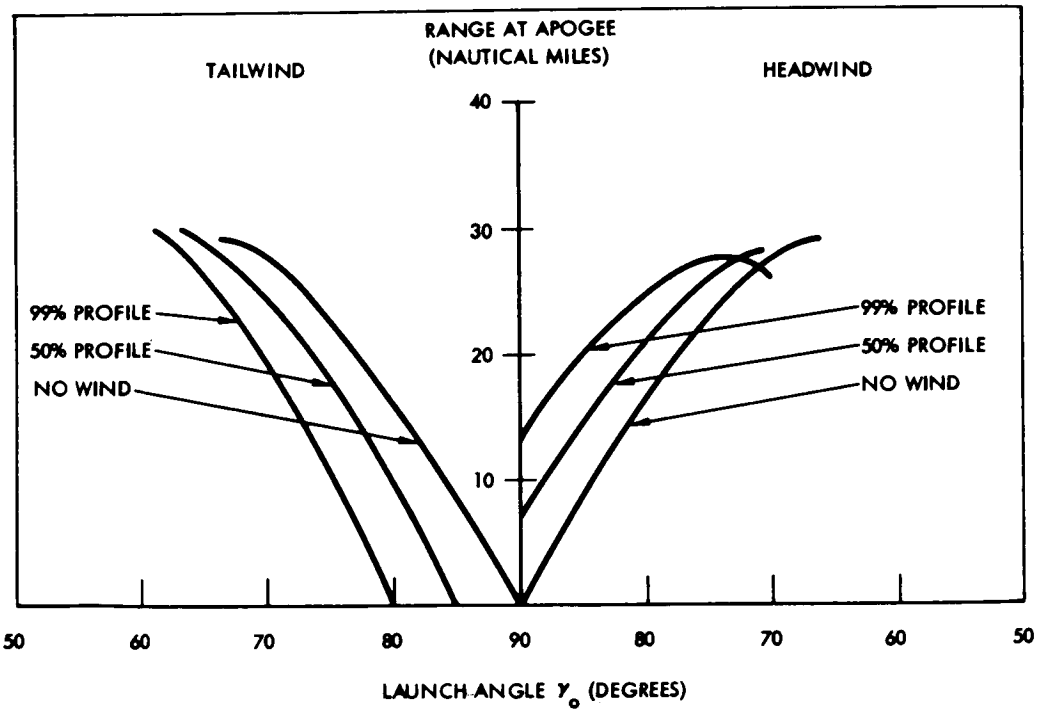

Figure 43. Range at Apogee—Final Two-Stage System

The various configurations were sized to provide, as closely as possible, the same static margin characteristics. Wind-cocking tendencies thus were reasonably similar in the lower altitude region where the majority of transient behavior takes place.

By the time apogee conditions were reached, the flight paths were characterized by an azimuth change of approximately 40 degrees for the 50-percent wind profile and by a change of approximately 52 degrees for the more severe 99-percent wind profile. The azimuth change was, of course, toward the direction from which the wind was assumed to be blowing.

Apogee attainment under the lateral wind condition will be a function of the launch elevation angle as well as azimuth and wind profile. While the complete spectrum of the various launch combinations was not obtained, the limited trajectory data indicate that apogee under lateral wind influence can be expressed as a percentage of the no-wind apogee at a given launch angle. Table 8 indicates the estimated variation for the candidate configurations.

Table 8. Apogee With Direct Lateral Winds

System	Percent of No-Wind Apogee at Similar Launch Elevation Angle	
	50-Percent Profile	99-Percent Profile
Single-stage/apogee separation	94.4	88.1
Single propulsive stage/ stabilized payload separated at burn-out	94.5	88.6
Dual-thrust	95.5	90.7
Two-stage	94.6	89.0

Misalignment Effects

Misalignment effects also may influence the basic performance of the vehicle and prevent the repeatability of trajectories. In coordination with NASA's Langley Research Center, the following tolerance values were established as being reasonably attainable with current manufacturing processes:

Surface alignment:

1. Twist—±0.25 degree
2. Incidence at m.a.c. —±0.05 degree

Body components:

1. In any direction—±0.10 degree

Joints mismatch:

1. Longitudinal—0.100 inch
2. Transverse—0.020 inch
3. Gaps—0.030 inch

Unbalanced masses:

1. C.G. (longitudinal) position—nominal ±1 inch
2. General mass distribution such that cross-products of inertia do not exceed 25 percent of the physically possible maximum

Thrust vector alignment:

1. Mechanical installation—±6 minutes
2. Nozzle flow distortion—±10 minutes

It had been initially expected that application of particular tolerance structures would indicate noticeable variations among the candidate system approaches. This was generally not the case and all systems exhibited similar trends. The few exceptions are noted in the following discussion.

Angular mismatch and thrust vector alignment tolerances of body components produce moments that must be trimmed by a steady-state angle of attack. (The term steady-state is somewhat misleading because variations in vehicle dynamics and environment are occurring all along the trajectory. The term is used here to define a non-spinning case, result.) In the case of thrust misalignments, the relatively small values, coupled with smoothing of dispersions due to spinning the vehicles, were generally trimmed with average angles of attack of less than 0.4 degree. There were two exceptions to this. The second-stage burn-out region of the two-stage system and the final burn period of the dual-thrust system occur at higher altitudes and lower dynamic pressures; consequently, somewhat larger trim angles are needed to generate sufficient aerodynamic restoring torques. In the two cases noted, the angle of attack approached one degree as burn-out conditions were reached.

Body component alignments produced the same trend. In this case, angles of attack of approximately 0.3 degrees resulted and were amplifed accordingly during spin-pitch resonance periods. Nominal spin rates resulted in passage through resonance conditions early in flight; amplification factors under these conditions fell within a maximum band of 4 to 6. Thus, for cumulative worst case conditions of thrust plus body component misalignments, the short-term angles of attack approached 4.5 degrees. On a more probable, root-sum-square basis, a combined maximum of 3.0 degrees would be expected during resonance.

The tolerances which have a primary effect on spin rate are the ones that appear most critical. In addition to the possible variations caused by surface misalignments, which produce spin rate variations of up to 5 revolutions per second, the general mass distribution tolerance has noticeable effects.

Examination of the cross products of inertia that could result under the allowable tolerance conditions indicated that values on the order of 30 percent of the product of nominal pitch-roll moments of inertia were reasonable. Inclusion of the resultant cross-product terms in vehicle trajectory simulations resulted in reducing the nominal (zero cross product) spin rates by as much as 40 percent. While the slow spin rates were adequate to smooth out dispersion tendencies, the problem that is created is associated with the resonance phenomenon. At slower rates, the resonance point is attained at a higher altitude (specific examples are discussed in the System Design section) and amplification factors may reach values in excess of 16. In the absence of other disturbing forces, this is not bad. When coupled with other misalignments (for example, the previously discussed two-stage or dual-thrust system thrust misalignments resulted in a steady-state angle of attack approaching one degree) dynamic excursions may exceed reasonable limits. Even when the phenomenon occurs within a velocity-altitude environment where loads are not a problem, the large angles may force the vehicle into regions of nonlinear aerodynamic behavior.

Admittedly, a worst-case combination has been viewed here, but it is an area that needs to be spotlighted because of the potential severity of results. At lease two solutions are apparent. The first would be a general tightening of the tolerances associated with surface alignment. The ring-fin assembly concept appears amenable to normal production practices that would allow tighter tolerance control without excess cost. For a cast and machined assembly approach, tolerances on the order of 0.1 degree appear very reasonable. This would reduce the spin rate variation to about 2 revolutions per second. Tightening of the mass distribution tolerance also appears possible but bears more investigation. Spin balancing techniques could be utilized to control this deviation band.

Another approach is the use of pre-spin (or exhaust forced spin) to keep vehicle spin rates above values which result in spin-pitch resonance. This method is discussed further in the System Design section.

From other than a resonance coupling standpoint, spin rates of as low as one revolution per second were sufficient to alleviate dispersions due to the misalignments so far discussed and no significant influences on overall trajectory were noted.

Variation of longitudinal center of gravity within the allowable band also showed little effect. All configurations were purposely sized to provide a nominal 3- to 4-inch minimum margin. During the early portion of flight, where the majority of pitch response occurs, the allowable shift represented, in general, less than a 5-percent variation in static margin. This is within the tolerance band of estimated aerodynamic derivatives. At burn-out conditions, where a 1-inch shift represents 25 to 30 percent of the static margin, higher amplitude transient response is, of course, noted for the reduced margin case. Unless unusual forcing functions were also present, however, long-term flight path variations were within a degree of nominal. This would not be true if an unstable configuration resulted but adequate margins were maintained.

Joint mismatches and body or surface misalignments also may contribute to an increase in the nominal drag of the vehicle. For the relatively simpler shapes such as the single-stage, apogee separation, and dual-thrust configurations, incremental drag variations due to these effects are estimated to fall within a band characterized by 2 percent of the nominal drag values. For the slightly more complex burn-out separation and two-stage systems, 3 percent of nominal appears reasonable.

These values are within the overall accuracy band of any total vehicle estimated drag; however, Table 9 gives an indication of the reduction in apogee over that attained with an assumed nominal drag and provides an indication of the expected performance degradation.

Table 9. Apogee Variance With Increased Drag

Additional Drag Increment (percent of nominal)	Apogee Attained (percent of nominal)
5	95
10	91
20	82

A word of caution must be introduced concerning the application of the tolerance criteria. Before final conclusions can be reached on overall acceptability of the assumed tolerance structure, a closer investigation of so-called secondary effects appears mandatory. For instance, it is conceivable that a joint mismatch may — depending on its location — disrupt normal flow over the body and introduce aerodynamic nonlinearities that could substantially change the response picture. Particular flow patterns and other dynamic transients occurring during stage separation also may introduce periods of nonlinear behavior. Analog simulation techniques, preferably augmented with wind-tunnel test data, appear to be the best analysis tool to apply to investigations of these specific regimes of the total trajectory.

Performance Comparison Summary

A re-tabulation of parameters that characterize the performance of a given vehicle appears useful and is presented in Table 10.

Table 10. Performance Recapitulation

System	Gross Weight (pounds)	Total Mass Fraction, ν_T	Apogee Under 99% Wind & $\gamma_o = 83°$ (kilometers)	Allowable $\Delta\gamma_o$ (99-percent wind, h = 62 kilometers)
Single-stage/apogee separation	71.4	0.51	65.0	-1.2
Single propulsive stage-stabilized paylod separated at burn-out	78.1	0.52	54.5	—
Dual-thrust	71.2	0.50	71.3	-4.5
Two-stage	68.2	0.48	64.2	-1.3

With the exception of the nonpropulsive second-stage system, all candidates are capable of attaining the desired apogee band under the wind conditions and launch elevation constraints delineated for this study. Minor variations in mass fraction or possible drag refinements also could put it into the proper band.

The systems are extremely sensitive to weight and mass fraction variations and a matter of two or three pounds difference will have considerable impact on results. A consistent estimate of component weights for the various systems was used throughout the study and while the magnitude of any individual item may vary in a detailed design, the relative positions appear valid.

Relative ranking of the systems, from the single viewpoint of performance, appears to be best accomplished by considering the payload-to-gross weight requirements plus the allowable tolerance on launch angle requirements under the severe wind profile. (This latter criteron may be noted in the last column of Table 10 where $\Delta \gamma_o$ indicates the amount less than the maximum 83-degree value that can be tolerated for attainment of the lower altitude boundary.)

On this basis, and assuming equal value for each item, the relative performance standings are:

1. Dual-thrust and two-stage

2. Single-stage/apogee separation

3. Nonpropulsive, stabilized payload separated at burn-out

Specifics associated with the growth potential capabilities resulting from use of high-energy fuels, alternate propellant methods, etc., are discussed in Volume II of this final report. In general, any of the systems considered appear amenable to attainment of the desired higher apogee capabilities.

SYSTEM RELIABILITY COMPARISONS

A representative sequence of events associated with the meteorological sounding rocket mission is shown in Figure 44, which traces the history of a rocket vehicle from storage, through checkout and launch, to acquisition and transmission of atmospheric data. The net mission effectiveness will be influenced by the degree of reliable accomplishment attainable for each step in the sequence; however, the events of prime interest to this study are those associated with the vehicle launch and flight. These may be separated into two categories for purposes of comparative evaluation of the candidate systems:

1. Events associated with attainment of the design apogee altitude

2. Events associated with the deployment and operation of the payload once apogee has been reached

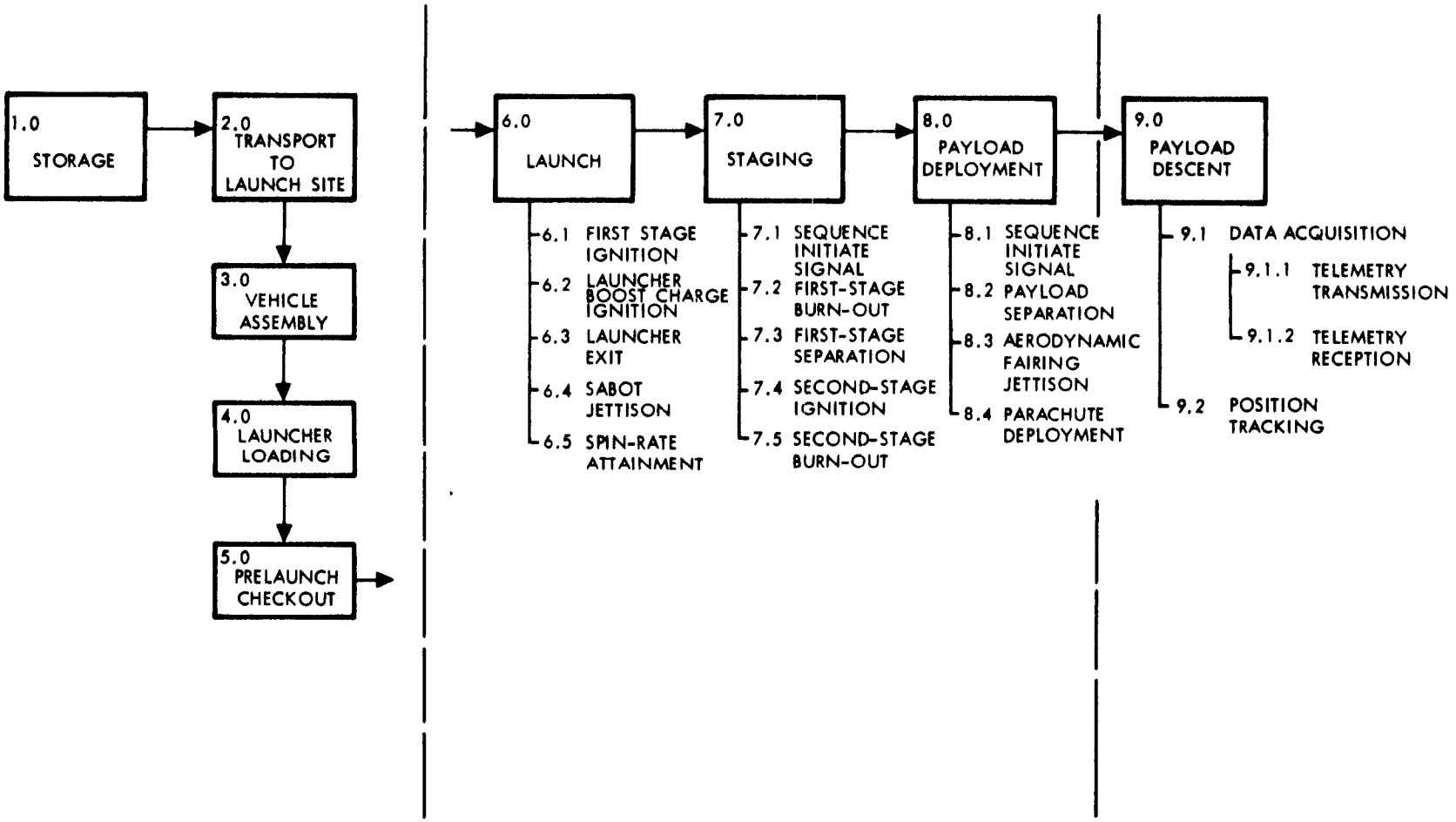

Figure 44. Generalized Sequence of Events

Study requirements established a goal of 95 percent for the successful attainment of design altitude. This overall objective must, in turn, be apportioned among the pertinent components and functions of the launcher, rocket motor, separation systems (for particular candidate system approaches), and vehicle structure.

The apportionment associated with the second category includes functions and components relevant to the payload expulsion system, parachute deployment, payload sensors, and radiosonde system operation.

Critical Area Review

A review of available failure data associated with this general class of vehicle was undertaken in order to provide reasonable assessment of the operational reliabilities of the various functions. The major potential reliability problem areas highlighted by this review are listed in Table 11.

Quantitative field failure data availability was limited, but it is of interest to note that one set of data (Reference 2), although limited in detail and obtained under fairly severe environmental conditions, indicated that 72 percent of the failures occurred in the payload-parachute function category. Information on more recent single-stage vehicle firings indicates a marked improvement in the attained success ratio, with the gains attributed to improved propellant manufacturing controls, progressive modifications to the radiosonde, utilization of a progressive burning charge in the payload expulsion system, and continuing modification of vehicle stability characteristics as a result of field use.

System Comparisons

The reliability apportionments for the four candidate systems of this study are shown in Tables 12 and 13. The parachute-payload functions are considered identical for the single-stage/apogee separation, dual-thrust, and two-stage approaches since a singular payload model was used and similar methods of deployment appear possible. A slight reduction in the apportioned parachute-payload function may be noted for the single propulsive stage-stabilized payload separated at burn-out due to the somewhat more sophisticated design requirements.

The ascent reliability of the dual-thrust configuration could approach that attained by the single-stage/apogee separation case. If the launcher booster charge could be eliminated by compensating with a sufficiently higher initial thrust level, the dual-thrust ascent reliability would increase from 0.946 to 0.947. Further increase in the dual-thrust configuration would be available if the motor burn apportionment could be assumed equal to that of a conventional end-burning motor. Neither of these assumptions appears

Table 11. Potential Reliability Problem Areas

Components	Failure Type
ATTAINMENT OF ALTITUDE	
Rocket motor case assembly	Motor case rupture caused by end-burning grain exhaust gases igniting grain along the side or forward end producing excessive burning area and internal pressure.
Nozzle assembly	Misdirected thrust from misaligned nozzle; burn-through or excessive throat erosion from inadequate design; poorly applied insulation, poor materials and fabrication.
Liner bonding, and internal case insulation	See rocket motor case assembly above. Mechanical bond failure arising from excessive temperature of case can cause failure to attain altitude or loss of vehicle and use of instrumentation. Other possible types of failure include excessive thermal heating leading to case bending, bulging, distortion, and burn-through.
Propellant	Deterioration or mechanical damage during storage or handling can cause excessive increase in burning areas and internal pressures that can rupture case. Voids or cracks will cause excessive increase in burning areas and internal pressure that could rupture case. Performance outside of tolerance contributed by several factors such as thrust, burn time, and impulse.
Motor ignition system	Electrical failure in circuitry or power source can delay launch. Failure to ignite or slow ignition caused by defective squib, initiator, or main charges.
Aerodynamic control surfaces and structure	Aerodynamic failure from fin breakage. Aerodynamic failure from maladjustment or change in fin incidence angle leading to instability of vehicle. Aerodynamic failure from misalignment of longitudinal axes of mated components.
Launcher boost grain	Failure to ignite and burn within the time constraints determined by launch thrust requirements will affect vehicle performance. Excessive burn rate resulting from grain deterioration or damage can cause pressure transients that decrease performance or damage launcher and vehicle.

Table 11. Potential Reliability Problem Areas (Cont)

Components	Failure Type
PAYLOAD FUNCTIONS	
Payload separation/ expulsion	Excessive burn rate or detonation arising from grain deterioration or damage can impose high shock loads upon instrument package during ejection and result in loss of data returns. Separation forces outside of performance tolerance caused by excessive burn time of mortar grain, and leakage of generated gases will prevent effective payload ejection and deployment.
Separation/ expulsion system timer	Failure of time delay system as result of defective or mechanically damaged fuse would prevent expulsion of payload.
Parachute system	Failure to deploy and loss of payload utilization caused by failure or high payload breakaway forces. Parachute streaming after expulsion accompanied by rapid descent of payload is attributed to insufficient stabilization of rocket and tumbling of parachute payload combination. Parachute instability at altitude delaying canopy inflation during initial portion of descent will reduce value of sensor data at high altitudes. Twisting of parachute load lines resulting from higher rate of rotation of payload with respect to expanding parachute pack can delay canopy opening and stabilization.
Instrument payload	Failure of instrument to operate after separation caused by high shock or acceleration imposed by parachute mortar or by handling and launching.
Power supply	Failure of battery power supply caused by shelf life deterioration, prolonged stand-by power drain, or internal damage from shock or altitude depressurization. Power loss caused by failure of battery connections to radiosonde load.
Sensors	Failure of sensors caused by shock or acceleration would cause loss of data other than winds aloft. Delay or failure to expose sensors after payload expulsion or sensor damage incurred during removal of the nose fairing will adversely affect data returns.

Table 12. Reliability Comparison—Ascent to Altitude Functions

System	Tube Launcher, Piston, Spacecraft	Rail Launcher, Shoes, Rail, etc.	Squib and Motor Ignition	Tube Launcher Grain Ignition	Motor #1 Burn	Motor #1 Separation	Ignition Timing Motor #2	Squib and Motor #2 Ignition	Motor #2 Burn	Aerodynamic Surfaces and Structures	Additional Aerodynamic Surfaces and Structures	Payload-Motor Separation	Ascent Reliability
Single-stage Motor/payload separation near apogee	0.997		0.999	0.999	0.970					0.985			0.95
Dual-thrust-level motor	0.997		0.999	0.999	0.965					0.985			0.946
Two-stage Payload/second-stage separation near apogee		0.997	0.999		0.970	0.997	0.998	0.998	0.970	0.985	0.985		0.903
Single propulsive stage-stabilized payload separated at burn-out	0.997		0.999	0.999	0.970					0.985	0.985	0.997	0.934

Table 13. Reliability Comparison—Payload Functions

System	Ascent to Altitude	Separation Timing	Payload Expulsion	Parachute Deployment	Sensor Operation	Radiosonde Operation	Payload Operations Reliability	Net Reliability
Single-stage Motor/payload separation near apogee	0.95	0.998	0.950	0.985	0.990	0.968	0.895	0.85
Dual-thrust-level motor	0.946	0.998	0.950	0.985	0.990	0.968	0.895	0.846
Two-stage	0.903	0.998	0.950	0.985	0.990	0.968	0.895	0.808
Single propulsive stage-stabilized payload separated at burn-out	0.934	0.998	0.945	0.985	0.990	0.968	0.868	0.810

warranted at the present relative development level of the dual-thrust motor, but continued use of this motor configuration could lead to equality with the estimated reliability associated with the single-thrust-level system.

The 0.97 apportionment for reliable burn of the conventional end-burning motor configurations appears realistic. While the burn function has shown an initially higher success during developmental testing of various motors in this relatively small size category, variations in one representative motor made in quantity at different sites have resulted in accepted unit static test firing success levels ranging from 0.95 to 1.0, dependent upon the quality control practices of the particular site.

Reliability experience levels attained with sequential testing of rocket motors also indicate a general trend wherein 0.90 is attained between the 10th and 20th test and 0.95 is attainable by about the 40th test. The apportionment of 0.999 for initial-stage ignition and 0.998 for subsequent stages is well substantiated by reports on characteristic off-the-shelf pyrotechnic devices. A similar level is expected for the launcher boost charge ignition.

An attempt was made to develop the variation in expected reliability level as a function of various vehicle environments or attributes such as temperature, type of propellant, thrust-level size, burn time, etc. Unfortunately, correlation sufficient to draw meaningful conclusions was not attained. For example, Figure 45 shows the demonstrated reliability,

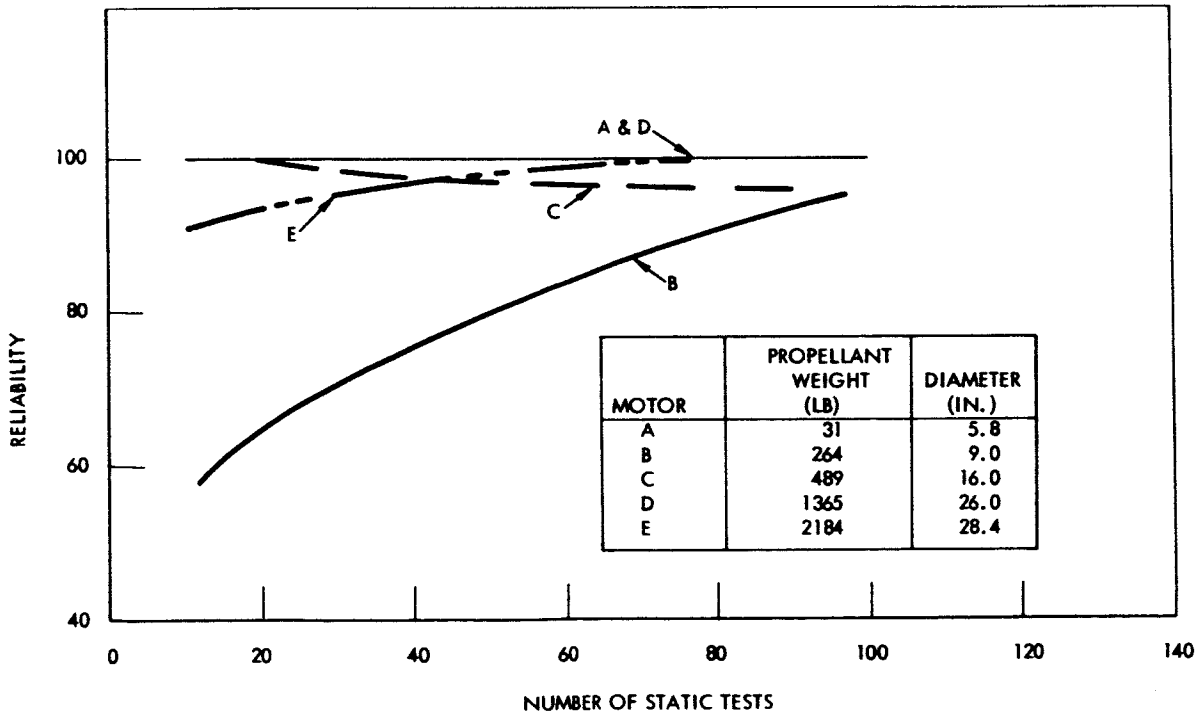

MOTOR	PROPELLANT WEIGHT (LB)	DIAMETER (IN.)
A	31	5.8
B	264	9.0
C	489	16.0
D	1365	26.0
E	2184	28.4

Figure 45. Representative Motor Reliability Test Data

based on static test firings, of motors of various sizes. For this sample, both the smallest and second-largest motors completed 100 tests without failure. The second-smallest motor, on the other hand, started out with a high failure rate but, presumably due to design changes, eventually attained a 95 percent reliability level.

Table 14 presents additional failure data on relatively large samples of the motors shown in Figure 45. As indicated, the major causes of static test failures were associated with the low-temperature tests; case malfunctions showed the next-highest failure mode. The flight test history of the same motors, however, yielded four failures in the entire sample, with the only identifiable one attributed to the ignition system. Reference 3 develops a case for viewing failure percentages as being inversely proportional to the vehicle diameter; however, design approaches and material selection can be used to negate the arguments presented in the reference.

Table 14. Representative Motor Failure Mode Data

Motor	Tests	Failures	Failure Cause				
			Case	Nozzle	Ignition	Propellant Temperature Test	
						Ambient	Low
STATIC TEST							
A	2160	16					16
B	164	10	7	3			
C	247	7	3	1	1	1	1
D	128	0					
E	348	2			2		
Total	3047	35	10	4	3	1	17
FLIGHT TEST							
A	5000	1			1		
B	150	0					
C	88	0					
D	105	0					
E	875	3	Causes Unknown				
Total	6218	4					

The duration of motor burn would, at first glance, appear to affect the reliability factor; however, experience in the testing of solid motors indicates that this apportionment factor must be considered from an attribute standpoint rather than from a mean-time-between-failure approach. Reference 4 discusses this topic in some detail.

The number of stagings required during the flight to apogee will significantly influence the overall reliability since discrete, series functions can be identified. Thus, all other factors held constant, system approaches with multiple separations must yield inherently lower reliability values.

From a reliability of altitude attainment standpoint, the candidate configurations are ranked in the following order:

1. Single-stage/apogee separation
2. Dual-thrust
3. Single propulsive stage-stabilized payload separated at burn-out
4. Two-stage

Obviously, utilization of such reliability improvement items as redundant circuitry in some cases and not in others could influence the relative standings; however, to provide a reasonable comparison basis, such techniques were avoided in all cases. The first two systems rank very close together, with the single-stage, single-thrust-level motor having a slight edge, at this point in time, due to its longer usage.

The proof of attainment of the reliability goal must come ultimately from test firings. Figure 46 indicates the number of tests required and allowable failures to demonstrate a prescribed reliability level at a particular confidence factor. At least 13 successful flights are needed to demonstrate 0.95 reliability at a 0.50 level of confidence. One failure in 33 flights or two failures in 53 flights would provide the same relationship.

COMPARATIVE PRODUCTION COST EVALUATION

To provide compatible cost estimates for the candidate systems, the following ground rules were adopted in all cases:

1. Constant 1965 dollars are assumed.
2. No RDT&E amortization is applied.
3. Maximum market is 1000 vehicles.

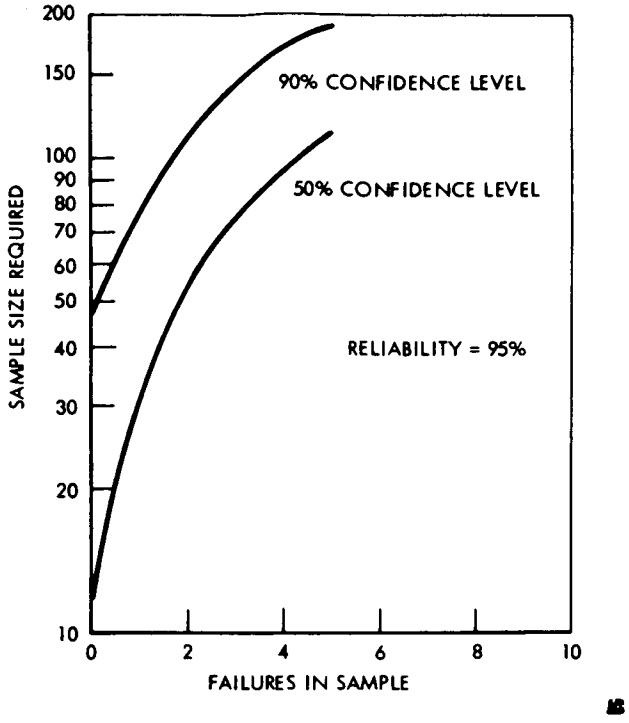

Figure 46. Sample Size Requirements

4. Local labor, material scrappage rates, and learning experience applies.

5. Ground support equipment costs are excluded.

6. Comparative vehicle cost estimates include the airframe, motor, propellant, parachute, and other airborne subsystems excluding the payload instrumentation, since it is assumed constant for all cases. (AN-DMQ 9 estimates are discussed separately.)

The general procedure followed in developing the comparisons utilized standard economic analysis techniques. Material and fabrication costs per pound are estimated for unit number one of a given configuration and adjusted, based on historical data, for procurement cost factors, scrappage adjustments, special handling or fabrication techniques, and net system complexity factors. The unit one costs are then projected on historically based learning curves for both labor and materials to obtain average unit costs at various production levels.

The resultant average cost estimates for the four configurations and the noted quantities are summarized in Table 15. While the comparative

relations and trends are considered valid and are compared in Figure 47 with a fairly wide spectrum of existing sounding rockets, certain comments on the absolute magnitude of any given cost estimate appears worthwhile:

1. For this general type of vehicle, it does not appear that the general cost-quantity slope can be changed significantly unless a substantially larger maximum buy is assumed. The particular break-point at which high rate tooling, fabrication, and assembly line techniques will pay off is, unfortunately, not readily apparent.

2. The analysis indicated that costs of labor, regardless of the configuration, represented about 60 percent of the total cost of 1000 units. This makes the absolute estimate extremely sensitive to geographical location. For example, a potential reduction of approximately 20 percent (on the average unit cost for quantities of 1000) is estimated when production is assumed to take place in a lower labor rate location. NAA West Virginia facility data were used as the model for this comparison.

Table 15. Estimated Average Unit Cost Comparison

System	Quantity		
	50	100	1000
Single-stage apogee separation	$1930	$1720	$1250
Single propulsive stage-stabilized payload separated at burn-out	2050	1840	1320
Continous-burn, dual-thrust level	1980	1790	1300
Two-stage	2230	2030	1460

Payload Instrumentation Costs

The AN/DMQ-9 was chosen as the model payload for all vehicle configurations of this study. Data obtained from the Cambridge Research Laboratory, Bedford, Mass., indicate that the cost of the current experimental units is around $1000. For small orders, it is expected to drop to the $500-600 level, with eventual decrease (dependent upon quantity order) to the $200-300 range. The AN/DMQ-6 is understood to have fallen into the region of $200 without transponder to $300 with transponder. Reduction much below this level does not appear realistic, since the estimated cost of one end item instrument—the thermistor bead for measuring temperature—is $60 including the calibration curves.

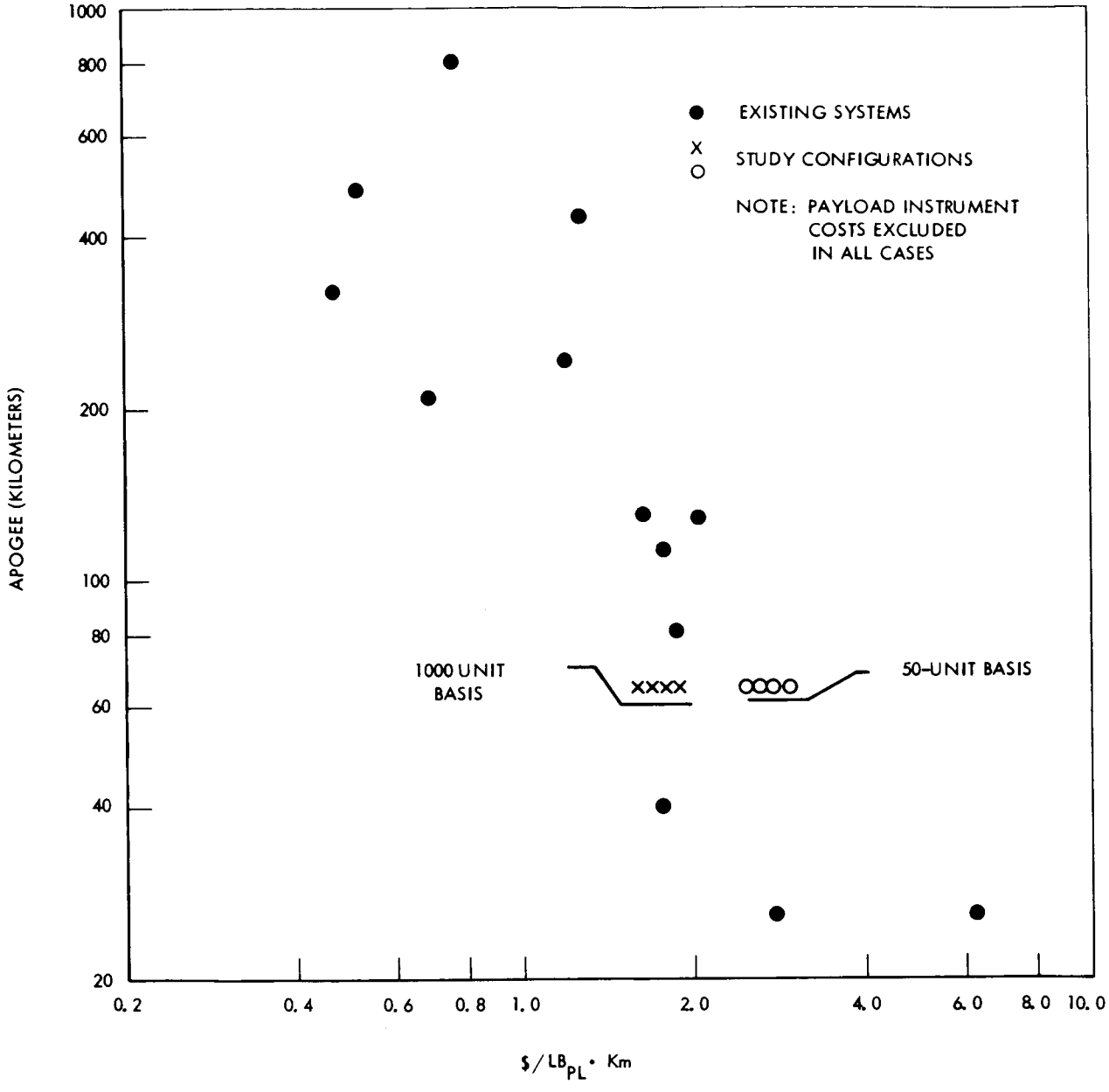

Figure 47. Cost, Apogee, Payload Comparison

Launcher Costs

To provide a more complete picture of overall cost elements, launcher cost estimates were made using the tube launcher configuration discussed in the System Design section of this report and the applicable ground rules previously outlined. In this case, however, a maximum number of 100 units was assumed. The estimated cumulative average cost per unit launcher that resulted from this evaluation were:

Units	Unit Cost
10	$5600
100	$3900

Cost Evaluation Summary

The ranking of the candidate systems, on the basis of estimated production cost, is:

1. Single-stage apogee separation
2. Continuous-burn-dual-thrust level
3. Single propulsive stage-stabilized payload separated at burn-out
4. Two-stage

Since the vehicle approach chosen for the study provides sufficient payload flexibility to obtain more than one telemetered measurement per flight, it is of interest to consider the net system cost aspects on a per measurement basis.

Based on the overall reliability assessment (ascent plus payload functions) discussed in the previous section, the single-stage apogee separation approach yields 850 successful launches per 1000 firings. Vehicle cost, for the 1000 systems, is $1,250,000, which, with an estimated average cost of $250 each for the AN/DMQ-9-type instrumentation package, brings the total vehicle system costs to $1,500,000. The cost per successful launch is $1765. With the minimum capability of two active measurements per payload plus the wind measurement, the average cost per measurement is $588. This, of course, is vehicle system cost only and excludes all support functions and equipments.

With continued growth in instrumentation techniques, the attainability of four measurements (in addition to wind) appears feasible. The experimental AN/DMQ ( ) (XE-1) can, in fact, continuously transmit four channels of information. Estimated quantity production costs of an advanced payload are $500 each, which, again on the basis of 1000 firings, yields an average vehicle system cost of $412 per attained measurement.

Reliability growth has not been accounted for in the preceding estimates. With a reasonable growth pattern, the estimated cost for the latter case would be expected to decrease to under $400 per attained measurement.

Similar projections can be made for the other configuration approaches considered. Table 16 lists the comparison of the candidate vehicle systems on a per measurement basis. Reliability factors used are in accordance with the apogee plus payload function assessment discussed previously. Costs of associated support functions and equipment again are excluded.

Table 16. Candidate System Comparisons on a Cost Per Measurement Basis

System	Measurements	
	2 + Winds	4 + Winds
Single-stage, apogee separation	$588	$412
Single propulsive stage-stabilized payload separated at burn-out	652	454
Dual-thrust	610	425
Two-stage	709	485

When viewed on this basis, the system costs appear reasonably competitive with the least expensive of current sounding rocket types. For instance, a widely quoted cost estimate for a current motor (associated with a smaller payload vehicle) plus a chaff-only package is $750. This yields, of course, only one measurement—wind—and presumes a 100 percent success ratio. The addition of one active measurement—temperature plus a transponder system—yields an estimated cost per measurement of approximately $450 on a 100 percent success ratio basis.

SYSTEM SELECTION

The candidate systems have been evaluated on the basis of performance, reliability, and production cost. It now remains to perform the composite

comparison and select the most optimum approach. Unfortunately, although not unexpectedly, the choice is not a clear black-and-white matter; it appears to be a blending of shades of gray.

The desired performance appears to be attainable with any of the configurations. Overall weight differences appear to be relatively small, and more detailed design of each system may show some variance, although the general relationships are expected to hold.

Launcher requirements appear to be about equal for all cases, with a definite need for attainment of a relatively high velocity prior to freeing the vehicle.

Reliability evaluations show the first major separation in that the two-stage and separation at burn-out system rank, on a relative basis, considerably lower than the single-stage, apogee-separation and the dual-thrust systems. The latter two, however, are decidedly close, and continued usage of the dual-thrust approach could place it in a tie position.

Comparative production costs follow the same trend as the estimated reliability, but, here again, fringe factors could influence the outcome. For instance, sounding rockets appear to have, for a large part, historically used motor systems developed for other programs. If a particular type of motor is currently in production and is compared to another type that requires new tooling, certification, spares provisioning, etc., a switch in relative standings could occur. This is outside the ground rules of this study, but is a consideration that may ultimately influence a go-ahead decision.

The same rationale appears to hold true for development program costs and risks, although at this time the dual-thrust-motor does not appear to have reached the experience level attained by the conventional end burners and must, therefore, be considered a greater risk.

Range safety aspects tend to lead inherently toward early motor separation to reduce spent case dispersion. Here again, however, a generalization must be avoided, since particular range requirements will dictate the answer and it may vary with the specific firing site chosen.

Other aspects, such as maintainability and logistics, do not yield widely significant differences, although multiple separation circuitry systems and multiple components of a hazardous type present more problems than do the singular systems.

A semiqualitative ranking of these items is possible, however, and is shown in Table 17. The table also presents a normalized effectiveness evaluation based only on the estimated production cost/reliability ratio. It is of interest to note that the net rankings are identical in both cases, with

the single-stage, apogee-separation system maintaining a slight lead over the dual-thrust approach. The variance between systems is somewhat less when only reliability and cost are considered.

The evaluation must, then, give preference to the single-stage, apogee-separation system approach. The dual-thrust-level system is a very strong contender.

On the basis of the established ground rules and the net evaluation criteria discussed in this section, the single-stage, apogee-separation system was selected for the preliminary design phase of the study.

Table 17. Candidate System Comparisons

SEMIQUALITATIVE POINT RANKING									
System	General Performance	Relative Reliability	Relative Cost	Range Safety	Maintain-ability	Logistics	Prop. Develop. Risk	Total	Points / Max. Points
Single-stage apogee separation	3	4	4	3	4	4	4	26	1.0
Single propulsive stage-stabilized payload separated at burn-out	2	2	2	4	3	3	4	20	0.77
Dual-thrust	4	3	3	3	4	4	3	24	0.92
Two-stage	4	1	1	2	2	2	4	16	0.62

RELIABILITY/COST RANKING		
System	R/C	R/C / R/C Max.
Single-stage apogee separation	0.00068	1.0
Single propulsive stage-stabilized payload separated at burn-out	0.00061	0.90
Dual-thrust	0.00065	0.96
Two-stage	0.00055	0.81

SYSTEM DESIGN

VEHICLE DESCRIPTION

The selected vehicle system concept—the single-stage/apogee-separation system—was utilized in developing a preliminary design of the sounding rocket and launcher subsystems. An inboard profile of the configuration is shown in Figure 48.

The vehicle consists of five major components: (1) nose and instrument package assembly, (2) parachute compartment, (3) separation system, (4) motor assembly, and (5) nozzle and fin assembly.

Nose and Instrument Package Assembly

The nose assembly is fabricated from phenolic resin impregnated glass cloth (such as MIL R9299, type 2) and is built up in laminated sections to provide the necessary structural integrity and thermal protection during the ascent phase of the mission. The VonKarman ogive is attached to the nose mounting ring by a series of screws. The mounting ring is fabricated of aluminum alloy and has provisions for the attachment of the parachute compartment shell, the separation charge, and the positioning and retainment of the instrument package. A base plate provides for shock mounted attachment of the instrument assembly and for attachment of the parachute. The outer edge of the base plate engages the vehicle structure so that instrument package loads are introduced directly into the vehicle shell. A swivel connection is located at the center of the base plate for parachute riser line attachment. The swivel attachment method was chosen to minimize wind-up of the canopy support lines.

Parachute Compartment

Several possible methods of separation and parachute deployment were investigated prior to selection of the system shown in Figure 48. The methods considered are shown in Figure 49 and are outlined in the following paragraphs.

Concept 1

Concept 1 includes the stowed arrangement, separation sequence, and deployment sequence. The parachute is located in the forward portion of the nose and is followed by the instrument assembly. This arrangement was

investigated for potential aid in keeping the relative position of parachute and payload constant to reduce the tendency of shroud line entanglement.

An expulsion bag and gas generator are also located in the nose section ahead of the parachute. After the payload section has been explosively separated from the motor, the gas generator is timer initiated and the gas reacts on the expulsion bag to eject the instrument assembly and parachute from the aft end of the nose assembly.

Although this system appeared to be attractive from the standpoint of ejecting the instrument package in the descent direction, it was rejected because of poor packaging density and the undesirable feature of ejecting the parachute a relatively long distance through the structure.

Concept 2

The deployment sequence of this concept begins with the explosive separation of the nose section from the motor case. A pressure cartridge is activated by a timing mechanism and produces a pressure on the parachute package cover. The cover, in turn, pulls the parachute out of the nose section structure. As the parachute deploys, the drag force extracts the instrument assembly from the nose section. This concept appears to have several areas of questionable reliability, and was subsequently rejected.

Concept 3

In the third concept, the separation sequence is initiated by a pyrotechnic fuse, which triggers the separation charges and simultaneously allows inflation of the expulsion bag. The expulsion bag, as it expands, forces the separation of the booster and payload. This sequence completely uncovers the parachute without forcing it through a restraining structure.

This concept, since it appears to offer simplified parachute extraction and positive separation, formed the basis of the preliminary design.

The parachute compartment is designed to contain all of the necessary separation and deployment system components as well as the chute. The assembly structure consists of the forward mounting ring, the aft mounting ring, and the monocoque shell, and is designed to permit integrated installation of the separation system and packed parachute.

The forward mounting ring has provisions for attachment of the nose to the parachute compartment shell. Grooves are located near the aft face of the ring for installation of the separation charge. A segmented retainer is positioned to accept the instrument mounting ring in order to transfer loads directly into the monocoque shell. The instrument package mounting

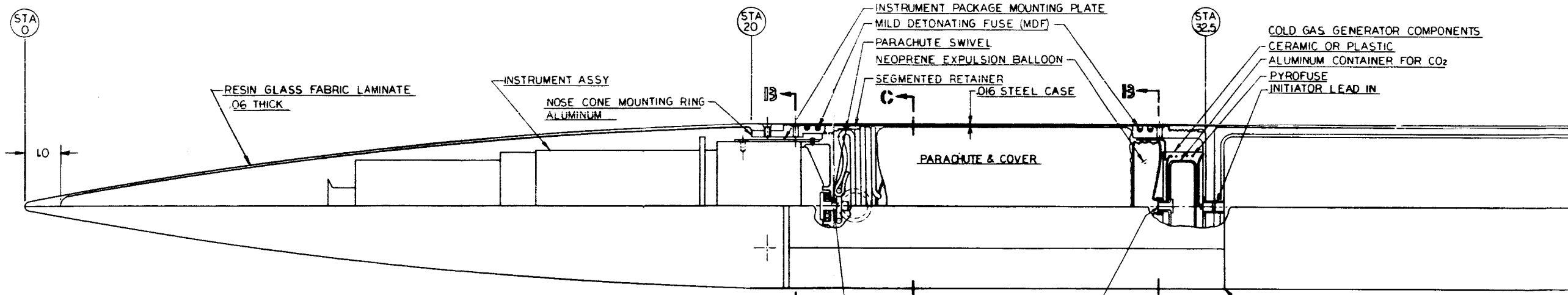

SECTION A-A INBOARD PROFILE

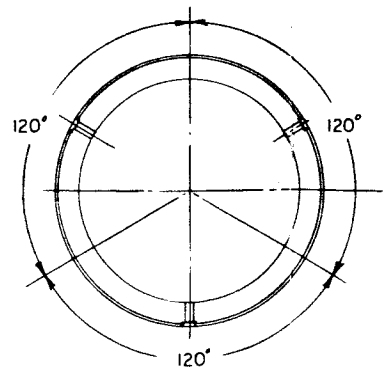

SECTION B-B

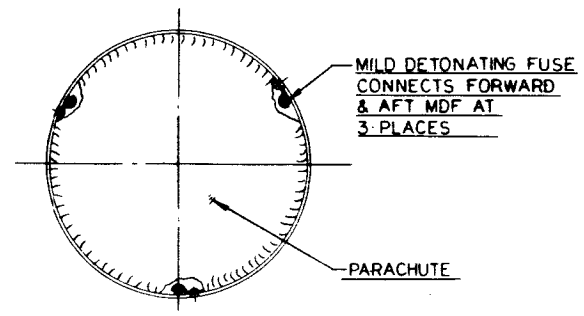

SECTION C-C

Drawing No. 7444-1

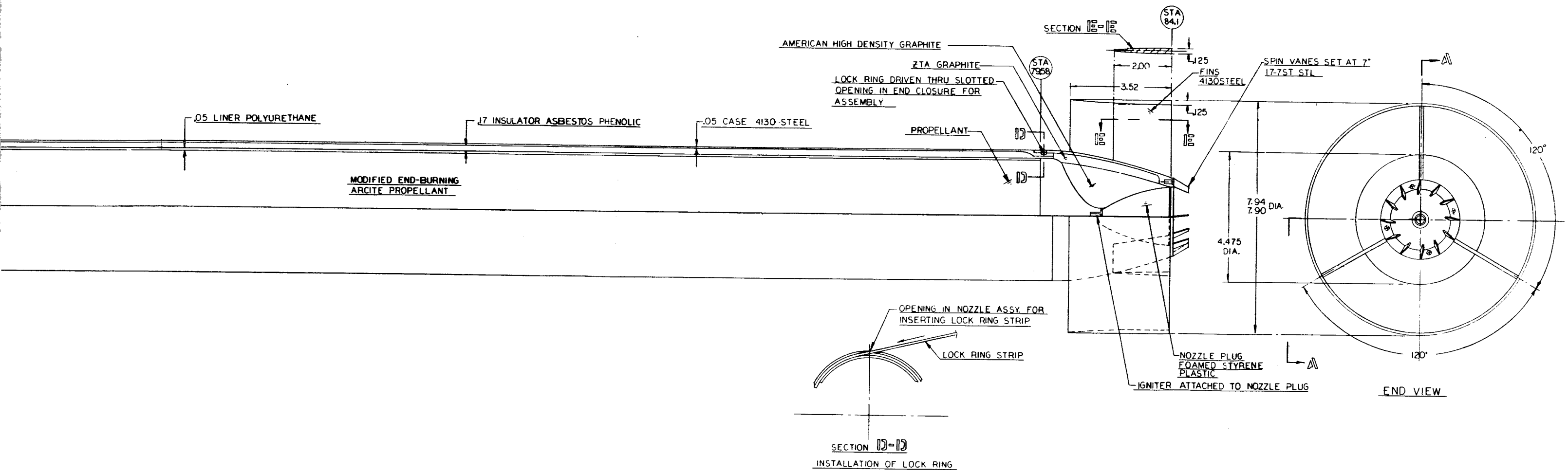

ALL DIMENSIONS IN INCHES UNLESS OTHERWISE NOTED

Figure 48. Inboard Profile

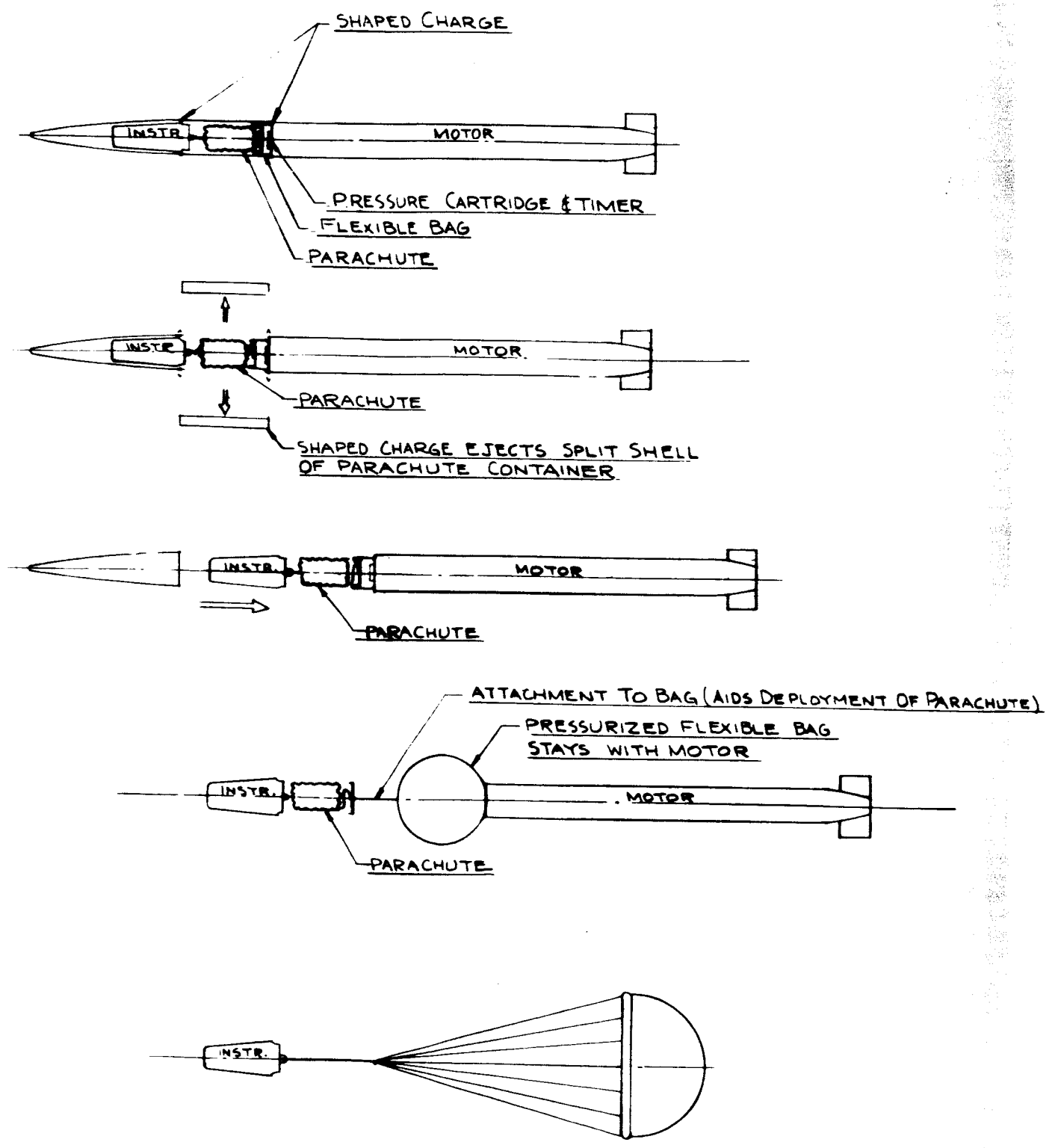

PARACHUTE DEPLOYMENT CONCEPT #3

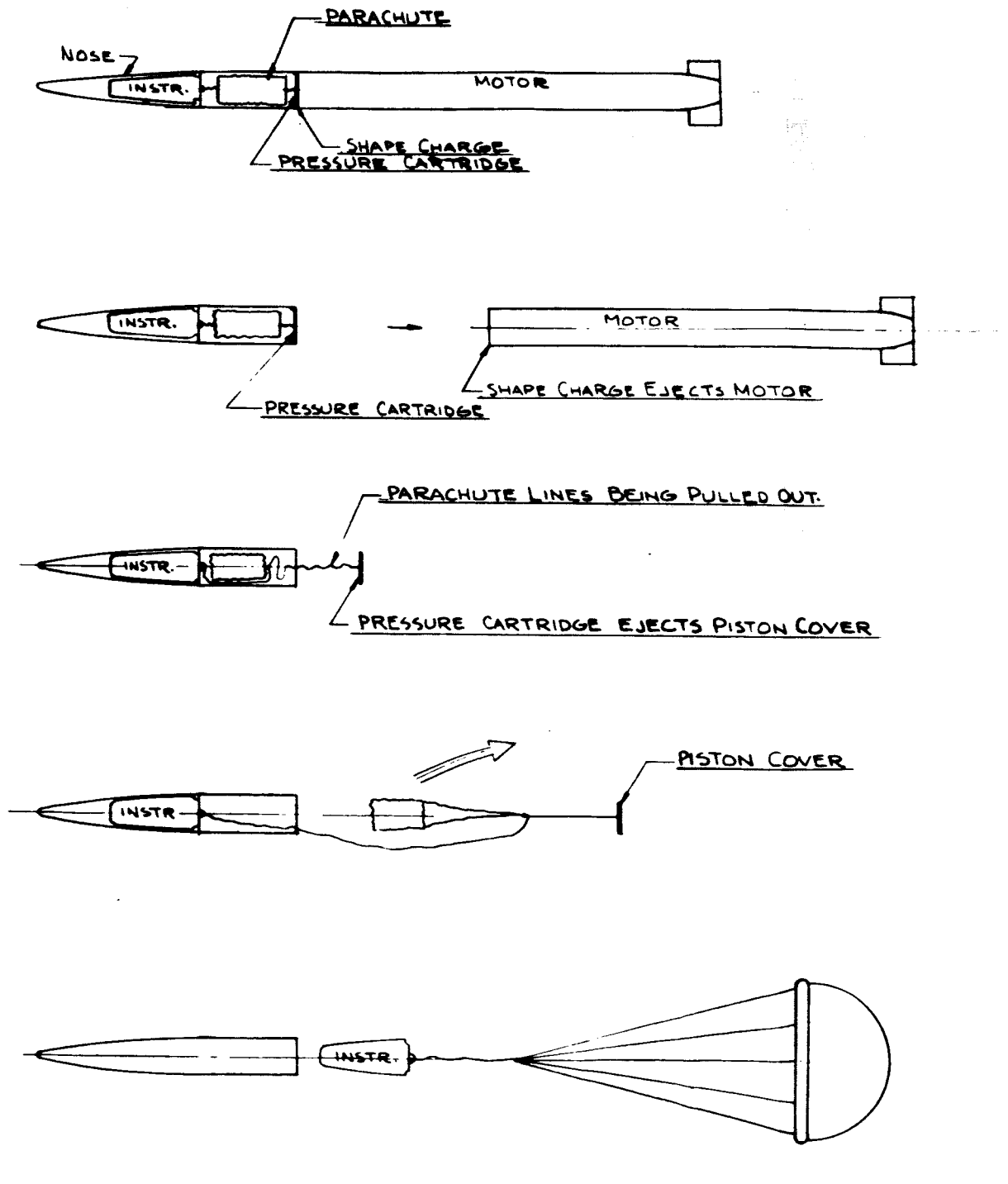

PARACHUTE DEPLOYMENT CONCEPT #2

Drawing No. 7444-3

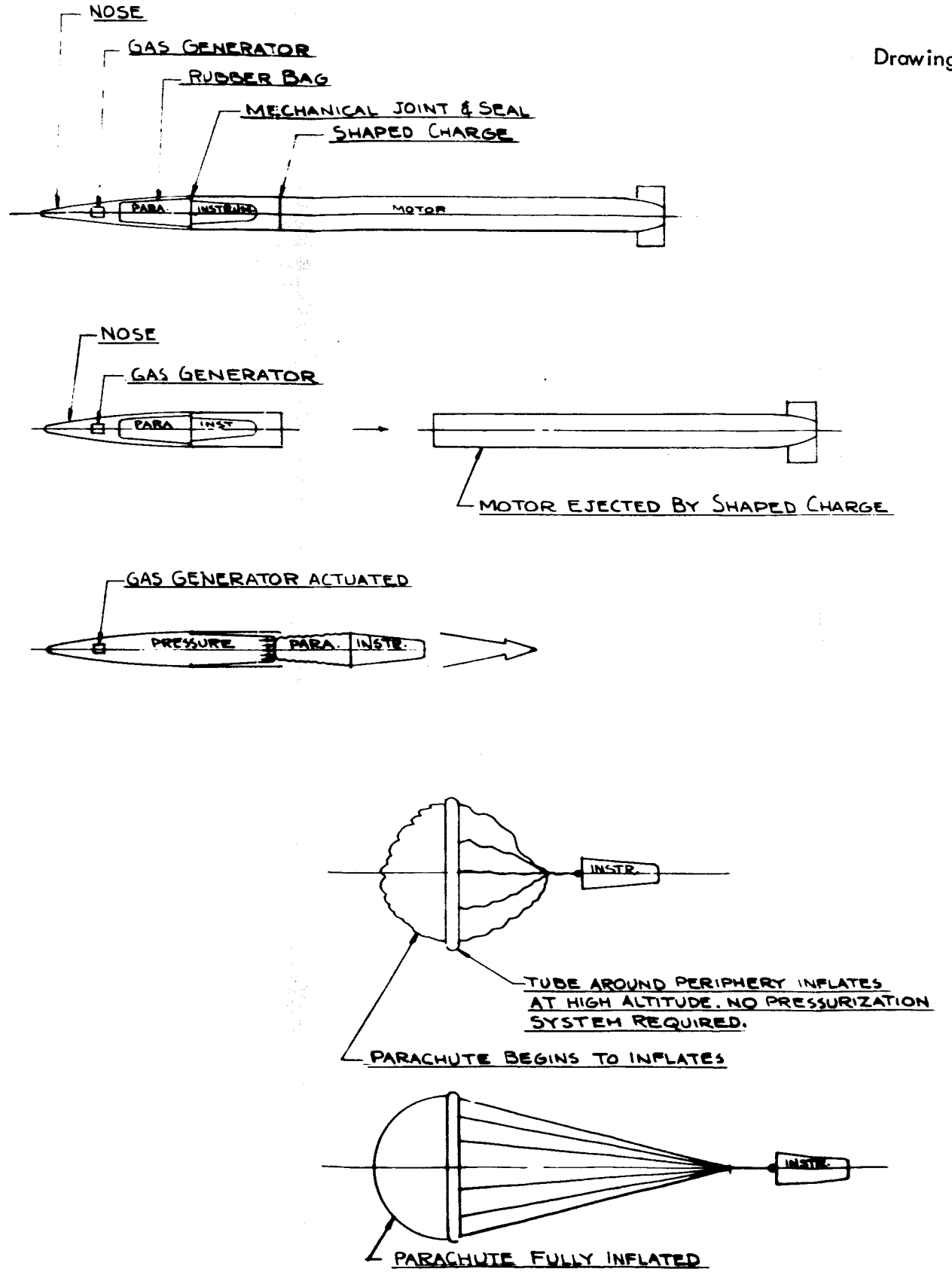

PARACHUTE DEPLOYMENT CONCEPT #1

Figure 49. Parachute Deployment Concepts

plate is installed between the retainer and nose mounting ring so that no fasteners are required and a complete release of the instrument package-parachute combination is obtained at separation.

The aft mounting ring is an aluminum alloy fitting recessed for installation of the expulsion gas cartridge, grooves for the installation of the separation charge, and tapped holes for the attachment of the monocoque shell.

The assembly sequence for the parachute compartment is as follows:

1. Install expulsion gas cartridge, pyrofuse initiator, and expulsion bag.

2. Install aft circumferential separation charge.

3. Install shell and longitudinal separation fuse.

4. Install packed parachute with instrument package mounting plate.

5. Install forward circumferential separation charge.

6. Install nose mounting ring.

The completed assembly is installed on the motor case by screwing it in place until snug and securing with lock screws. The instrument package can then be installed and the nose positioned and attached to the mounting ring.

Separation System

Expulsion bag inflation is accomplished with a cold gas such as carbon dioxide. The cartridge is located within a ceramic container that also houses a calibrated length of pyrofuse, which provides the necessary timing between end of motor burning and initiation of the separation sequence. The pyrofuse terminates at the discharge port of the CO_2 container and provides sufficient heat to melt the fusible plug and allow the gas to inflate the expulsion bag. Preheating of the gas is provided by the coiled pyrofuse. The pyrofuse also initiates the separation charge, MDF (mild detonating fuse), which severs the parachute compartment shell at the fore and aft ends.

Two methods were considered for longitudinal separation of the parachute compartment casing. The first consists of fabricating the compartment case in three longitudinal segments with overlapping lips. The segments are secured at the fore and aft attach rings and, upon detonation of the mild detonating fuse, are free to deploy. As the expulsion bag inflates

(to an estimated 30 psi), the parachute and payload are separated from the booster while the radial expansion of the bag also forces the severed panels of the compartment to deploy.

The second method uses three lengths of mild detonating fuse fastened to the inside of the casing. In addition to activating the forward ring mild detonating fuse, it also separates the compartment longitudinally. The fuse is separated from the parachute bag by heavy aluminum extrusions that prevent damage to the parachute from the detonation which shears the cylinder. This latter method allows use of an integral compartment casing and appears most suitable. The expulsion bag performs functions similar to those described for the segmented compartment approach.

Motor Assembly

The motor case is fabricated of 4130 steel and is insulated from the propellant by asbestos phenolic insulator material. The propellant is isolated from the insulator by a polyurethane liner.

The forward end of the motor case has a threaded flange to accept the parachute compartment assembly. A pyrofuse initiator, which is an integral part of the motor, is incorporated at the forward closure. The initiator is a small-diameter tube that runs from the propellant face, through the insulator and motor case, and terminates at the exterior of the end closure. A web is located at the center of the tube to prevent pressure leakage from the motor case. Each section of the tube is loaded with propellant grains. The grain burning in turn ignites the pyrofuse.

The aft end of the motor case has provisions for installation of the nozzle-fin assembly. The end closure is installed by accepted practices for rocket motor design and permits the motor case and propellant to be handled as a complete unit with exceptionally good access for casting the propellant in the motor case. The motor case and nozzle assembly contain mating grooves. A lock ring is inserted through a slotted opening in the nozzle assembly to secure the two sections.

Nozzle and Fin Assembly

The rocket motor nozzle and aerodynamic surfaces are integrated into a single assembly. The end closure and aerodynamic surfaces may be made of steel casting or welded titanium alloy construction. The nozzle is made of two sections: ZTA graphite bonded to the shell, and the throat section of American High Density graphite bonded to the ZTA liner.

The end closure is attached to the motor case by inserting a rectangular steel bar into mating grooves in the end closure and motor case.

Figure 48 shows one possible method of attaining desired spin characteristics. Vanes of 17-7 stainless steel are attached to the aft face of the end closure, with fins protruding into the nozzle exhaust to provide the necessary spin force. A redundant number of vanes is used so that breakage or uneven ablation of singular vanes does not effect the net spin characteristics of the vehicle. This method and other possible approaches are discussed more fully under the Trajectory and Control Characteristics subsection.

The ignitor assembly is located in the center of the nozzle throat and is mounted in a foam plastic plug installed in the nozzle. The plug provides prefiring protection as well as an excellent mounting for the ignitor. The ignitor and plug assembly disintegrates rapidly at motor ignition, thus minimizing any chance of damage to the launcher.

Weight estimates for the vehicle are listed in Table 18. Also shown in the table are the roll and pitch-yaw moments of inertia and nominal center-of-gravity positions. More detailed component design can be expected to change the noted values slightly.

ROCKET MOTOR CHARACTERISTICS

Dimensions and materials of the selected motor design are shown in Figure 48. The aluminized composite propellant properties are similar to those displayed by Arcite modified with twenty-five 0.01-inch-diameter silver wires axially imbedded in the grain to attain the desired burn rate of 2.45 inches per second at a chamber pressure of 1250 psia.

Dimensions, nozzle geometry, sea-level performance and operating characteristics of the solid motor are summarized in Table 19. Thrust and chamber pressure time histories are presented in Figure 50.

Estimated variations in average thrust as a function of grain temperature are shown in Figure 51 along with limited test data from similar-type motor firings. Corresponding burn-time estimates yield approximate ratios of 1.28 at -30 F and 0.89 at 130 F. To minimize the performance-temperature deviations substantially, it appears necessary to tailor the propellant with chemical ballastic additives to reduce the temperature-pressure sensitivity coefficients to approximately 0.15 percent per degree F.

The motor igniter assembly utilizes U.S. Flare 2M cylindrical pellets designed for rapid combustion throughout an extreme operating temperature range. The pellets are composed of 23.7 percent metallic boron powder, 70.7 percent potassium nitrate oxidizer, and 5.6 percent laminac binder mixture. Electrical impulse detonation of the squib imbedded in the igniter booster charge results in igniter combustion. The high temperature exhaust

products (oxides of boron and potassium, nitrogen, and oxygen gases) impinge on the motor grain surface, and initial combustion of the end-burning grain is achieved within 20 to 150 milliseconds from time of igniter activation.

Table 18. Estimated Component Weights and Inertias

Component	Weight (Pounds)		Moment of Inertia Slug-ft^2			
			Pitch-Yaw		Roll	
	Launch	Burn-out	Launch*	Burn-out**	Launch*	Burn-out**
Nose fairing	1.44	1.44	0.39	0.26	0.0008	0.0008
Instrument Package (DMQ-9 representative)	5.0	5.0	1.24	0.81	0.0024	0.0024
Forward ring	0.84	0.84	0.16	0.10	0.0008	0.0008
Base plate	0.50	0.50	0.09	0.05	0.0003	0.0003
Parachute assembly	4.4	4.4	0.54	0.42	0.0024	0.0024
Parachute casing	1.2	1.2	0.15	0.06	0.0015	0.0015
Expulsion bag	0.5	0.5	0.04	0.02	0.0002	0.0002
Aft ring	1.0	1.0	0.07	0.03	0.0009	0.0009
Expulsion system	0.5	0.5	0.04	0.02	0.0001	0.0001
Motor case	9.9	9.9	0.62	0.91	0.0098	0.0098
Insulation	6.0	2.0	0.28	0.03	0.0054	0.0018
Propellant (including liner)	36.2	0	1.71	0	0.0212	0
Nozzle	1.3	1.3	0.27	0.40	0.0008	0.0008
Fin assembly	2.45	2.45	0.54	0.80	0.0065	0.0065
Spin vanes	0.15	0	0.04	0	0	0
Total	71.38	31.03	6.18	3.91	0.0531	0.0283
Center-of-gravity station	50.7	43.9				

*Referenced to launch center of gravity
**Referenced to burn-out center of gravity

AERODYNAMIC CHARACTERISTICS

A substantial portion of the energy input to the vehicle is consumed in drag. It is necessary, therefore, to minimize drag by selecting a geometry of good fineness ratio and maintaining fair contours, smooth skin, and good joints.

The optimum (minimum drag/volume) fineness ratio for supersonic vehicles is so high that the structural weight required to resist bending becomes the controlling factor. The optimum can be approached with a

reasonable design, however, since the variation of drag becomes small at high fineness ratios. A typical case is shown in Figure 52.

Table 19. Propulsion System Characteristics

Propellant Grain	
Diameter	3.94 inches
Length	46.5 inches
Burn rate (at 70 F and P_C = 1250)	2.45 inches per second
Weight	36.2 pounds
Motor mass fraction*	0.68
80 Percent Bell Nozzle (15-Degree Half-Angle)	
Length (throat to exit plane)	2.278 inches
Throat diameter	0.557 inches
Exit diameter	2.083 inches
Expansion ratio	14:1
Sea-Level Delivered Performance	
Thrust output	473 pounds
Chamber pressure	1250 psia
Burn time	19.01 seconds
Propellant flow rate	1.904 pounds per second
Specific impulse	248.5 seconds
Nozzle thrust coefficient	1.555
Total impulse	8996 pound-second
*Includes motor case, insulation, propellant, liner, and nozzle assembly. Excludes fin and spin vane assemblies.	

As indicated, the drag of the selected configuration cannot be decreased significantly by raising the fineness ratio beyond that selected (19) unless very high (30 to 40) ratios are reached.

Component drag build-up and variation with Mach number are shown in Figure 53. The constant friction drag coefficient is unusual and is due to the fact that the altitude increases rapidly with Mach number, thus restricting Reynolds number variation. Some wave drag cancellation at the tail is obtained using the ring fin design. Area variation at the tail is indicated in Figure 54, along with the equivalent body used in estimating

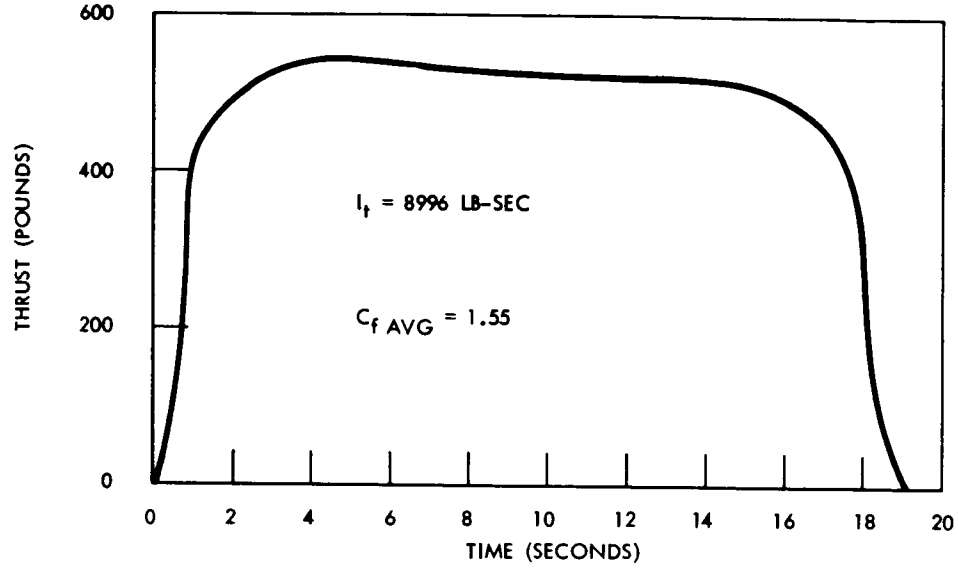

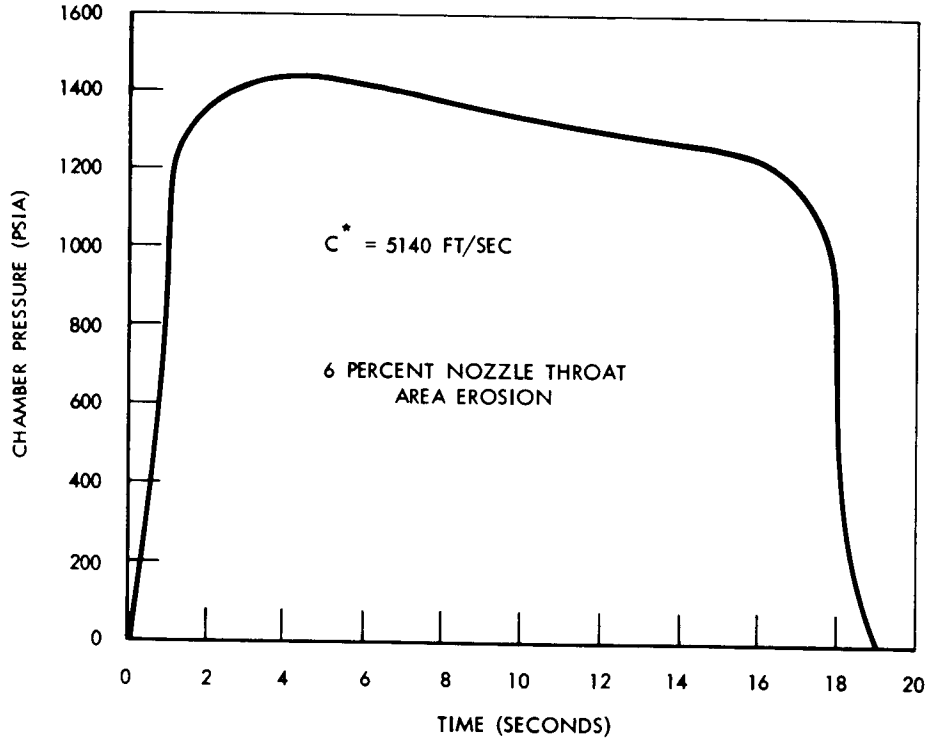

Figure 50. Motor Characteristics

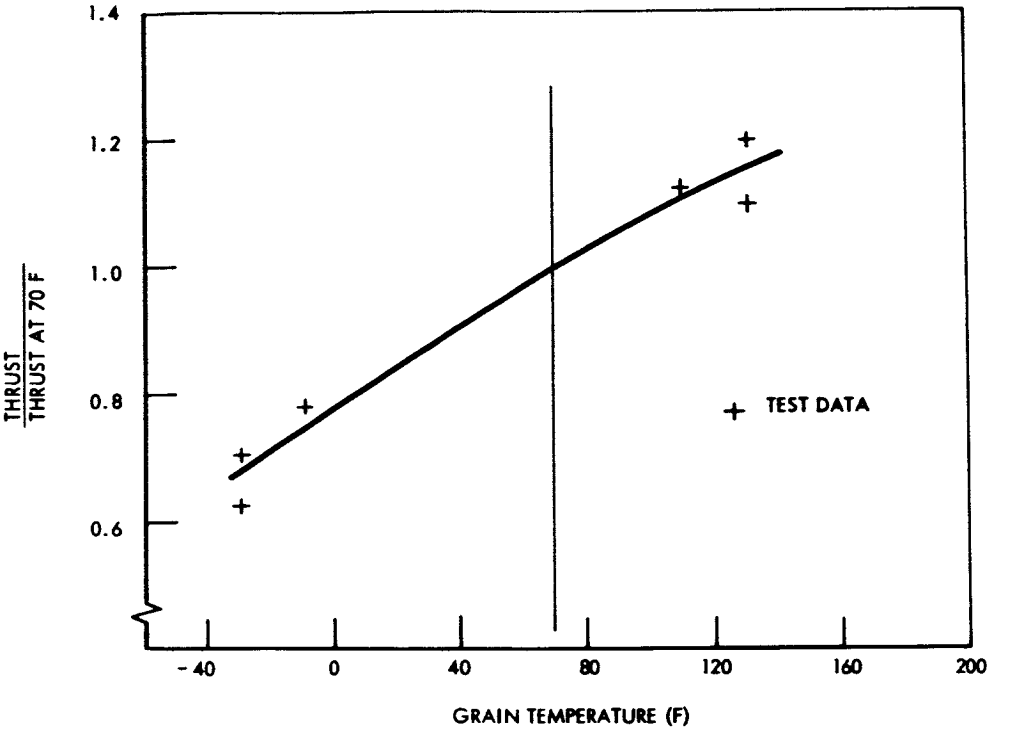

Figure 51. Average Motor Thrust Variation With Temperature

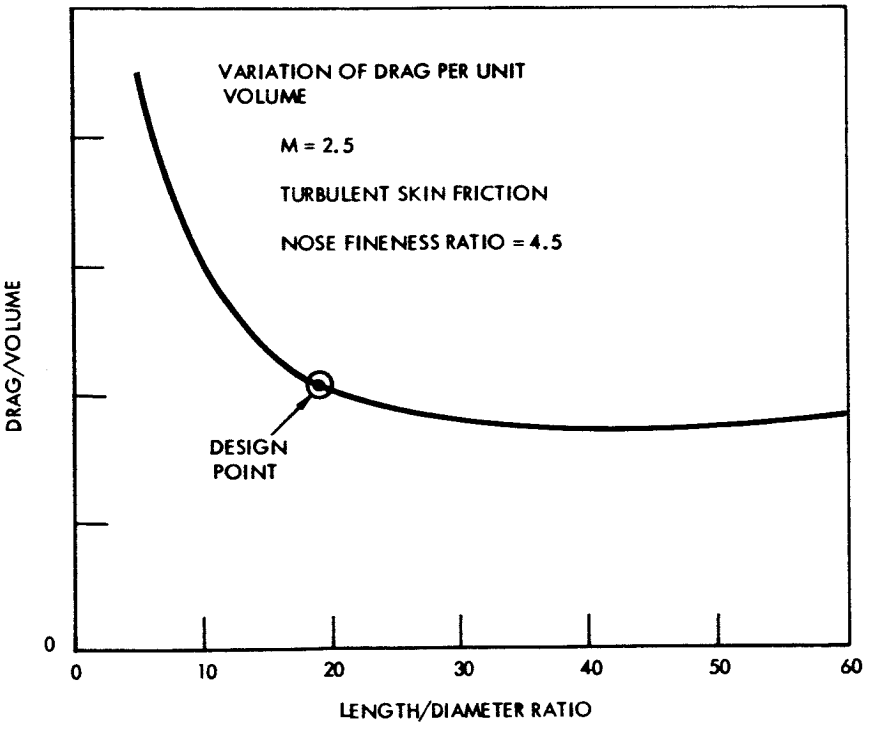

Figure 52. Fineness Ratio Selection

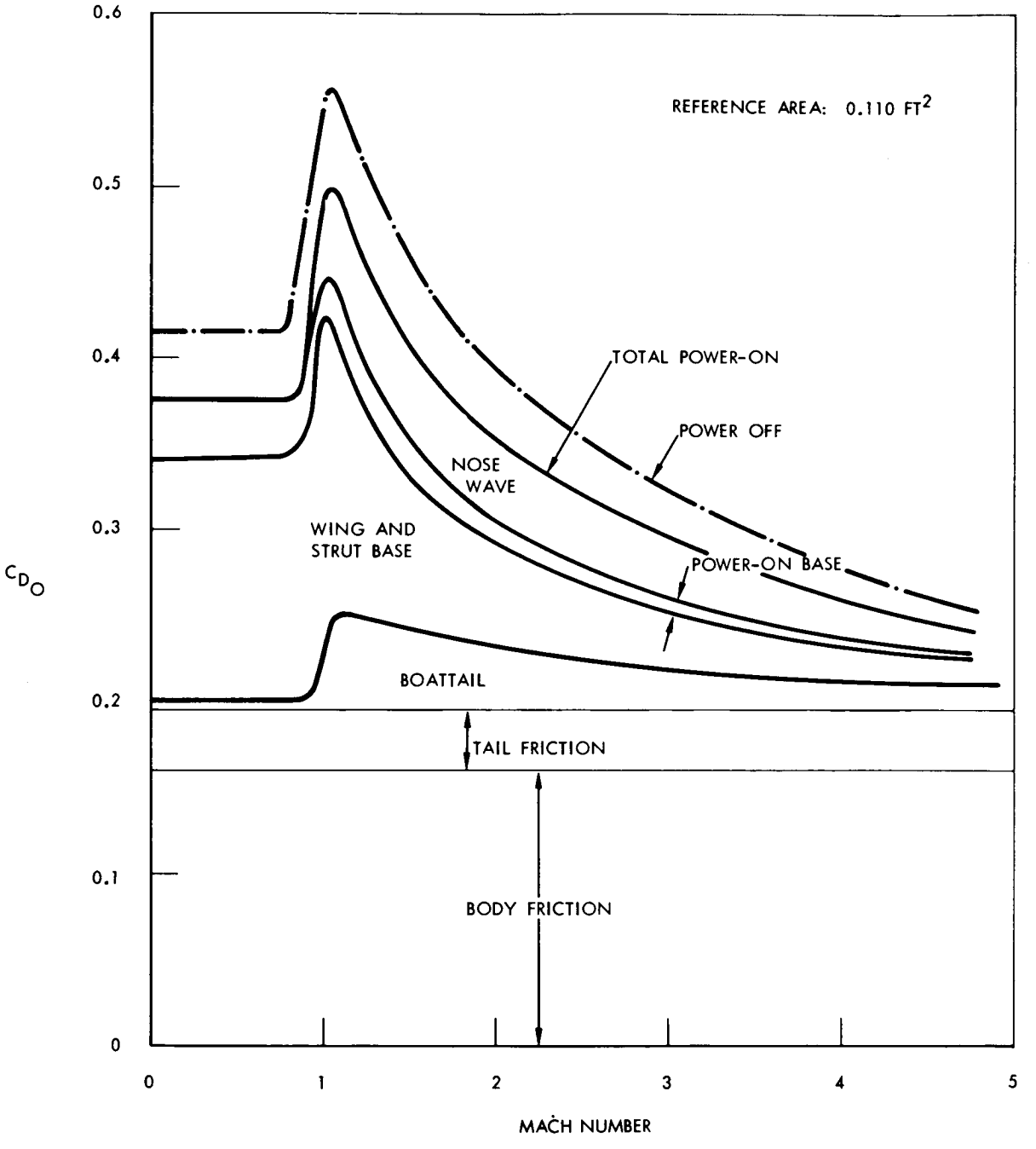

Figure 53. Estimated Drag Characteristics

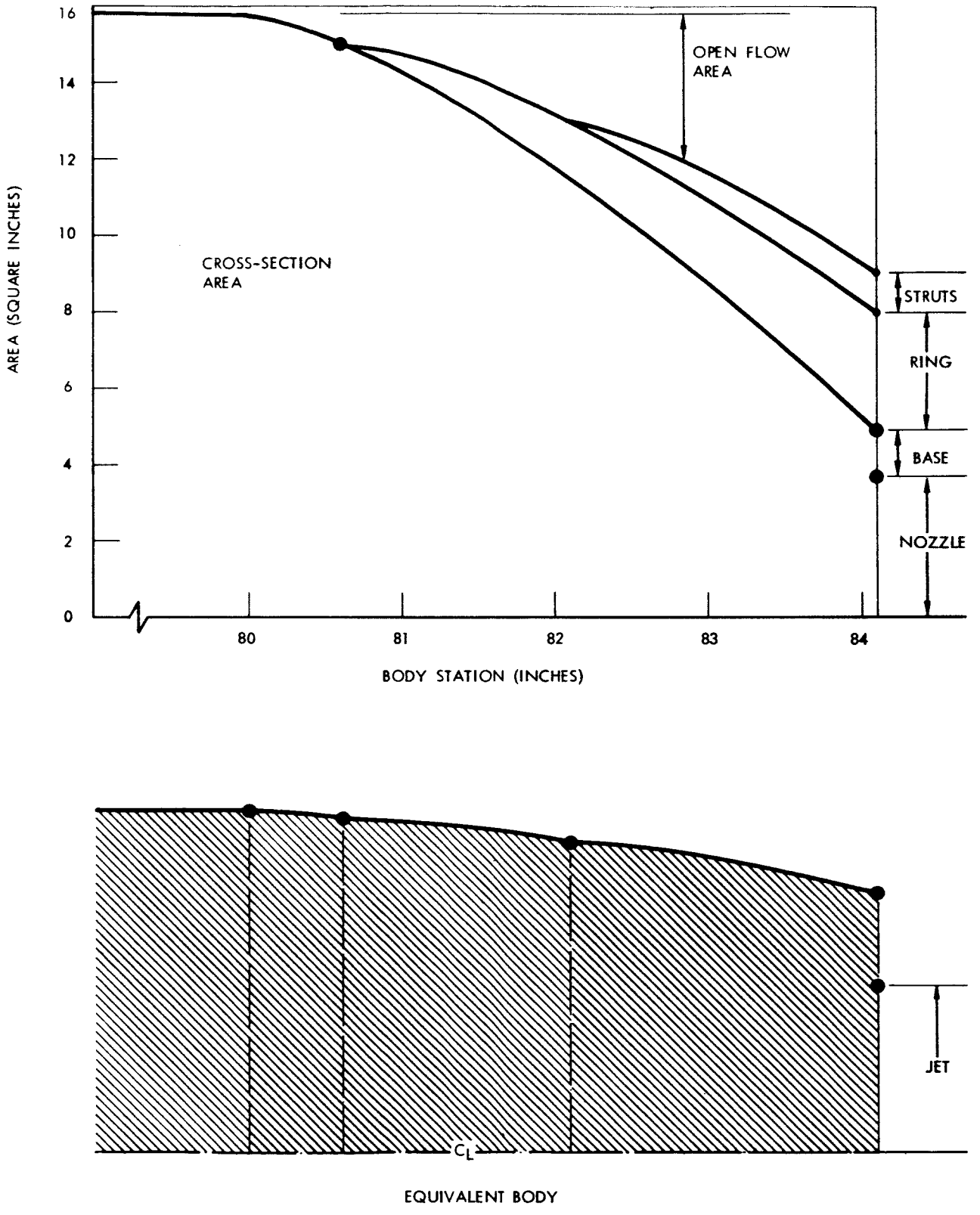

Figure 54. Boattail Equivalent Body

the bottail drag. It should be noted that the duct formed by the ring has a continually increasing area in the flow direction so that no flow blockage problems are anticipated.

Aerodynamic Derivatives

Pertinent aerodynamic derivatives are shown in Figures 55, 56, and 57.

Tail Design

The ring-fin type of tail surface was selected because it offered the advantages of a compact, rigid structure, low drag, and compatibility with tube launch techniques. Estimated normal force of the ring fin is shown in Figure 56 along with some experimental data points.

Additional data for this type of configuration may be found in References 5, 6, and 7. Designs in which the ring diameter is not much larger than the body diameter show less than theoretical effectiveness, presumably due to adverse body boundary layer effects. Boundary layer-shock wave interference can also be expected at low Mach numbers in designs where the support struts project ahead of the ring. For this design, the struts were kept thin and behind the ring leading edge, and the flow passage was kept continually expanding so that the boundary layer thickening would not produce choked flow.

Aerodynamic Heating

Estimated temperatures at the vehicle nose and 1.5 inches aft of the leading edge of the fin were calculated using computer-programed methods, and are shown in Figure 58 for the nominal trajectory. Body surface temperatures one diameter aft of the nose display a time history similar to the fin surface temperature shown.

As noted, these are surface temperatures and thus are not directly indicative of temperatures within the material itself or within the payload compartment; therefore, heat absorbed as a function of time must be considered.

Transient heating functions—heat flux and net heat absorbed—are shown in Figure 59 for a point one diameter aft of the nose. The trends displayed are also indicative of the fin area, while the nose stagnation point reaches a slightly higher net flux value (8.2 Btu/ft^2-sec).

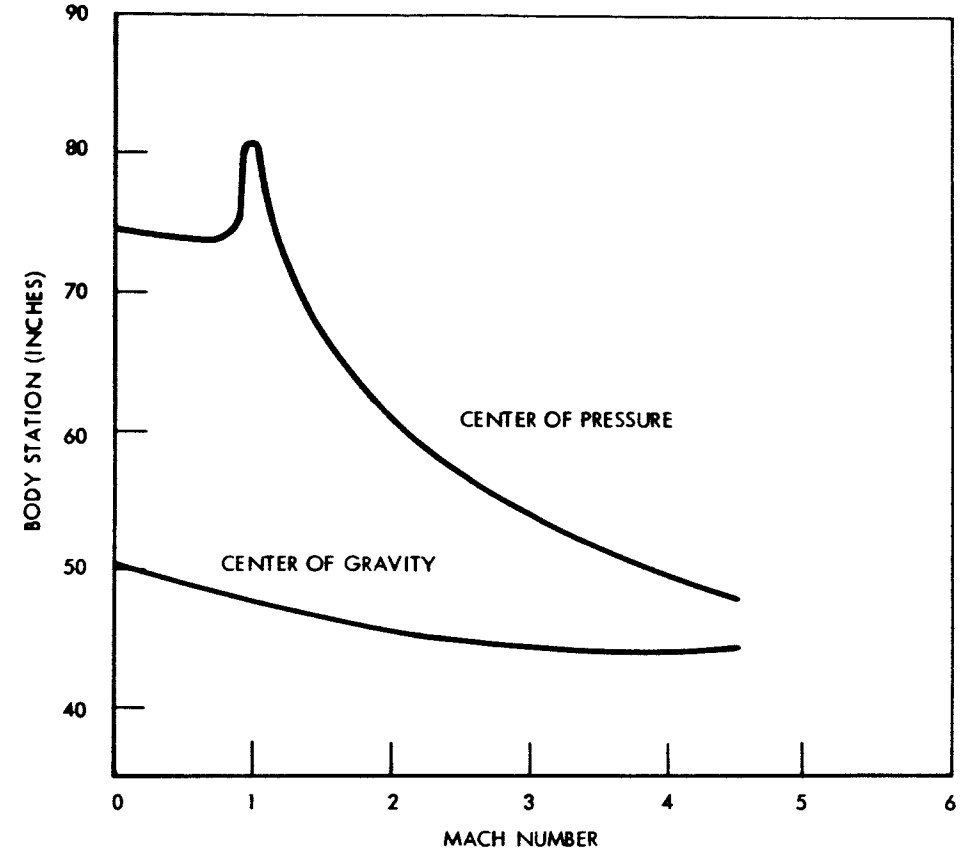

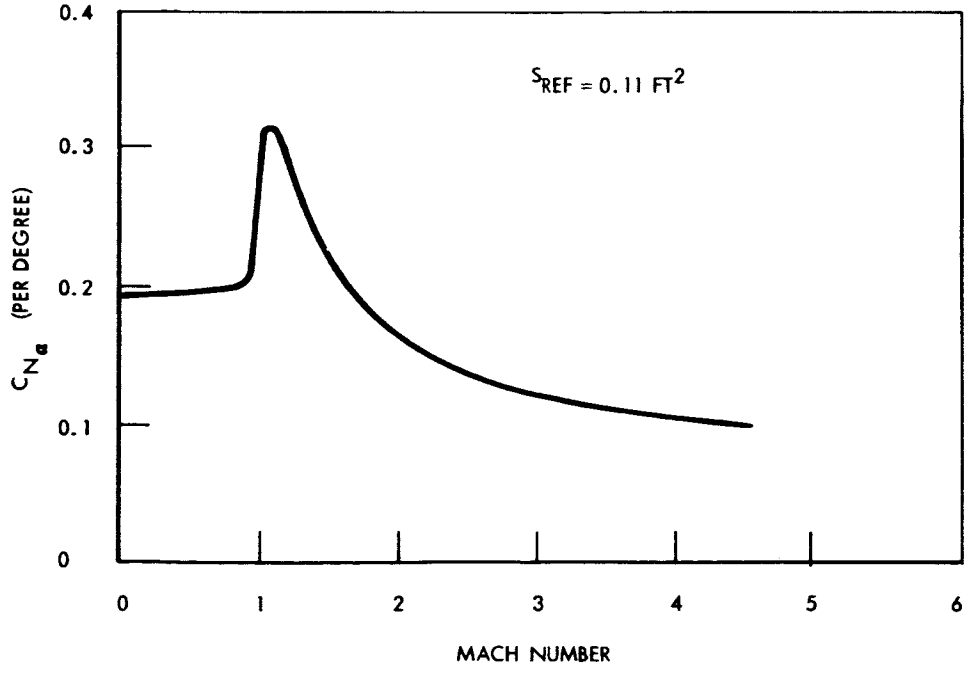

Figure 55. Estimated Aerodynamic Derivatives

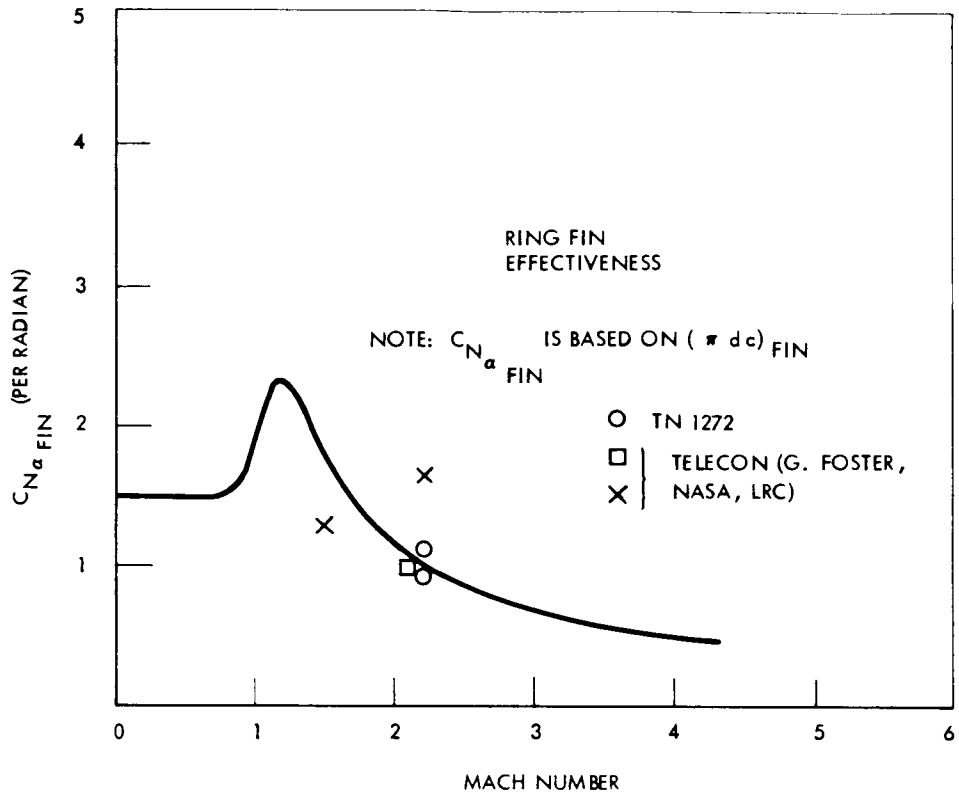

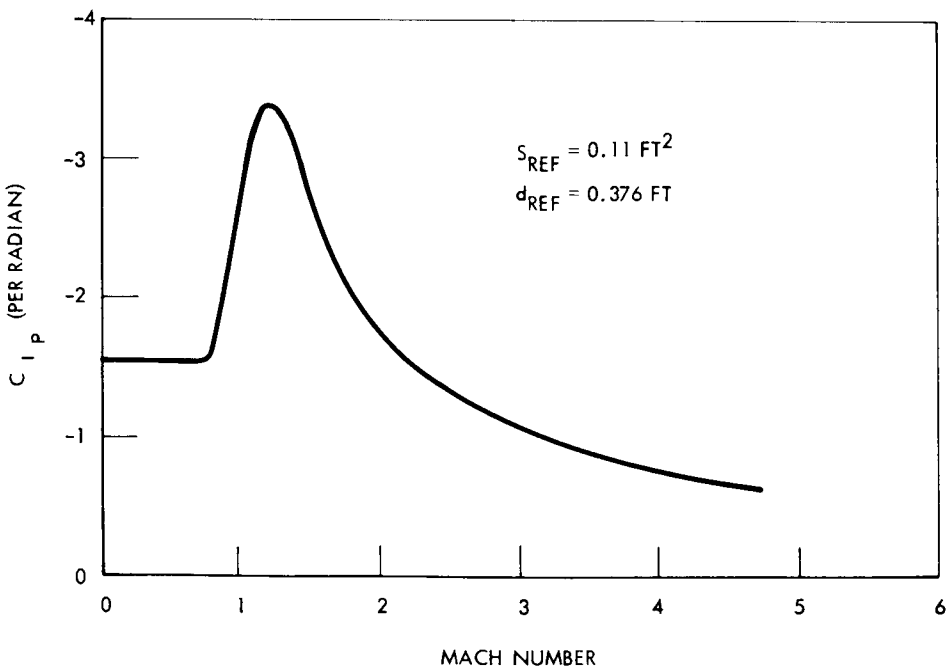

Figure 56. Estimated Aerodynamic Derivatives

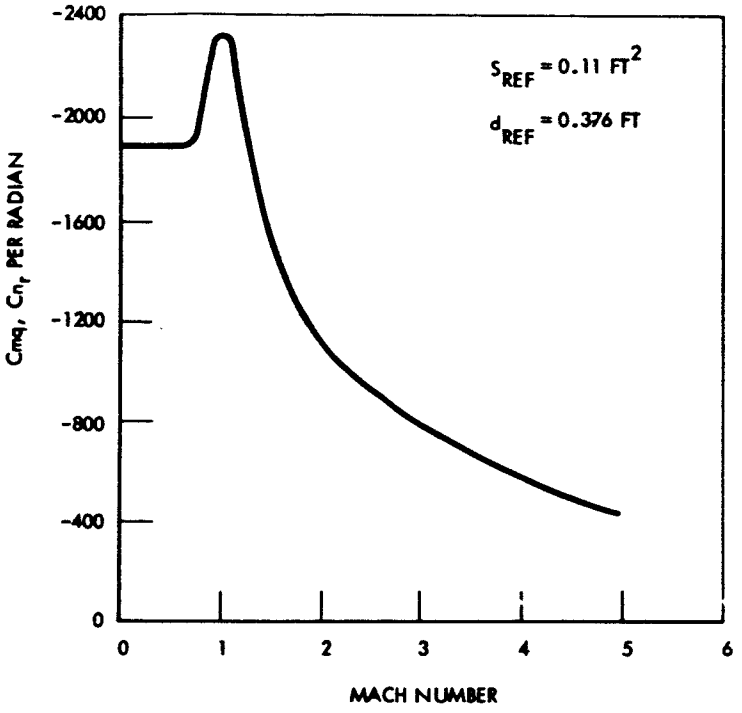

Figure 57. Estimated Aerodynamic Derivatives

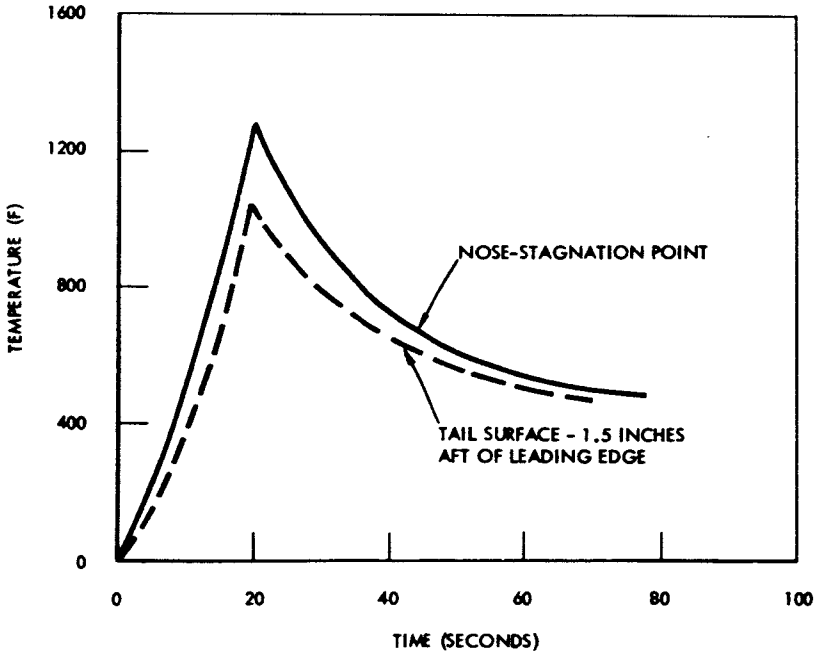

Figure 58. Vehicle Surface Temperature

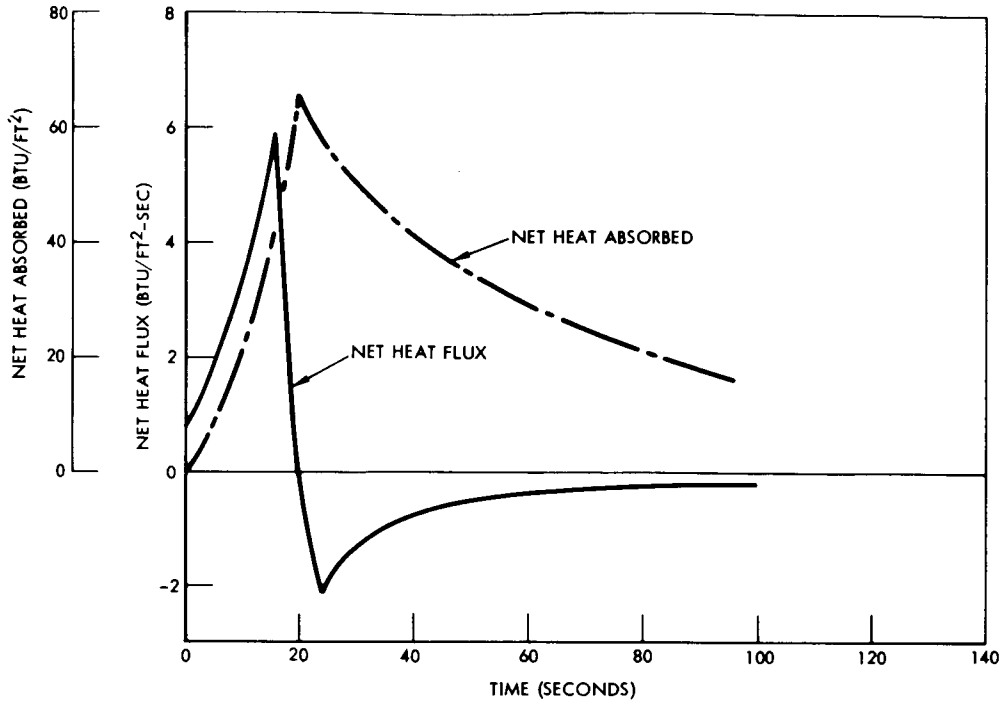

Figure 59. Transient Heating Functions at One Diameter Back From Nose

If it were necessary to design to the maximum heat flux as a steady state condition, a serious design problem would exist; however, due to the transient nature of the problem, only the surfaces reach high temperature. For the case shown, the net heat absorbed is a maximum of 66 Btu/ft^2 at 20 seconds. After 30 seconds, the net heat absorbed by the material has decreased to 50 Btu/ft^2.

The surface area of the instrument compartment fairing is approximately 1.3 square feet; thus, at the maximum point (20 seconds), a total of 88 Btu can be assumed absorbed. (This is a conservative assumption, since the compartment extends further aft and heat input decreases so that the actual Btu's absorbed will be somewhat less.) If the material were uniformly heated by this input, an average temperature rise of approximately 100 to 150 degrees would result. Distribution is, of course, not uniform and heat is also absorbed by the adjoining structure with the result that, again conservatively, the inner surface of the material will experience a rise of less than 100 degrees. The outer surface temperature is high enough so that some surface charring may take place, but no significant ablation is predicted.

In the case of the fin, a similar situation is experienced, with the net heat flux reaching a maximum value of 7.6 Btu/ft^2-sec. While surface temperatures exceed 1000 F, the midpoint within the metal does not exceed 400 F. Surface protection may be desirable and can be obtained with any of a variety of high temperature coatings such as Pittsburgh Plate Glass Company LA9708, W.P. Fuller 172-A-52, Sherwin-Williams 328-5, or Trail Chemical Company 18250.

STABILITY AND CONTROL CHARACTERISTICS

Spin Symmetry and Anomalies

In order to reduce trajectory dispersions resulting from misalignments and/or configurational asymmetries, the vehicle is forced to attain a spin rate. For combined asymmetries of realistic magnitude, analysis indicated that no appreciable degradation of the nominal trajectory would be encountered for spin rates above one revolution per second. At one revolution per second, however, a limit cycle is sustained at the spin rate frequency with an angle-of-attack amplitude equal to the steady-state trim angle. At higher spin rates, sufficiently above the pitch-yaw nutational frequency, the limit cycle is attenuated.

Although spin rates just above one cycle per second appear sufficient to provide effective minimization of dispersions due to construction asymmetries, low spin rates appear impractical. For aerodynamically attained spin, the rate is essentially proportional to vehicle velocity during boost. Because velocity increases by a factor of almost nine, a spin rate of one revolution per second at the end of boost would necessitate very low rates earlier in the trajectory. Control to the very low spin rates would be difficult; normal tolerances on fin and deflection angles could result in critical rates occurring at times that would prove objectionable. (Critical rates are those which are equal to the vehicle pitch-yaw frequency and are used to determine the criteria for spin requirements).

Spinning the vehicle for spin symmetry can precipitate dynamical problems. With the vehicle spinning, the roll rate can become equal to the pitch-yaw frequency at some time during the ascent. This problem is widely recognized, and has been investigated theoretically and experimentally. Under these conditions, resonant coupling of the pitch-roll modes will occur, and the total angle of attack will be amplified.

The vehicle stability was investigated utilizing linear perturbation theory in support of the six-degree-of-freedom study. The equations used were derived from References 8 and 9. The following assumptions were made to simplify the analysis. At any point on the vehicle trajectory, the spin rate and flight path velocity are assumed constant. This implies that any perturbations imposed on the vehicle will result in rotational displacements in the pitch and yaw planes, and translational displacements in the plane normal to the flight path. A total flow angle of attack ($\eta = i\alpha + \beta$) was defined, and the characteristic frequencies and damping of the spinning and nonspinning vehicle were obtained. The nonspinning frequency is effectively the pitch-yaw frequency of the vehicle due to its static margin. The pitch-yaw

frequency, ω_n, of the nonspinning vehicle is presented in Figure 60 for discrete points along the trajectory. Included in Figure 60 is a nominal spin rate than intersects the ω_n curve at 5 seconds. This spin rate was used to obtain the locus of roots of the spinning vehicle, Figure 61.

Resonance occurs at the point where the locus intersects the real axis. The frequencies ($j\omega$) in Figure 61 contain the rotational frequency of the spinning vehicle intrinsically, as the sum and difference of the pitch-yaw and spin frequency

$$j\omega = j\,(\omega_n \pm p)$$

This does not imply that the vehicle stiffness (resilience) is appreciably affected by the spin. The ability of the system to resist torques, above and below resonance, is still described by the nonspinning pitch-yaw frequency of Figure 60. The frequencies in Figure 61 are the two model frequencies that describe the motion of the total angle of attack.

The roll rate shown in Figure 60 was chosen since, for reasonable aerodynamic spin forcing methods, it provides the least amplification in the total angle of attack during resonance. This can be seen from the steady-state solution to the linear equations (Reference 9). The amplification during resonance is approximated by

$$|A| = \frac{1}{2\zeta}$$

where ζ is the damping ratio.

A plot of this steady-state amplification ratio is presented in Figure 62 for resonance occurring at various points on the trajectory. The reference points shown on Figure 62 are the peak amplitude ratios obtained from the six-degree-of-freedom trajectory simulations. Build-up to the peak values for forced resonance at several points along the nominal trajectory is shown in Figure 63. Although true steady-state conditions are naturally not achieved in the dynamic simulation program, good agreement with the theoretical analysis was obtained up to approximately 20 seconds. Beyond this time, vehicle response becomes relatively slow and thus lags the steady state predictions.

As an additional check, vehicle response to roll inputs was compared to a second-order system of similar characteristics. The check was made for conditions existing at 16 seconds after launch and the comparison is shown in Figure 64. Although the vehicle is obviously not a linear second-order system, and is accelerating and not at a steady-state condition, the data points shown in Figure 64 yield good agreement with the theoretical analysis.

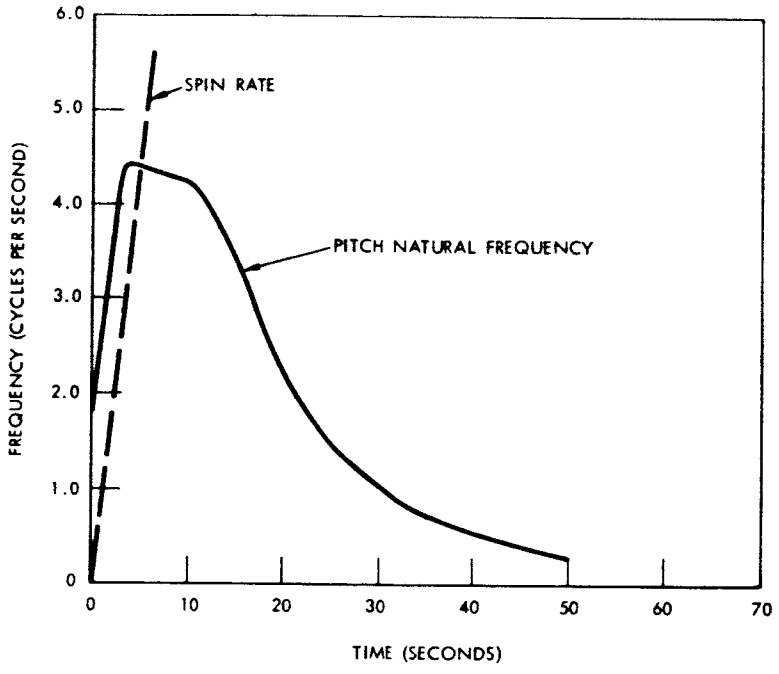

Figure 60. Nutational Frequency of the Nonspinning Vehicle

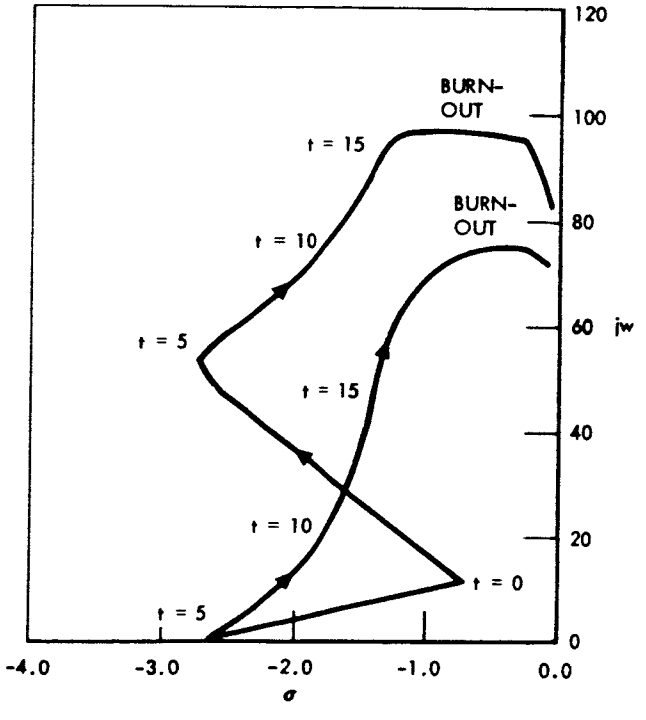

Figure 61. Root Locus

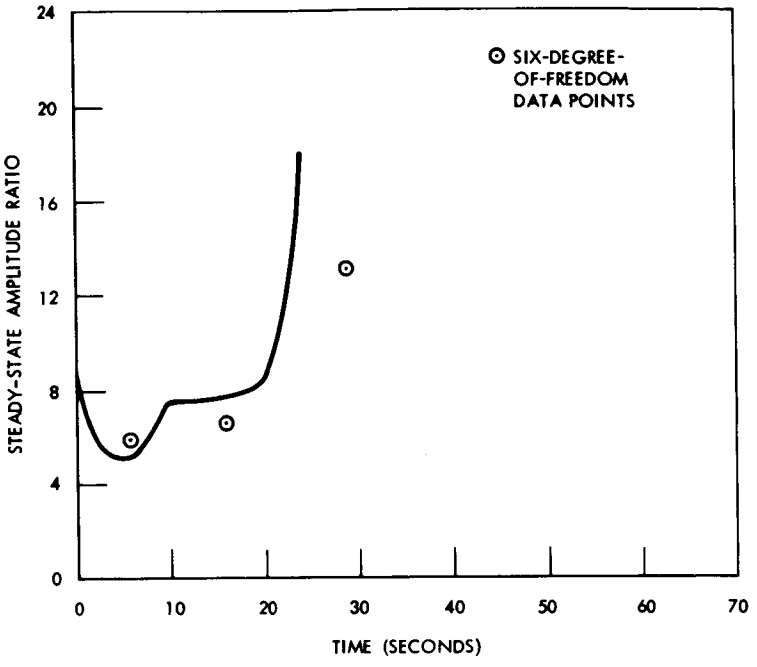

Figure 62. Steady-State Amplitude Ratio During Resonance

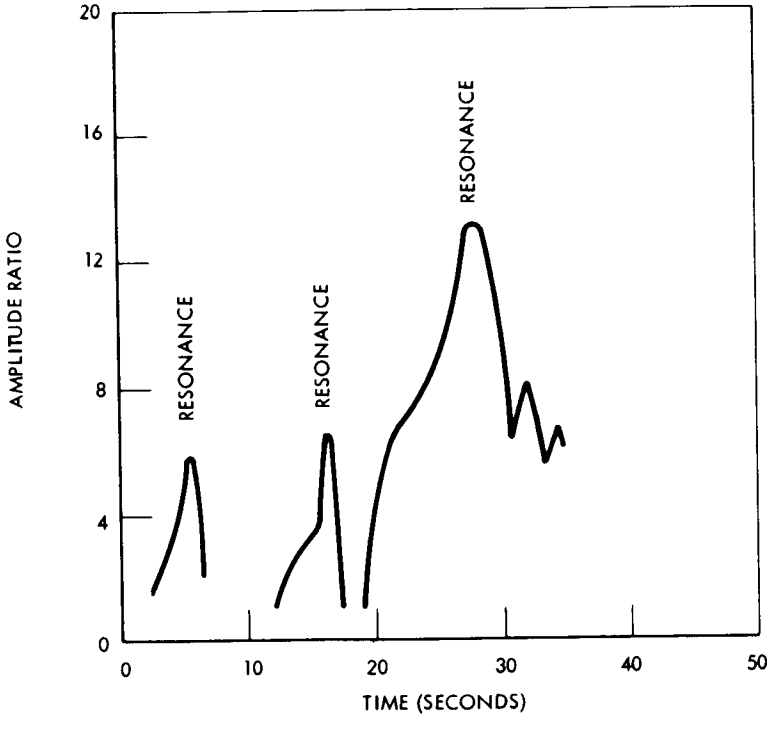

Figure 63. Amplitude Ratio for Resonance at Three Different Times

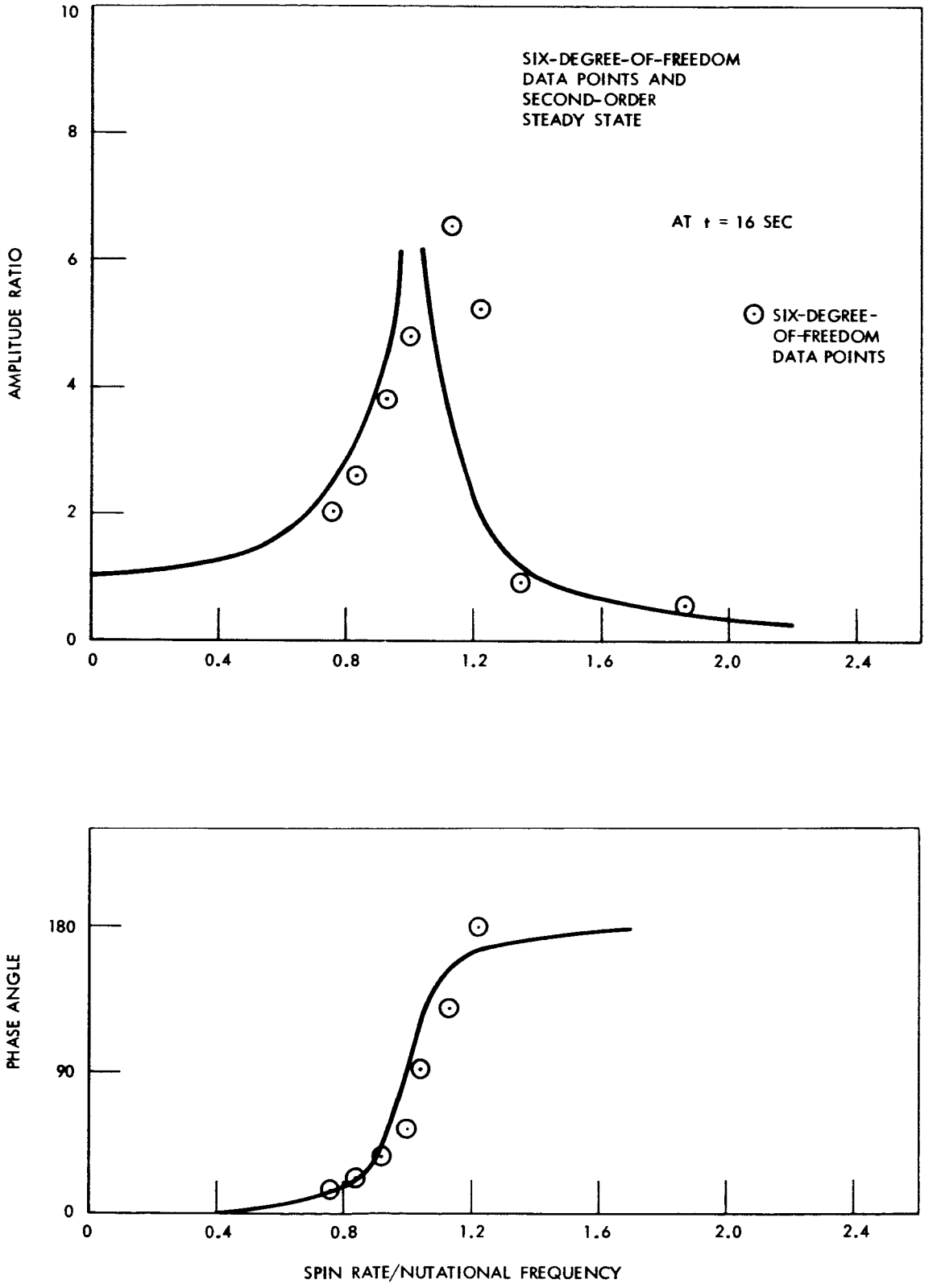

Figure 64. Amplitude Ratio and Phase Angle

Typical vehicle responses during the resonance phenomena are presented in Figures 65 and 66. Major resonance conditions are noted at 5.5 seconds following launch. This compares favorably with the predictions afforded by Figures 60 and 61.

The characteristic frequencies predicted by the root locus shown in Figure 61 may be observed by examining the angle-of-attack history (Figure 66). Resonance effects start to occur at about 1.5 seconds, when the pitch-yaw frequency reduces to high- and low-frequency components. The higher component damps fairly rapidly due to its higher damping ratio, but the low-frequency component degenerates to zero or a neutral condition. The resulting divergence is only resisted by the net system damping which happens to be a maximum at this point. The total angle of attack (or incidence angle) is an absolute value, so that scales above and below the time axis were chosen for convenience in portraying the nature of the oscillations.

Pitch attitude, which is not a direct function of spin rate (although forced by it through the vehicle response) continues to oscillate at the pitch-yaw frequency but with increasing amplitude until the resonance point is passed.

The problem of resonance cannot be solved by spinning at lower rates and thus encountering resonance at higher altitudes. From Figures 62 and 63, the peak amplitude is lowest around 5 seconds. While at much later times (post burn-out), the load per degree would be less, the angle can become quite large and lead to possible instabilities because of nonlinear effects.

One potential solution to the resonance problem is the pre-spin of the vehicle with vanes extended in the exhaust wake, thus removing the dependence on the vehicle velocity build-up.

The estimated spin rate obtained with 12 vanes set at a seven-degree incidence angle is shown in Figure 67. The vanes are designed to start burning off at one second and to be completely off at four seconds. Their small size and short duration prevents any significant thrust loss while the redundant number provides attainment of the desired spin characteristics under possible uneven ablation or breakage of single vanes. The highest torque required during the first second is only 4.4 foot-pounds.

Because the roll damping of the vehicle is low, misalignment of the ring support struts could affect the attained spin rate. The helix angle corresponding to the spin rate of Figure 67 is shown in Figure 68. Because strut angle misalignments on the order of 0.25 degrees are possible, the spin rate may vary as much as ±5 revolutions per second at times beyond

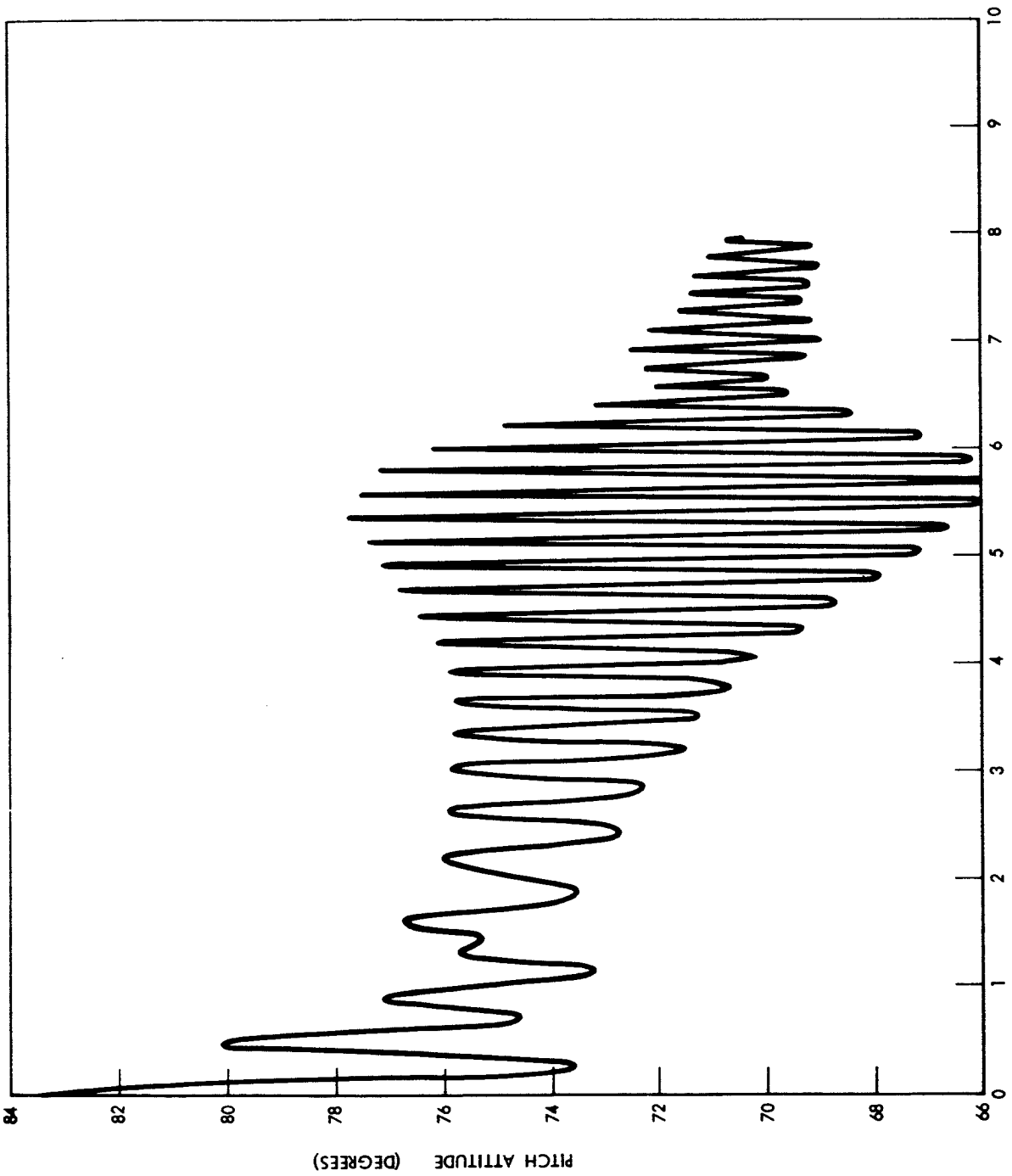

Figure 65. Pitch Response Through Resonance

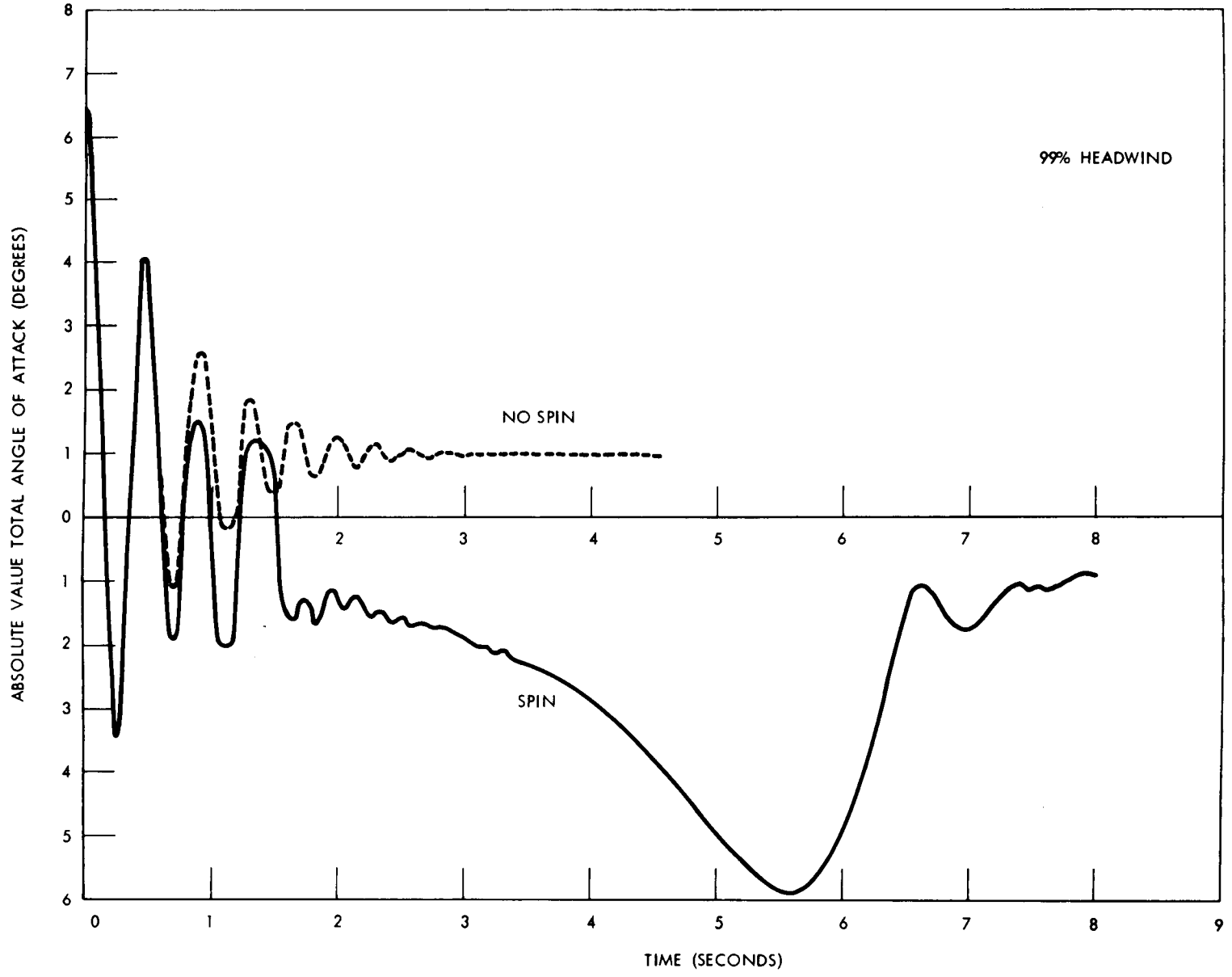

Figure 66. Total Incidence Angle Through Resonance for One Degree Steady-State Trim

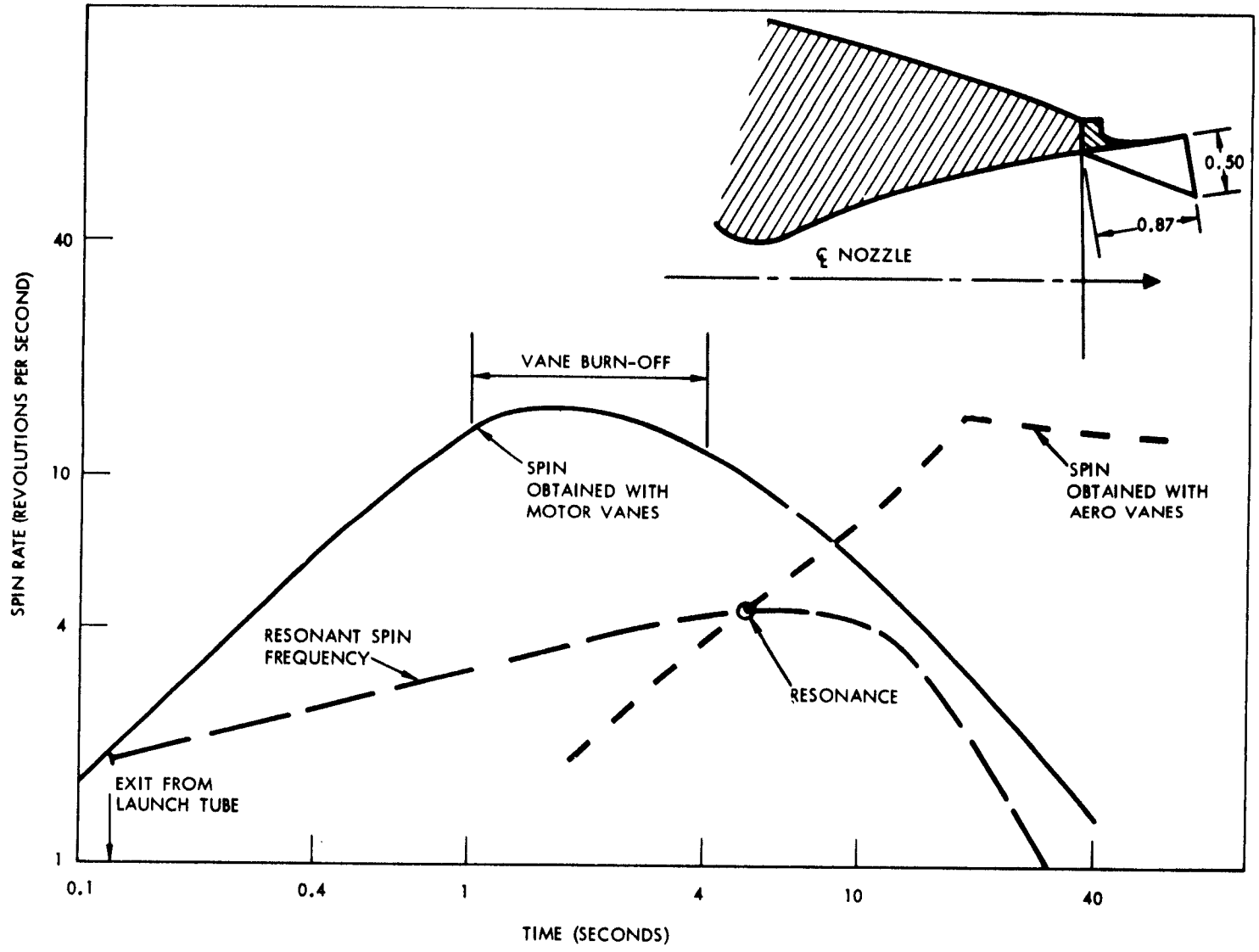

Figure 67. Spin-Forcing Methods

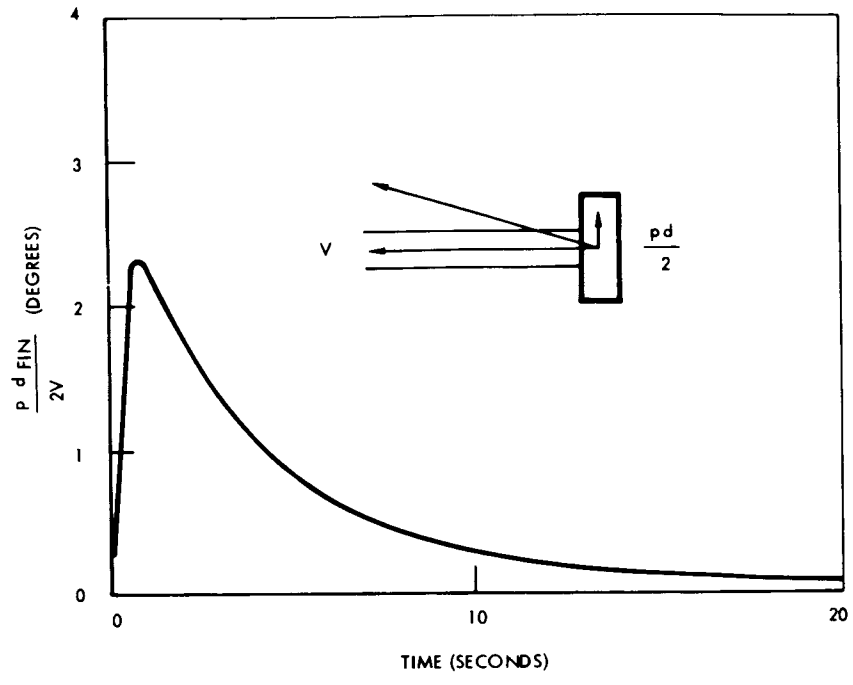

Figure 68. Helix Angle of Ring-Spin With Motor Vanes

10 seconds. It may be necessary to design the spin vanes to stay on for several more seconds to ensure retention of a higher than critical spin rate.

The use of conventional aerodynamic surfaces to provide spin makes it necessary to pass through the pitch-roll resonance as previously discussed and also indicated in Figure 67. The example shown uses ring support struts twisted to produce an angle of 0.53 degrees at the ring junction. A like effect could be obtained with struts of zero incidence and small tabs, in the manner of Reference 10.

The nominal resonance conditions attained with the conventional aerodynamic-induced spin can (when coupled with worse-case accumulations of tolerances that result in a one-degree trim requirement) produce short-term angles of attack approaching six degrees. Structural and aerodynamic integrity of the vehicle is adequately maintained under these conditions; however, as previously discussed, a slow spin that results in resonance at a latter point is an area of major concern. Angles of attack in excess of approximately ten degrees may result in reaching a region of nonlinear aerodynamics and attendent stability problems. While wind-tunnel testing is required to confirm this, the potential severity of the results leads to recommended incorporation of a combined exhaust vane-aerodynamic spin forcing system. The combined method provides spin rates that avoid the resonance regions during the earlier portion of flight without necessitating sustained spin rates that would be higher than desired as apogee conditions are reached.

Rapid Dynamic Pressure Decay

For a conservative system, any out-of-trim condition at or near the peak pitch-yaw frequency will increase in amplitude as the dynamic pressure decreases. The amplitude increases to maintain an energy balance as the pitch-yaw frequency decreases. A system with finite damping will retard the amplitude build-up, but there will be an effective reduction in the time to damp.

Outside of the neighborhood of resonance, analysis has indicated that this effect is not a problem of concern here. A check of nontrim conditions at 19 seconds after launch (just at burn-out) indicated that the resulting motion damped with only a small increase in damping time.

Forced resonance at 28 seconds took place under the influence of rapid dynamic pressure decay and an increase in amplitude ratio is shown in Figure 63. While it is not possible to separate the exact contribution of the dynamic pressure decay from all other factors involved in the amplitude build-up, damping is an all-important term and any reduction in damping will be reflected by an increase in amplitude.

High-Altitude Conditions

At high altitudes the pitch-yaw frequency becomes quite small due to the low air density. Under these conditions, the gyroscopic stability associated with the spin becomes a significant part of the total vehicle stability. Figure 69 presents the relative magnitudes of the nonspinning aerodynamic pitch-yaw frequency and the combined gyroscopic-aerodynamic frequencies of the spinning vehicle at high altitudes. For a nonspinning, aerodynamically stable vehicle, a gravity turn is performed with the vehicle aligned to the flight path. With the inclusion of spin, gyroscopic torques result, causing a precession of the vehicle with respect to the flight path. It was found, from the trajectory simulation studies, that the amplitude of precession was negligible.

MAGNUS INSTABILITY

The cross-flow over the cylindrical rocket body, coupled with body blockage of the fins at angles of attack can cause destabilizing moments on the vehicle, Reference 11. The Magnus moments act normal to the plane of the total angle of attack, and thus can only be resisted by damping.

Criteria for stability with Magnus moment present was estimated from the data of Reference 11 and is shown in Figure 70. The upper curve establishes

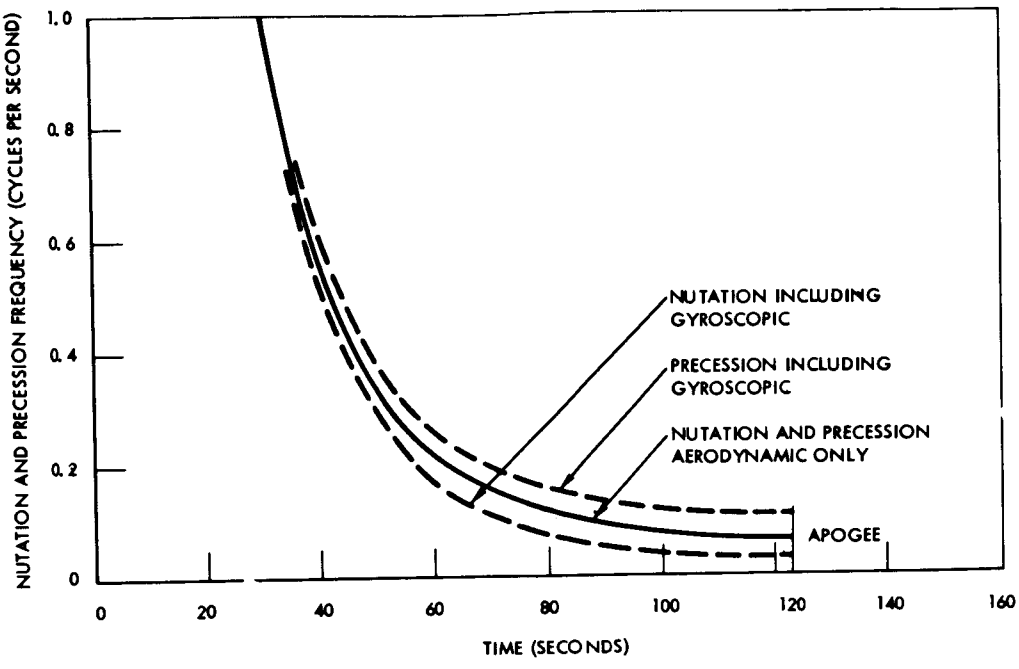

Figure 69. Spin Contribution to Nutational Precessional Frequencies at High Altitudes

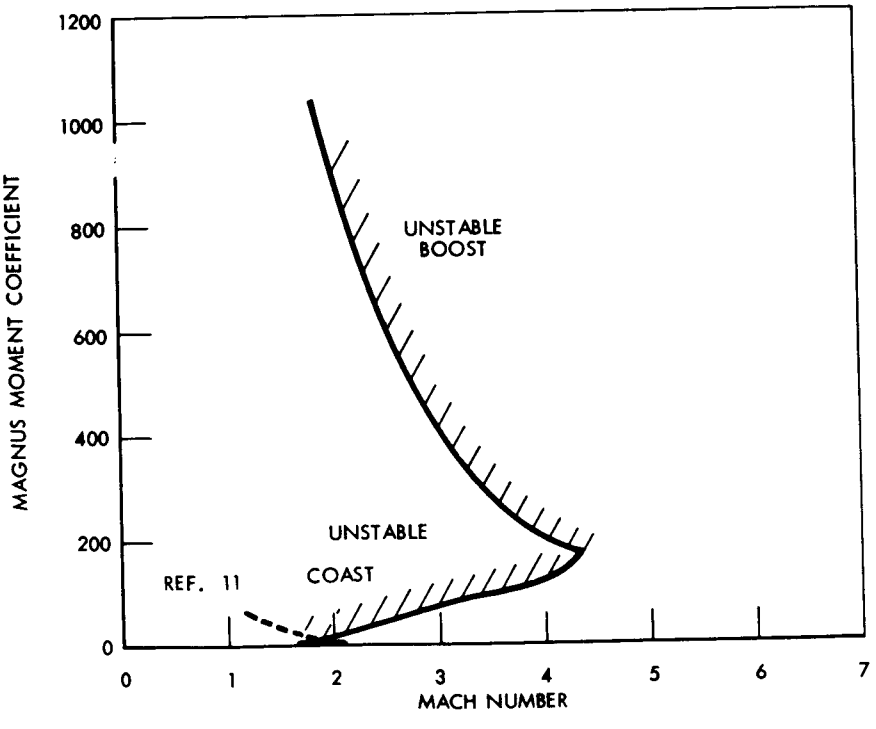

Figure 70. Critical Magnus Moment Coefficient

the maximum value of Magnus moment coefficient up to burn-out; the lower curve presents the boundary from burn-out to apogee. Because of the numerous variables associated with this phenomena, no satisfactory method was found to determine the actual coefficients without empirical data. Typical values, based on Reference 11, are plotted in Figure 70 for comparison purposes. Although this would indicate a region of concern around 60 kilometers, a check of the probable time constant associated with the instability indicated a value in excess of 200 seconds. A time constant of this magnitude should not present a problem; however, testing is required to define more fully the possible Magnus effect.

TRAJECTORY CHARACTERISTICS

Nominal trajectory characteristics of the vehicle have been presented in Figures 17 through 21 and are also shown, in English units, in Figures 71 and 72 and in metric units in Figures 73 and 74. Other items of particular interest are discussed in the following paragraphs.

Launch Velocity Variations

The nominal launch velocity required to achieve the desired apogee band under the severe headwind environment and within launch angle restrictions has been established as 500 feet per second. Altitude variations with both launch velocity and launch angle are shown in Figures 75 and 76 for the head and tailwind 50- and 99-percent profiles. As shown in Figure 75, a launch velocity of 400 feet per second could be allowed when considering only the 50-percent profile; however, it is not sufficient to meet altitude requirements under the extreme conditions. While a variable launch speed system does not appear attractive from a complexity standpoint, the data of Figures 75 and 76 may be used as the basis for future trade-offs in the establishment of wind requirements versus initial acceleration and launcher subsystem requirements.

Altitude Versus Time

The device chosen for initiation of the payload separation/expulsion sequence previously discussed is a fuze and therefore time sensitive. Time to altitude under the varying launch conditions thus becomes important. Figure 77 presents the altitude attained at 124 seconds—the nominal initiation time chosen Evaluation of end conditions indicated that a variation of at least ±2 seconds could be tolerated.

Spin Rate/At Apogee

Parachute deployment problems could be pronounced if the spin rate of the vehicle is excessive. A limit rate of 10 revolutions per second was

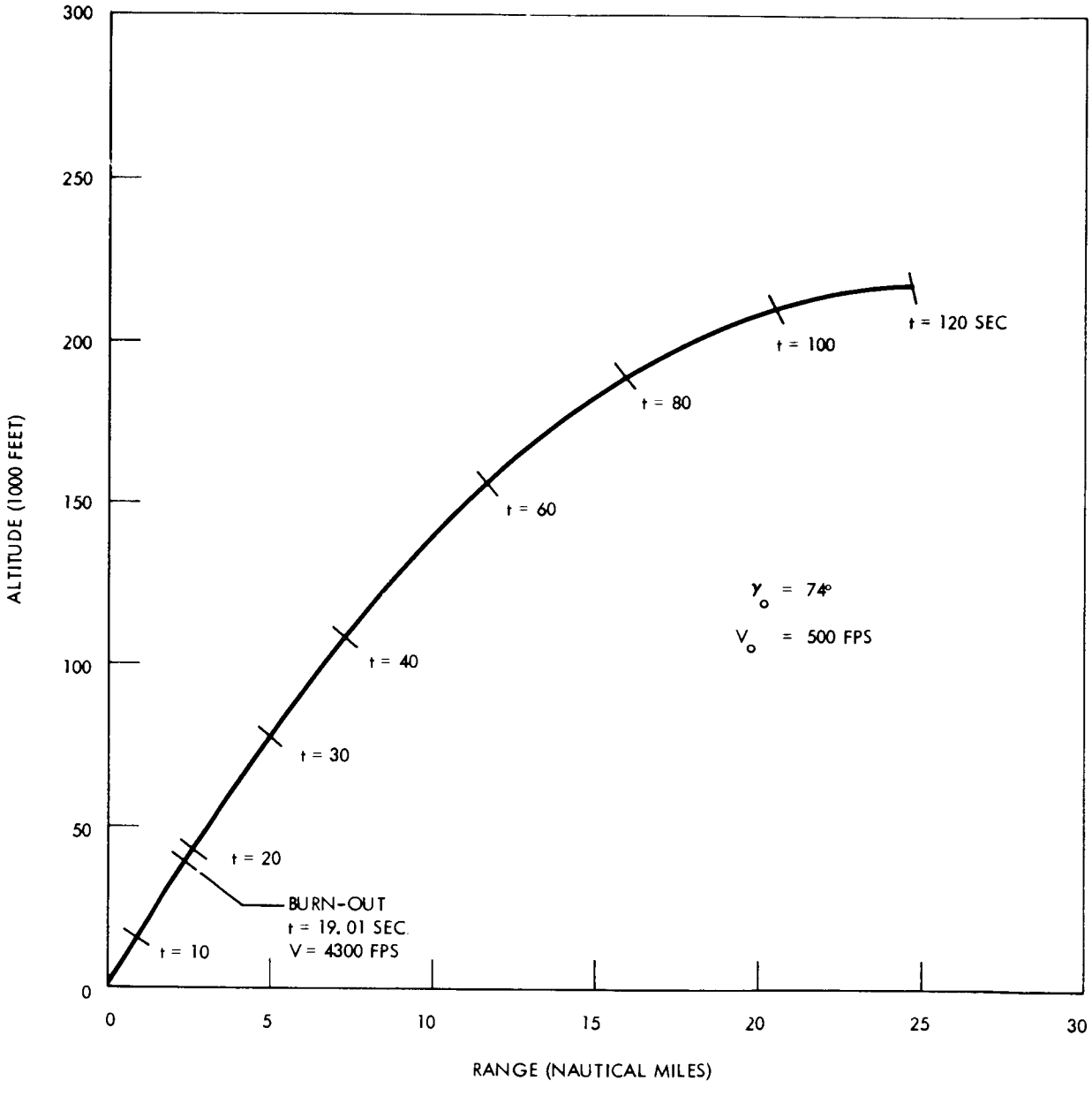

Figure 71. Nominal Performance Trajectory—No Wind, English Units

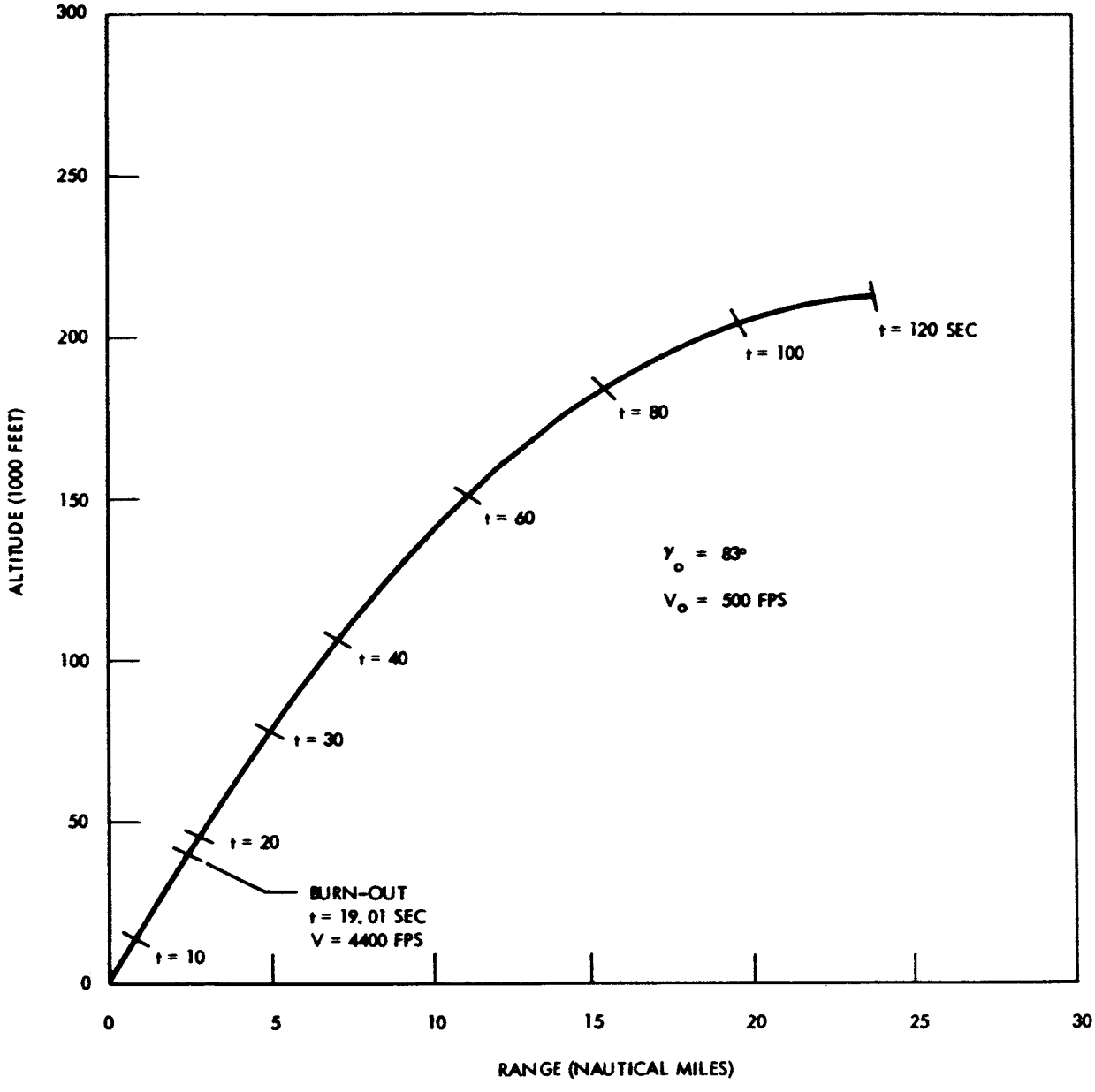

Figure 72. Nominal Performance Trajectory—99 Percent Headwind, English Units

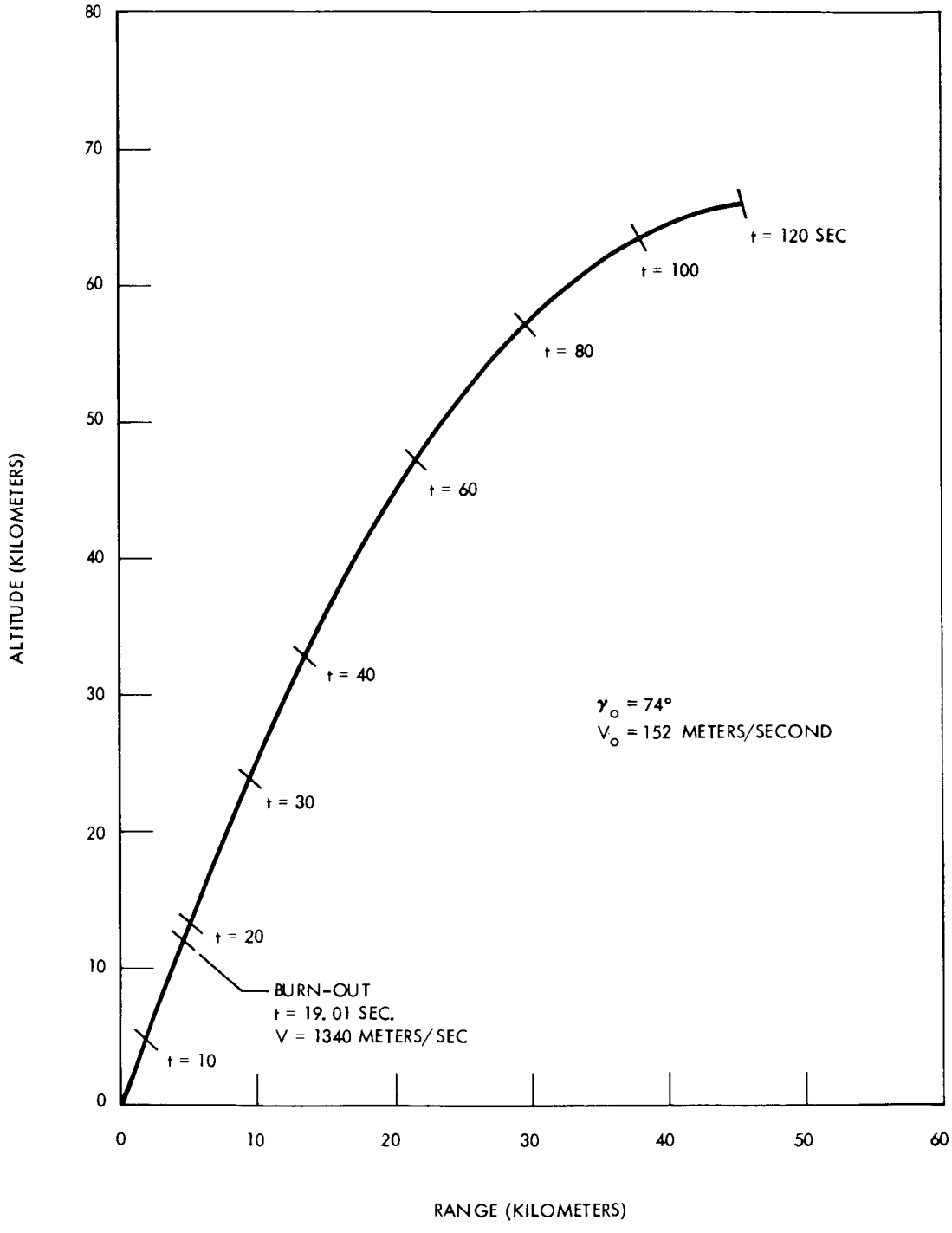

Figure 73. Nominal Performance Trajectory—No Wind, Metric Units

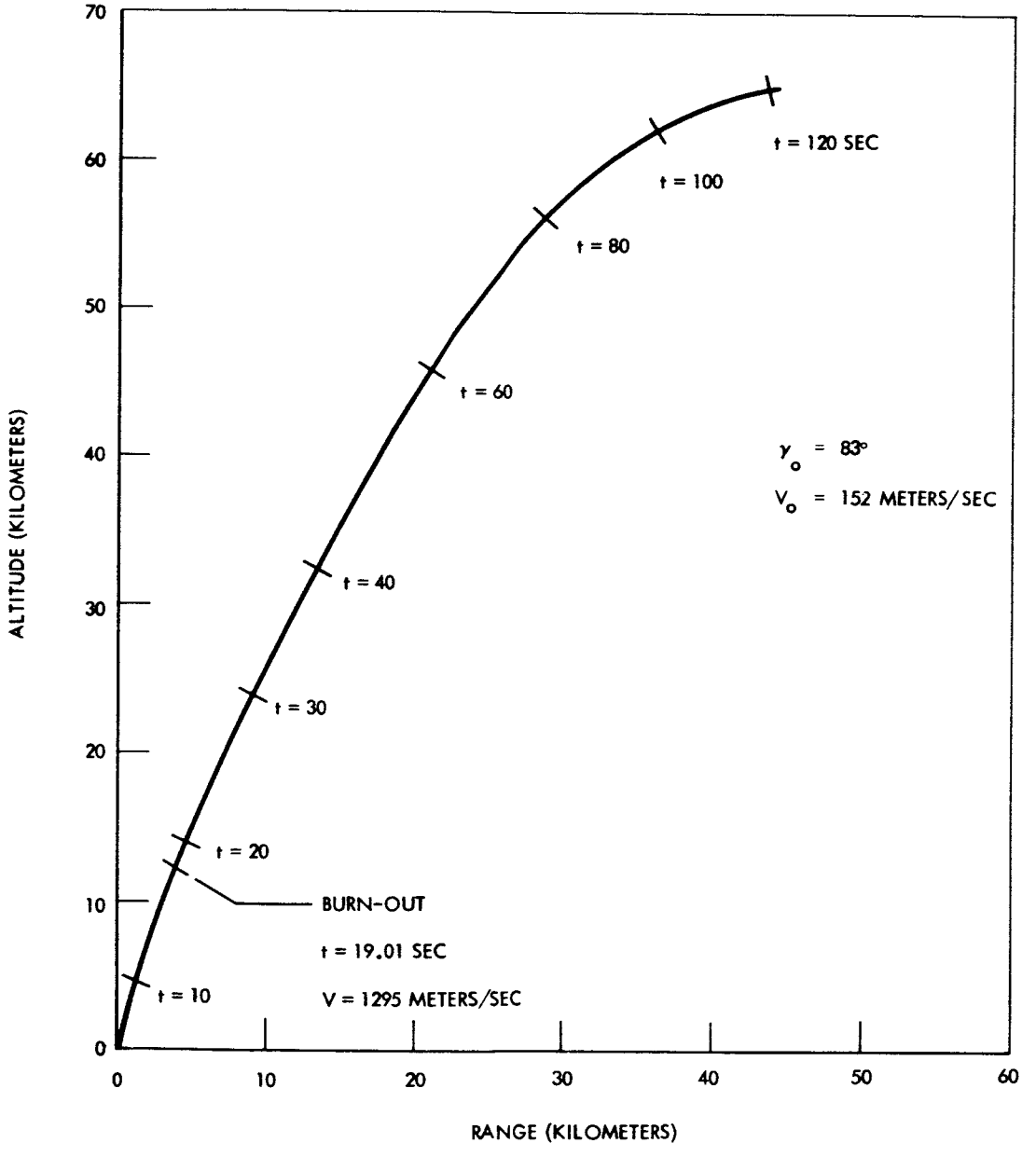

Figure 74. Nominal Performance Trajectory —99 Percent Headwind, Metric Units

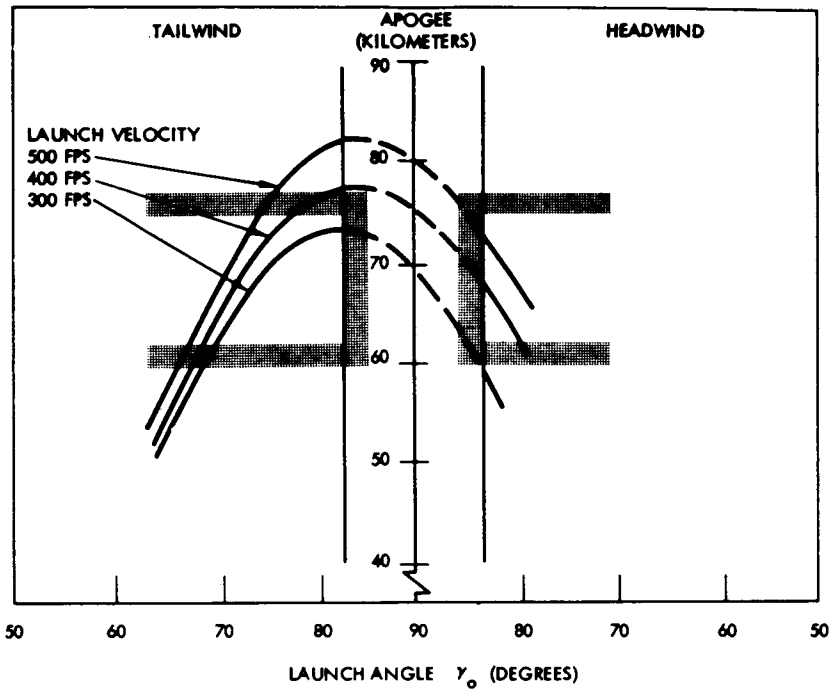

Figure 75. Effect of Launch Velocity — 50 Percent Profile Wind

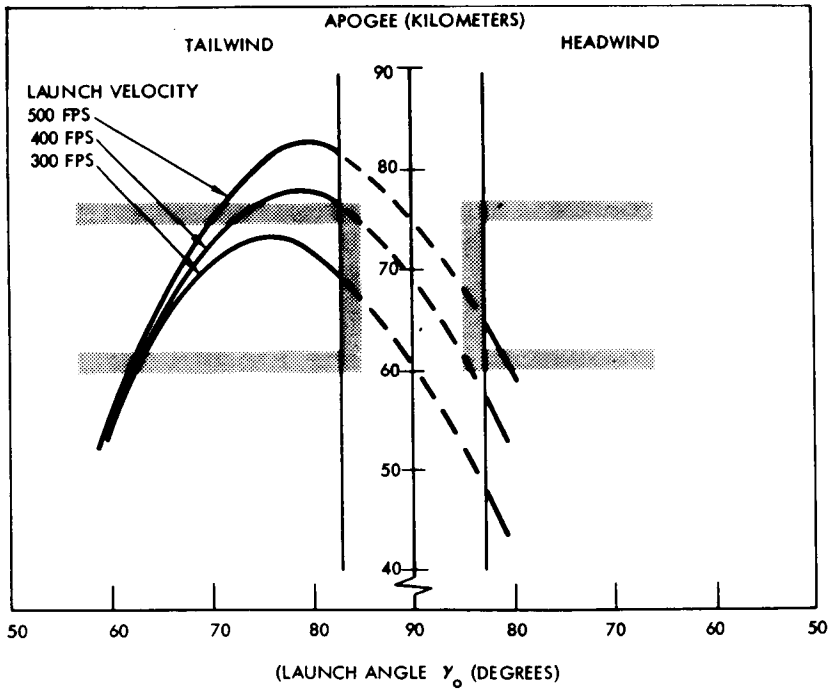

Figure 76. Effect of Launch Velocity — 99 Percent Profile Wind

selected as the design objective. The nominal spin history (for aerodynamically induced spin) obtained from trajectory simulations is shown in Figure 78. As indicated, the design objective is fairly well met in the nominal case. However, tolerance build-ups may induce variations of as much as ±5 revolutions per second about the case shown.

Payload Weight Variation

The functional payload is represented by the AN/DMQ-9 radiosonde plus the parachute system and base plate assembly. The estimated weight of this combination is 9.9 pounds and represents approximately 14 percent of the launch gross weight. Specific payload designs may result in some variations about this nominal value; thus, the effect of weight changes on attained apogee is of interest. Trajectory studies have shown the variation in apogee to be essentially linear with structural weight for variations within five pounds of nominal and to be represented by a trade-off factor of 7860 feet or 2.4 kilometers per pound. For example, the nominal system, when launched at an angle of 80 degrees in a 50 percent headwind environment, attains an apogee of 68 kilometers. If structural weight were increased by 3 pounds, an apogee of approximately 61 kilometers is predicted.

Dispersion and Wind Weighting

Two major classes of dispersion are of interest: (1) the variation in apogee altitude and range under varying conditions, and (2) the impact dispersions associated with either the expended booster case or, in the case of a separation malfunction, the impact zone of the total vehicle.

Figures 79 and 80 present apogee altitude and range at apogee for the 50-percent and 99-percent wind profiles at various angles with respect to the launch direction and for various launch elevation angles. For the 50-percent profile, and launcher elevation angle varied as a function of wind, absolute range at apogee dispersions fall within a 10-nautical-mile band. Under the influence of the 99-percent profile, a maximum apogee range band of 17 nautical miles is noted. As used in Figures 79 and 80, a 45-degree sidewind is one which quarters from the headwind position and a 135-degree sidewind is one which quarters from the rear.

As an example of the use of these plots in establishing launcher elevation angle, consider the case of a 90-degree (direct lateral) wind which matches the 50-percent wind profile. If a fixed angle of 80 degrees were used, apogee would very slightly exceed the desired tolerance band and would occur approximately 19 nautical miles from the launch site. If, however, the launch angle were reduced to 72 degrees, the design apogee of 65 kilometers would be attained. The decreased elevation angle results in an increase in range to apogee of 9.5 nautical miles over the 80-degree launch case or a total range of 28.5 nautical miles.

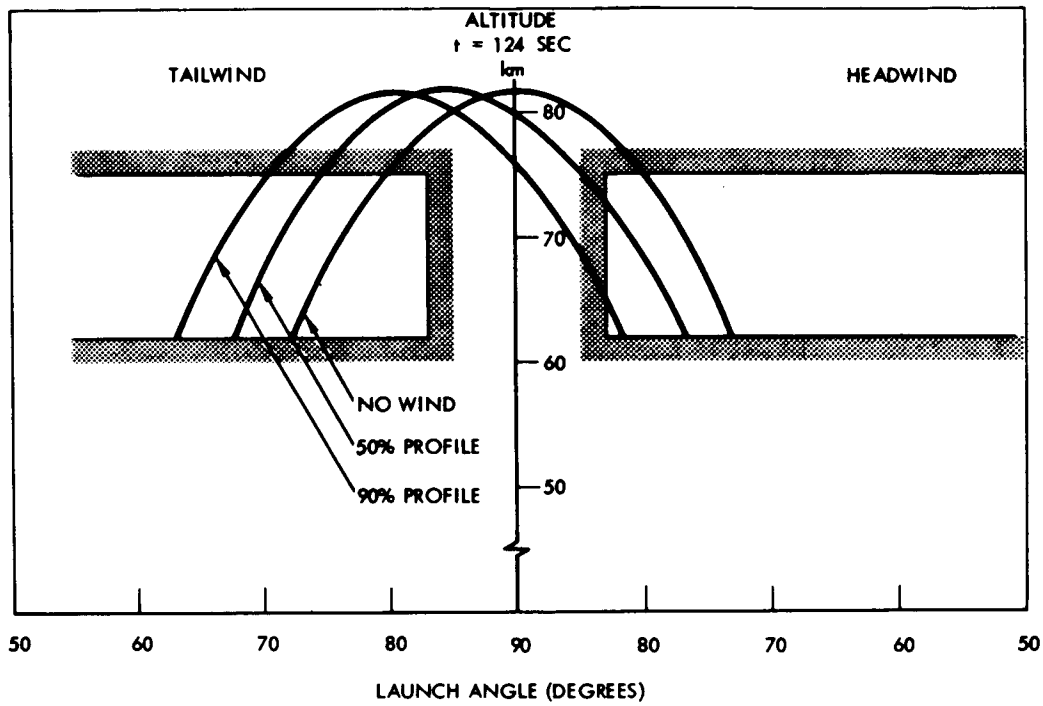

Figure 77. Altitude at 124 Seconds

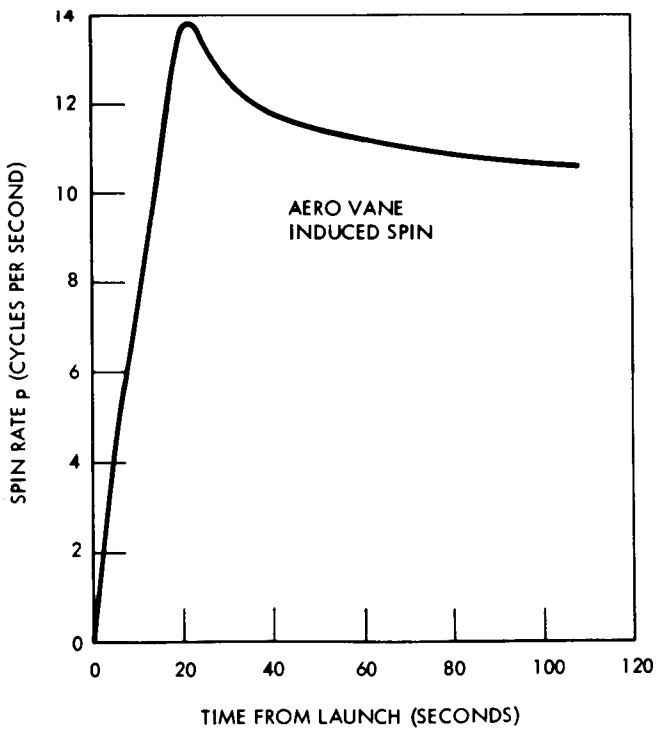

Figure 78. Nominal Spin Rate History

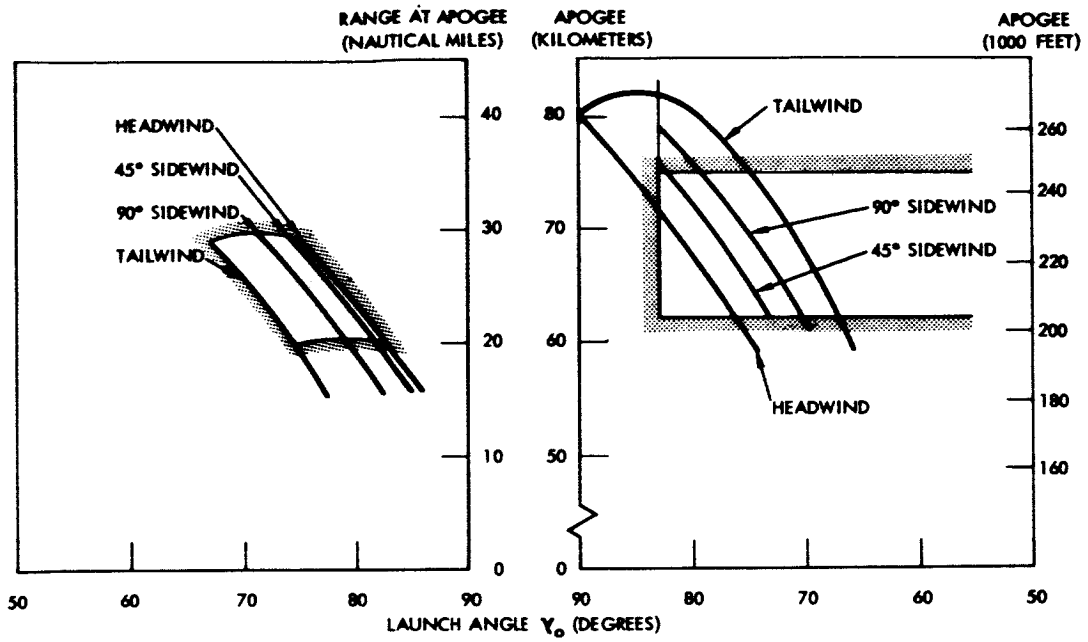

Figure 79. Apogee and Range Dispersion— 50 Percent Wind Profile

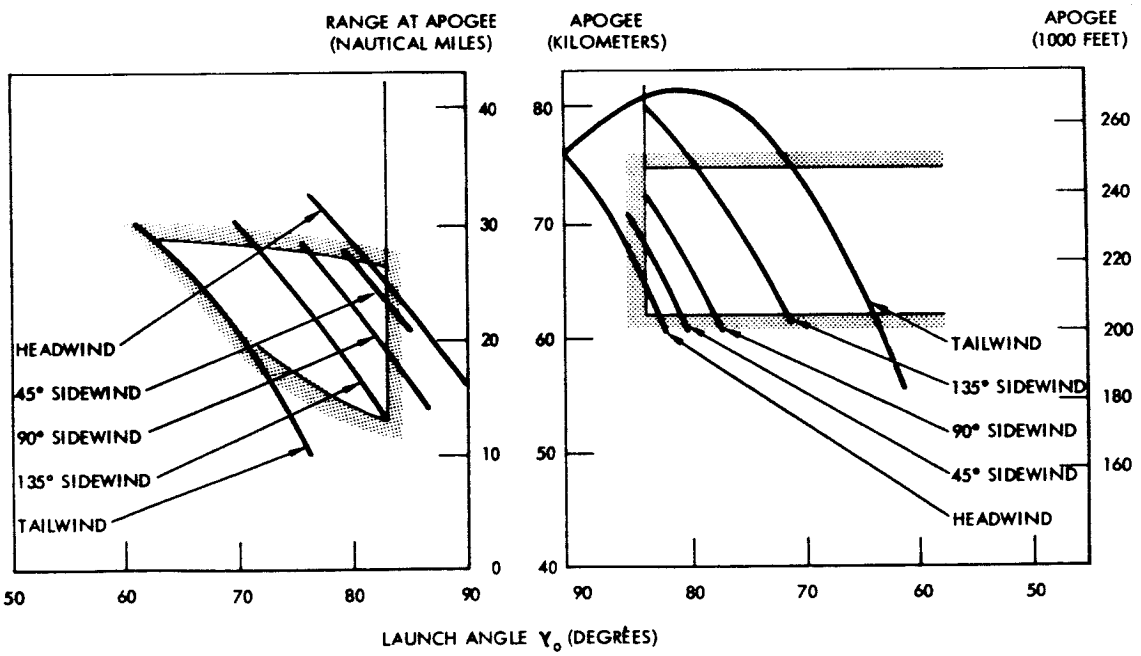

Figure 80. Apogee and Range Dispersion—99 Percent Wind Profile

Impact dispersions associated with the wind-weighted launches of Figures 79 and 80 are shown in Figures 81 and 82. In the event of a separation failure, the payload-booster combination will, on a considered 3-sigma basis, impact within the boundaries labeled "separation failure."

For normal operation, the expended motor case will impact within the hatched area designated "Dispensed Motor Case."

In order to consider the boundaries as 3-sigma variations, expected deviations in aerodynamics and sequence initiation were accounted for. Because the expended case is expected to be an unstable body, a considerably wide range of effective drags were used in compiling the dispersion area. These values ranged from an effective $C_D = 2$ to an upper limit of $C_D = 14$.

This system of wind weighting (briefly outlined for the specific wind profiles and directions noted) can be expanded to include other wind conditions and azimuth variations. The families of apogee altitude and range at apogee (which could be presented as down-range versus cross-range) would then provide a rapid and convenient catalogue for the field operator. Wind profiles, obtained from balloon soundings prior to rocket launch, would be compared on a surface speed and slope basis for fast indexing. Indications are that the average slope up to approximately 40,000 feet is sufficient for field use.

LAUNCHER SUBSYSTEM DESIGN

Launching in the surface wind environment established for this study has indicated the requirement for attaining a relatively high velocity prior to the time that the vehicle becomes free to respond to disturbances. To provide this initial acceleration without paying the penalty associated with the addition of propellant to the basic vehicle, the concept of a closed breech-tube launcher with an auxiliary booster charge, ignited by the vehicle motor, was investigated.

The preliminary design of a potential launcher system is shown in Figure 83. The launch tube is supported by four cables. Two opposite cables are of fixed length to keep the tube perpendicular in one plane, while the other two cables are winched to the desired elevation. Azimuth control is obtained by rotating the tube-cable assembly.

Maximum cable load occurs during erection of the tube following vehicle loading and manual assistance appears to be required until the tube is raised high enough to alleviate the acute angle geometry of the raising winch. Two men are needed to lift the tube and a third is needed to operate the winch. Cable tension (and winch load) will not exceed 500 pounds if the point of cable attachment to the tube is raised manually 8 feet above the base.

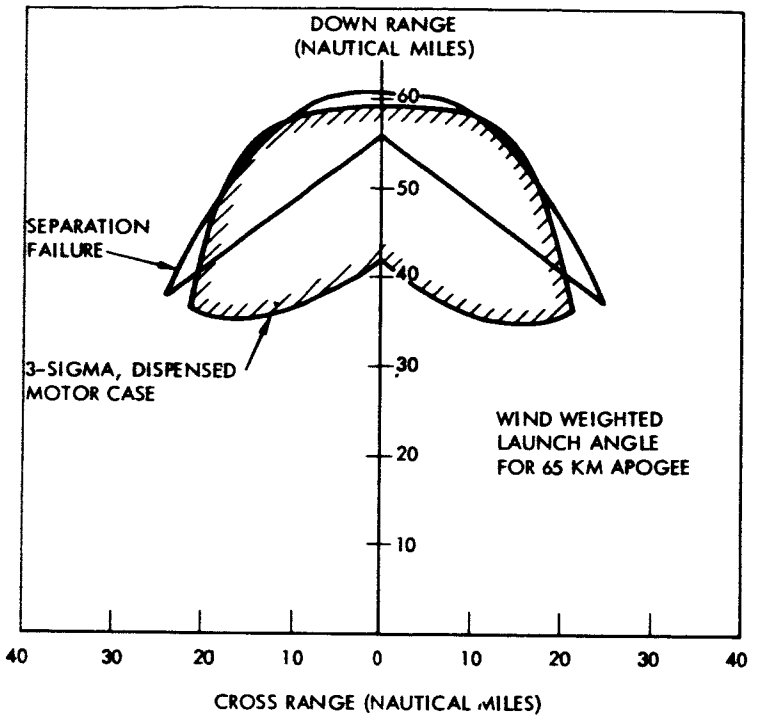

Figure 81. Ground Impact Dispersion—50 Percent Wind Profile

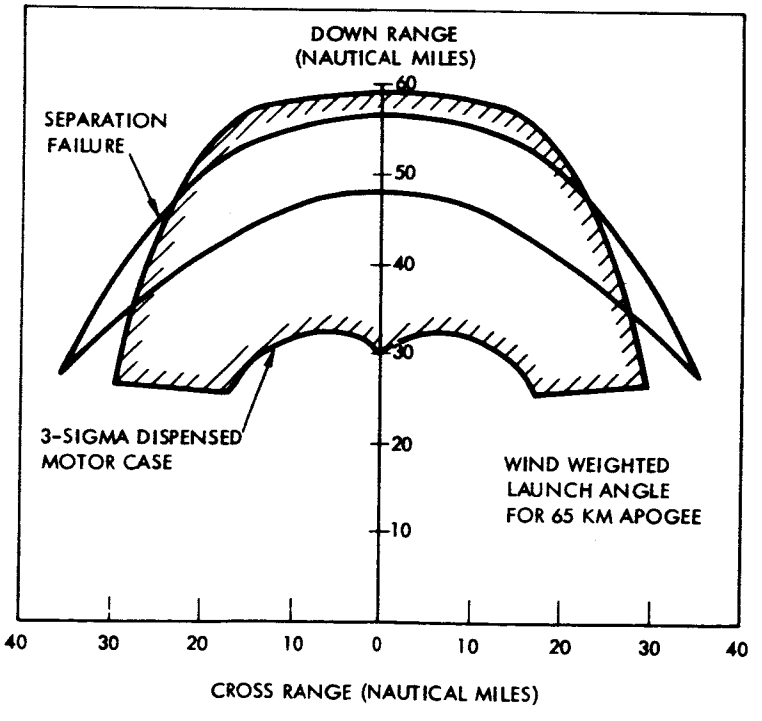

Figure 82. Ground Impact Dispersion—99 Percent Wind Profile

Because launch capability in high-surface-wind environment is required, a maximum design wind velocity of 100 feet per second was used for check purposes. Analysis indicates that the tube drag will be approximately 84 pounds and cable drag approximately 7 pounds. Maximum cable load will occur at the assumed lower operational elevation limit of 60 degrees. In this case, one cable must bear the loaded tube weight plus the drag load—totaling approximately 380 pounds. To provide adequate safety factors, 1/8-inch steel aircraft cable is used.

Four support legs, at a radius of 100 inches, prevent overturning due to wind loads in velocities up to 113 feet per second. Additional support points, ballasting, or tie down will be required for higher wind velocities.

Launch recoil produces relatively high instantaneous loads. The estimated peak load is 17,000 pounds, with an average over the 0.16 second launch period of 9000 pounds. Firing at 60 degrees elevation will produce side loads of one-half these values. Staking of the base to the ground is recommended.

From a general structural point of view, the launch tube must withstand internal pressure, bending and shear loads due to dead weight and dynamic pressures induced by winds, axial loads (most critical at erection) which tend to cause column instability, and indentation due to handling or misuse. The wall of the launch structure may be designed in two ways:

1. Thick wall construction, in which the wall performs all of the above structural tasks

2. Thin wall construction, with accompanying longitudinal and circumferential stiffeners, in which the wall resists the internal pressure, the stiffeners maintain stability and provide bending and shear resistance, and an auxiliary thin outer skin is added to deter penetration and indentation

The thick-wall method chosen, and shown in Figure 83, appears to be the most attractive from overall fabrication and structural considerations.

The joints must maintain the structural integrity and provide an effective pressure seal. They must be easily assembled and disassembled and must provide a means for bringing the axis of each section into collinear alignment.

The estimated weight of the assembled launcher (less vehicle) is 428 pounds, with a maximum single component weight of approximately 60 pounds.

Drawing No. 7444-2

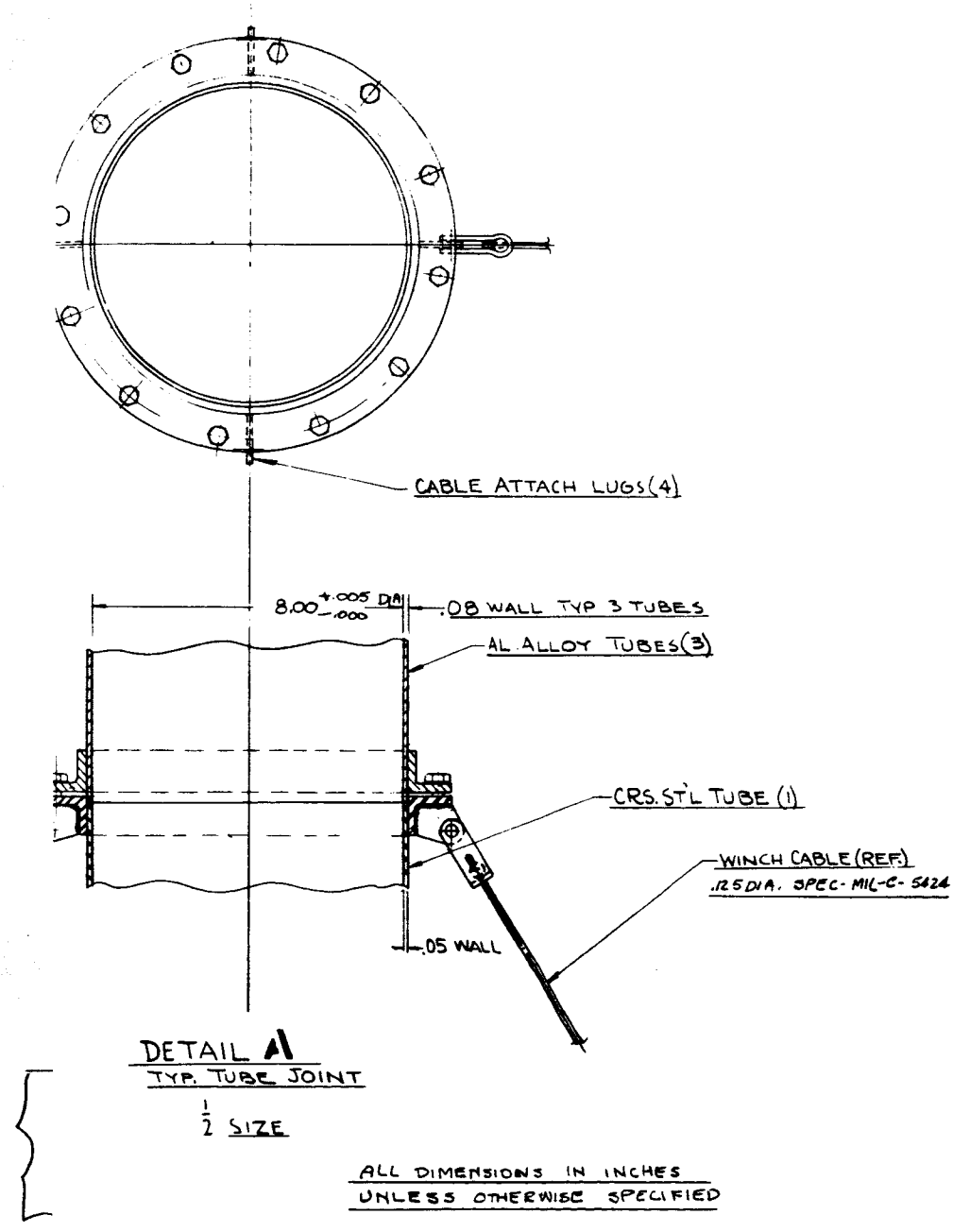

Figure 83. Launcher Configuration

Auxiliary Booster Charge

The auxiliary booster charge evolved for use with the tube launcher utilizes a standard propellant cast to compatible diameter and perforated with holes to obtain the necessary surface area for rapid burn rate. Actual grain burning rate is thus not critical and normal propellant compositions appear practical for use. For the design case, a 14.65-percent perforated grain was used, resulting in a casting with 600 holes of 0.125-inch diameter.

A peak tube pressure of approximately 300 psig (due to the combined auxiliary propellant and main motor exhaust effects) occurs at 0.02 seconds after auxiliary charge ignition and is obtained with a charge weight of 1.75 pounds. Leakage, wall friction, and heat losses of about 10 percent appear realistic and are accounted for in the selection of charge weight.

Average pressure over the 0.16-second launch interval is approximately 150 psig, with an average vehicle acceleration of approximately 106 g's noted. Although relatively high by current sounding rocket standards, payload developments and the trend toward solid-state component design appears to make this a realistic value. The shorter term transients, producing 170 to 180 g's over an interval of about 0.04 second, are not expected to create an insurmountable problem. (It has been estimated by some using agency personnel with considerable experience in field use of various sounding rockets that current payloads have experienced loadings in excess of 200 g's during late parachute deployment without damage to sensors and telemetry.) Tube-length changes or modification of the breech assembly to incorporate a plenum chamber could be made in the event that initial tests indicate a need for reduction in acceleration level. It also might be noted that propellant grains and telemetry systems have been successfully subjected to much higher acceleration environments during various gun-launch test programs. The expected problem area for sounding rocket application appears to be the end instrument mounting method, which should be amenable to simple design changes.

CONCLUSIONS AND RECOMMENDATIONS

The end-burning single-stage system concept, with the payload separated at apogee or near apogee conditions, is capable of meeting the design objectives delineated for this study. Under the established ground rules, and at this point, it must be judged the most optimum of the approaches considered.

The dual-thrust level motor is recognized as an exceedingly strong contender, and as additional developmental and operational experience with this type of propulsion system is acquired, it could attain lead position in the overall relative rankings.

The two-stage system, while capable of excellent performance, is ranked lower in reliability and cost aspects. The single propulsive stage system with a stabilized payload section separated at burn-out ranks fourth when all assessment aspects are considered.

Certain specialized areas of detailed analysis and design, which are commensurate with attaining a second level in the orderly development of the meteorological sounding rocket system, have been noted and include:

1. Additional investigation of possible Magnus instability effects at near apogee conditions. While analysis to date indicates that the associated time constant should preclude any significant problems, testing is required to define more fully the possible magnus effects.

2. Preliminary wind-tunnel testing of the ring-fin design to substantiate theoretical estimates and delineate nonlinear effects and boundaries.

3. Real-time simulation of transient behavior during critical phases of flight.

Additional investigation of trade-offs which consider payload antenna pattern characteristics and possible location or orientation changes also has been noted as an area of recommended study.

Specific payload deployment dynamics and the dynamics associated with obtaining rapid parachute deployment, especially as higher altitudes are encountered, represent additional subjects for specialized studies.

REFERENCES

1. Weaver, W.L., A.G. Swanson, and J.F. Spurling. Statistical Wind Distribution Data for Use at NASA Wallops Station. NASA TN D-1249 (July 1962).

2. Rotolante, R.A., R.S. Briggs, and J.F. Bettle. Establishment of a Meteorological Rocket Station at McMurdo, Antarctica (Oct. 1963).

3. Itogawa, H., et al. Survey of Japanese Space Program With Emphasis on Kappa and Lambda Type Observation Rockets. NASA TT F-303 (Feb. 1965).

4. Cronshagen, A.H., and D.E. Hartrigsen. Why Mean Time to Failure Is Not Used to Assess the Reliability of Solid Rockets. Aerojet-General Corp. Report CRA 62-5 (12 June 1962).

5. Hoerner, S.F. Fluid Dynamic Drag (1965 Edition).

6. Morris, O. Aerodynamic Characteristics in Pitch of Several Ring-Wing-Body Configurations at a Mach Number of 2.2. NASA TN D-1272 (April 1962).

7. Experimental Investigation of Simple Symmetric and Un-symmetric Supersonic Ring Wings. Grumman Report RE 175 (May 1964).

8. Nelson, R.L. The Motions of Rolling Symmetrical Missiles Referred to a Body Axis System. NACA TN 3737 (Nov. 1956).

9. Whitlock, C.H. Comparison of Steady-State and Six-Degree-of-Freedom Analyses of Pitch-Roll Resonance Conditions for a Long Slender Sounding Rocket. NASA TN D-1816 (June 1963).

10. Falanga, R.A. Supersonic Investigation of a Spinning and Non-Spinning Model of a Cajun (or Apache) Rocket Vehicle With Roll Control Tabs. NASA TN D-2576 (Jan. 1965).

11. Platou, A.S. "Magnus Characteristics of Finned and Non-Finned Projectiles," AIAA Journal (Jan. 1965).